

Supporting Information for

The lifetime of carbon capture and storage as a climate-change mitigation technology

Michael L. Szulczewski, Christopher W. MacMinn,
Howard J. Herzog, and Ruben Juanes*

Massachusetts Institute of Technology,
77 Massachusetts Ave, Building 48–319, Cambridge MA 02139, USA

*To whom correspondence should be addressed; E-mail: juanes@mit.edu.

Here we present our calculation for the growth rate in CO₂ production, describe our mathematical models for CO₂ trapping and pressure build-up, and explain our methodology for applying the models to calculate storage capacity. We also describe the hydrogeologic setting of the aquifers we study and their storage capacities.

Contents

1	Growth rate of CO₂ production	3
2	CO₂ trapping model	3
2.1	Mathematical model	3
2.1.1	Injection period	5
2.1.2	Post-injection period	5

2.2	Migration-limited capacity	8
3	Pressure model	11
3.1	Mathematical model	11
3.2	Pressure-limited capacity	16
4	Methodology for application of the models	17
5	Aquifer data	23
5.1	Mt. Simon Sandstone	23
5.2	Black Warrior River Aquifer	28
5.3	Frio Formation	35
5.4	Madison Limestone	40
5.5	Navajo-Nugget Aquifer	44
5.6	Morrison Formation	48
5.7	Lower Potomac Aquifer	51
5.8	Fox Hills Sandstone	54
5.9	Paluxy Sandstone	57
5.10	St. Peter Sandstone	60
5.11	Cedar Keys and Lawson Dolomites	64
6	Sensitivity analysis	67
7	Uncertainty analysis	70
7.1	Uncertainty in input parameters	70
7.2	Uncertainty in capacity	70
8	Synopsis of aquifer data and storage capacities	80

1 Growth rate of CO₂ production

We calculate the growth rate of CO₂ production in the United States based on historical data of electricity production from 1972 to 2008 [1]. From this data, we calculate the coal and gas resources consumed each year by assuming an efficiency of 33% for coal and 44% for gas [2, Tables A2, A8]. We then calculate the CO₂ produced each year by assuming 90 Mt CO₂ per exajoule of coal consumed and 50 Mt CO₂ per exajoule of natural gas consumed [2, Tables A2, A18]. The growth rate of CO₂ production is then the slope of the linear regression of this data: 45 Mt CO₂ per year per year.

2 CO₂ trapping model

2.1 Mathematical model

The volume of CO₂, V_g , that can be trapped in a deep saline aquifer is usually calculated as a fraction of the total available pore volume [3, 4]:

$$V_g = V\phi(1 - S_{wc})\varepsilon, \quad (\text{S1})$$

where V is the aquifer volume, ϕ is the porosity, S_{wc} is the connate water saturation, and ε is the efficiency factor. We calculate the efficiency factor using a model for how CO₂ migrates through an aquifer and becomes trapped through solubility and capillary trapping [5, 6]. All parameters in the model are defined in Table S1. The major assumptions in the model are: (1) the interface between the CO₂ and brine is sharp [7–10]; (2) capillary pressure effects are negligible; (3) the flow is predominantly horizontal (Dupuit approximation) [7, 11]; (4) CO₂ leakage through the caprock is negligible; (5) the aquifer is homogeneous, isotropic, and incompressible; (6) the fluids are incompressible and their properties are constant; and (7) during the dissolution of CO₂ into brine, the total fluid volume is conserved.

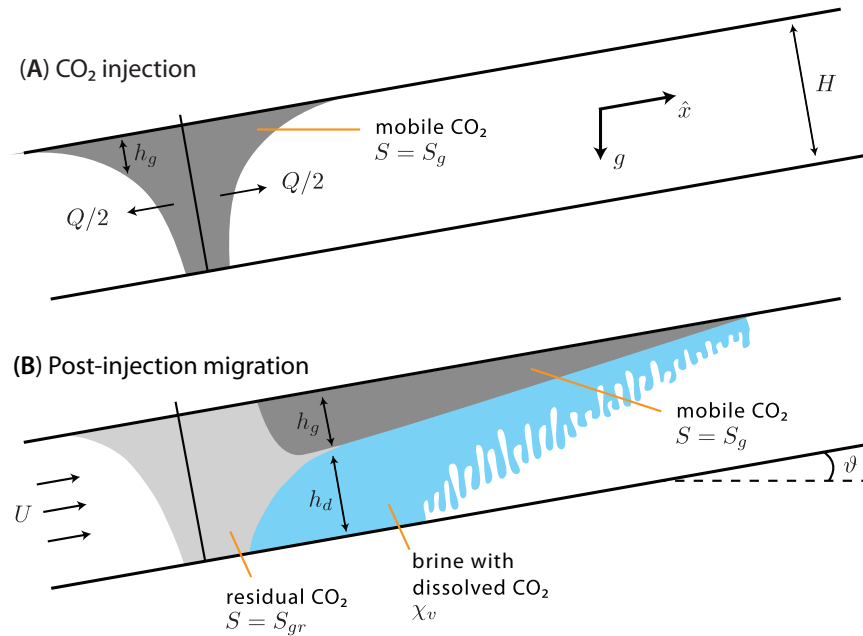


Figure S1: (A) During the injection period, CO₂ enters the aquifer at a high flow rate Q , displacing brine to its connate saturation S_{wc} . Since CO₂ is buoyant and less viscous than the brine, the injected CO₂ forms a gravity tongue [9]. No residual trapping occurs since there is little if any imbibition, and solubility trapping is negligible because the injection period is in general much shorter than the time required for dissolution [6]. (B) Once injection stops, the CO₂ plume migrates away from the well array due to buoyancy and the natural hydraulic gradient. Gravity tonguing becomes more severe, with the plume forming a thin wedge along the bottom of the caprock. At the trailing edge of the plume, CO₂ becomes trapped due to capillarity [12]. Along the bottom of the plume, CO₂ dissolves into the brine via convective mixing [13].

2.1.1 Injection period

We divide the model into two parts: the injection period and the post-injection period (Fig. S1). During injection, the thickness of the mobile CO₂ plume, h_g , as a function of time, t , and distance along the aquifer, x , is [5, 6, 9, 14]:

$$(1 - S_{wc})\phi\partial_t h_g + \partial_x F_g^i = 0, \quad (\text{S2})$$

where F_g^i is the flux of CO₂ during injection. Note that the model is one dimensional since we consider injection from a long, line-drive array of wells, as shown in Figure 2. Since the flux of CO₂ due to injection is typically much larger than fluxes due to buoyancy or the natural hydraulic gradient, the flux term is given by

$$F_g^i = \frac{Q}{2W}f, \quad (\text{S3})$$

where Q/W is the injection rate per unit width of the injection-well array. The fractional flow function f is given by

$$f = \frac{h_g}{h_g + \mathcal{M}(H - h_g)}, \quad (\text{S4})$$

where H is the thickness of the aquifer and \mathcal{M} is the mobility ratio,

$$\mathcal{M} = \frac{\mu_g}{k_{rg}^* \mu_w}. \quad (\text{S5})$$

2.1.2 Post-injection period

Once injection stops, the CO₂ plume migrates away from the well array. During migration, it becomes trapped by capillarity at the back of the plume, and by dissolution along the bottom of the plume until the underlying brine is saturated (Fig. S1). To determine when the brine is saturated, we model the transport of dissolved CO₂ in the brine in addition to the migration of the free-phase CO₂ plume.

Plume model. The thickness of the plume, h_g , during post-injection is also governed by a one-dimensional hyperbolic equation:

$$(1 - S_{wc})\phi\tilde{R}\partial_t h_g + \partial_x (F_g^p) = \mathcal{L}, \quad (\text{S6})$$

where F_g^p is the CO₂ flux during post-injection. \tilde{R} is a conditional coefficient that accounts for residual trapping:

$$\tilde{R} = \begin{cases} 1 & \text{if } \partial_t h_g > -q_d/\phi, \\ 1 - \Gamma & \text{otherwise,} \end{cases} \quad (\text{S7})$$

where Γ is the capillary trapping coefficient, which quantifies the fraction of pore space that will be occupied by residual CO₂:

$$\Gamma = \frac{S_{gr}}{1 - S_{wc}}. \quad (\text{S8})$$

q_d is the volumetric flux of CO₂ leaving the plume due to dissolution:

$$q_d = \frac{\alpha\chi_v\phi(\rho_d - \rho_w)gk_{aq}}{\mu_w}, \quad (\text{S9})$$

where α is a constant roughly equal to 0.01 [15], $\Delta\rho_d$ is the density difference between brine and CO₂-saturated brine, and χ_v is the solubility of CO₂ in brine, expressed as the volume of free-phase CO₂ that can be dissolved per unit volume of brine saturated with CO₂.

During post-injection, the flux is given by:

$$F_g^p = UHf + \frac{(\rho_w - \rho_g)gk_{aq}k_{gr}^* \sin \vartheta}{\mu_w}(1 - f)h_g, \quad (\text{S10})$$

where U is the Darcy velocity of the natural groundwater flow and ϑ is the slope of the caprock. The first term expresses the flux of CO₂ due to the natural hydraulic gradient and the second term expresses the flux due to upslope migration.

The right-hand side of the post-injection model (Eq. S6) is a loss term ($\mathcal{L} < 0$) that accounts for dissolution:

$$\mathcal{L} = \begin{cases} -\tilde{R}(1 - S_{wc})q_d & \text{if } h_d < H - h_g, \\ 0 & \text{otherwise,} \end{cases}$$

where h_d is the effective height of the water column under the plume that is saturated with CO_2 . Substituting each of these expressions into Eq. S6 yields the complete CO_2 trapping model:

$$(1 - S_{wc})\tilde{R}\partial_t h_g + \partial_x \left(UHf + \frac{(\rho_w - \rho_g)gk_{aq}k_{gr}^* \sin \vartheta}{\mu_w} (1 - f)h_g \right) = \mathcal{L}. \quad (\text{S11})$$

CO_2 -saturated-brine model. The model for the migration of CO_2 -saturated brine tracks the thickness of the region of brine below the plume that is saturated with CO_2 , h_d :

$$\chi_v \phi \partial_t h_d + \chi_v \partial_x F_d^p = -\mathcal{L} - \chi_v S_{wc} \phi \partial_t h_g, \quad (\text{S12})$$

where F_d^p is the flux of CO_2 -saturated brine. The thickness of the CO_2 -saturated region grows as a result of dissolution via the $-\mathcal{L}$ term (recall that $\mathcal{L} < 0$), which previously appeared as a loss term in the CO_2 model.

The flux of CO_2 -saturated brine F_d^p may occur due to a natural hydraulic gradient or the slope of the aquifer:

$$F_d^p = UH(1 - f) - \frac{(\rho_g - \rho_w)gk_{aq}k_{gr}^* \sin \vartheta}{\mu_g} (1 - f)h_g. \quad (\text{S13})$$

We neglect fluxes that may be caused by the density difference between the brine and CO_2 -saturated brine. We also neglect diffusion and dispersion.

Non-dimensional form of the equations. We choose the following non-dimensional variables:

$$\eta_g = h_g/H, \quad \eta_d = h_d/H, \quad \tau = t/T_c, \quad \xi = x/L_c, \quad (\text{S14})$$

where $L_c = QT_i/2W(1 - S_{wc})\phi H$, with $T_c = T_i$ being the injection time. With these variables, the injection model (Eq. S2) becomes:

$$\partial_\tau \eta_g + \frac{1}{2} \partial_\xi f = 0. \quad (\text{S15})$$

The model for the CO₂ migration during post-injection (Eq.S11) becomes:

$$\tilde{R}' \partial_\tau \eta_g + N_f \partial_\xi f + N_s \partial_\xi [(1-f)\eta_g] = -\tilde{R}' N_d, \quad (\text{S16})$$

and the model for the CO₂-saturated brine (Eq. S12) becomes:

$$\tilde{R}' \partial_\tau \eta_d + (1 - S_{wc}) N_f \partial_\xi f_d - (1 - S_{wc}) N_s \partial_\xi (f_d \eta_g) = \tilde{R}' \frac{N_d}{\Gamma_d} - S_{wc} \partial_\tau \eta_g, \quad (\text{S17})$$

where:

$$\tilde{R}' = \begin{cases} 1 & \text{if } \partial_\tau \eta_g > -N_d, \\ 1 - \Gamma & \text{otherwise.} \end{cases}$$

and

$$f(\eta_g) = \frac{\mathcal{M} \eta_g}{\mathcal{M} \eta_g + (1 - \eta_g)}, \quad f_d(\eta_g, \eta_d) = \frac{\eta_d}{\mathcal{M} \eta_g + (1 - \eta_g)}.$$

The coefficients in the equations are the flow number, N_f , and the slope number, N_s :

$$N_f = \frac{T_c}{T_i} \frac{2UH}{Q} \quad \text{and} \quad N_s = \frac{T_c}{L_c} \frac{(\rho_w - \rho_g) g k_{aq} k_{gr}^*}{(1 - S_{wc}) \phi \mu_g}, \quad (\text{S18})$$

which express the strength of the natural groundwater flow and the aquifer slope in driving plume migration. The dissolution number, N_d , expresses the strength of dissolution:

$$N_d = \begin{cases} \alpha \chi_v \frac{\Delta \rho_d g k_{aq} k_{gr}^* T_c}{H \phi \mu_g} & \text{if } \eta(\xi, \tau) > 0 \text{ and } \eta_d(\xi, \tau) < (1 - \eta(\xi, \tau)), \\ 0 & \text{otherwise.} \end{cases} \quad (\text{S19})$$

2.2 Migration-limited capacity

In an aquifer, a given volume of injected CO₂ will migrate a particular distance before becoming completely trapped by capillarity and solubility [5, 6, 10, 14]. There is a particular injection volume for which the CO₂ plume will just reach the boundary of the aquifer. We define this volume to be the migration-limited storage capacity. Rearranging the expression for non-dimensional distance ξ (Eq. S14), we obtain a formula for the injected volume $V_i = QT_i$:

$$V_i = xWH\phi(1 - S_{wc}) \frac{2}{\xi}.$$

By setting x to the total length of an aquifer, L_T , ξ to the dimensionless extent of the plume when it is fully trapped, ξ_T , we ensure that this injected volume will just fit in the aquifer. Since the model is one dimensional, we measure the length of an aquifer, L_T , in the direction parallel to migration. We calculate the dimensionless extent of the trapped plume, ξ_T , using the trapping model. To convert volume to mass of CO_2 , we multiply by the density of CO_2 in the aquifer, and obtain the final expression for the storage capacity, \mathcal{C}_t :

$$\mathcal{C}_t = \rho_g L_T W H \phi (1 - S_{wc}) \frac{2}{\xi_T}. \quad (\text{S20})$$

The expression has the same form as equations commonly used in the literature (Eq. S1), but the efficiency factor $\varepsilon = 2/\xi_T$ can now be calculated explicitly.

To calculate the efficiency factor, we first solve the equation for the injection plume (Eq. S15) analytically using the method of characteristics [5, 9]. We use the solution as the initial condition for the equations governing post-injection migration (Eq. S16–S17). While these equations can be solved semi-analytically in some limiting cases, we in general solve them numerically using a finite volume method with linear reconstructions and a van Leer limiter, and forward-Euler time stepping [16].

Table S1: The input parameters used in our models and their symbols. Dimension abbreviations are as follows: L = length, T = time, M = mass, and θ = temperature. Parameters written in Roman are raw input parameters; parameters written in italics are derived parameters.

Parameter [dimensions]	Symbol
Gravitational acceleration [LT^{-2}]	g
Residual CO_2 saturation [-]	S_{gr}
Connate water saturation [-]	S_{wc}
Endpoint relative permeability to CO_2 [-]	k_{gr}^*
Coefficient of CO_2 -saturated-brine flux [-]	α
Compressibility [$M^{-1}LT^2$]	c
Undrained Poisson ratio [-]	ν
Geothermal gradient [ΘL^{-1}]	G_T
Surface temperature [Θ]	T_s
Depth to top of aquifer [L]	D
Depth from aquifer to bedrock [L]	B
Net aquifer thickness [L]	H
Length of domain for migration model [L]	L_t
Width of well array [L]	W
Distance from well array to nearest pressure boundary [L]	L_{Pmin}
Distance from well array to farthest pressure boundary [L]	L_{Pmax}
Porosity [-]	ϕ
Caprock slope [-]	ϑ
Darcy velocity [LT^{-1}]	U
Aquifer permeability [L^2]	k_{aq}
Caprock permeability [L^2]	k_c
Salinity [ML^{-3}]	s
Average bulk density of the overburden [ML^{-3}]	$\overline{\rho_o}$
Average density of water in overburden [ML^{-3}]	$\overline{\rho_w}$
<i>Lateral overburden permeability</i> [L^2]	$\overline{k_x}$
<i>Vertical overburden permeability</i> [L^2]	$\overline{k_z}$
CO_2 solubility [-]	χ_v
<i>Brine density</i> [ML^{-3}]	ρ_w
<i>CO_2 density</i> [ML^{-3}]	ρ_g
<i>CO_2-saturated-brine density</i> [ML^{-3}]	ρ_d
<i>Brine viscosity</i> [$ML^{-1}T^{-1}$]	μ_w
<i>CO_2 viscosity</i> [$ML^{-1}T^{-1}$]	μ_g
<i>Fracture pressure</i> [$ML^{-1}T^{-2}$]	P_{frac}

3 Pressure model

3.1 Mathematical model

We have previously derived a one-dimensional version of our pressure model [17]. Here, we extend the model to two dimensions. All variables in the model are defined in Table S1. The major assumptions in the model are: (1) the vertical stress is lithostatic; (2) the overburden is the only source of horizontal stress (the bilateral constraint [18, p.282]); (3) the aquifer, the overburden, and the underburden are homogeneous; (4) the initial pressure is hydrostatic; (5) the aquifer properties and fluid properties are constant; (6) the pressure distribution along the line-drive array of wells is uniform; and (7) the compressibility of the CO₂ is negligible. This final assumption will cause the model to overestimate the pressure rise at the well array, and will therefore lead to conservative estimates of storage capacity.

The assumptions cause errors in the calculated pressure. Neglecting the compressibility of CO₂ will cause the model to overestimate the pressure rise at the well array, and will therefore lead to conservative estimates of storage capacity. Assuming uniform pressure along the well array can lead to an underestimation of the pressure buildup at the wells themselves, and could cause us to overestimate the storage capacity. The validity of this assumption can be estimated by comparing the timescale of pressure communication between wells in the array with the injection time: if the pressure field equilibrates along the well array quickly relative to the injection time, the assumption will be good and the error will be small. With this in mind, we estimate the pressure equilibration time and compare it to an injection time of 100 years, which is the most important time horizon in our study. We assume a permeability of $k=100$ mD, a brine viscosity of $\mu=1$ mPa s, and an aquifer compressibility of $c=0.1$ GPa⁻¹, based on aquifer data in Table S28. We find that for a well spacing of $l=10$ km, the timescale of pressure equilibration is roughly $l^2/(k/c\mu)\approx 3$ years, which is much smaller than the 100 year time

horizon. Since the well spacing is reasonable and the equilibration occurs relatively quickly, the assumption of uniform pressure along the array likely causes minimal error.

The geologic setting of our system is the same as the setting of the trapping model, but now includes the entire thickness of the basin that contains the target aquifer, as shown in Figure S3. In this system, the model for pressure, p , as a function of spatial coordinates x and z and time, t , is:

$$c\partial_t p + \partial_x u_x + \partial_z u_z = I(z), \quad (\text{S21})$$

where c is the compressibility, I is a function that represents injection into the aquifer, and u_x and u_z are the Darcy velocities in the x and z directions, respectively. Since we neglect the compressibility of CO_2 , these velocities are given by Darcy's law for single-phase flow:

$$u_x = -\frac{k_x(z)}{\mu_w} \partial_x p, \quad u_z = -\frac{k_z(z)}{\mu_w} (\partial_z p - \rho_w g), \quad (\text{S22})$$

where k_x and k_z are given by:

$$k_x(z) = \begin{cases} k_{aq} & D \leq z < D + H, \\ \overline{k_x} = k_{aq}/2 & \text{otherwise,} \end{cases}$$

$$k_z(z) = \begin{cases} k_{aq} & D \leq z < D + H, \\ \overline{k_z} = 2k_{cap} & \text{otherwise.} \end{cases}$$

These expressions are conditional because we assign different properties to the aquifer and the regions outside of the aquifer. Within the aquifer, the intrinsic permeability is k_{aq} . Above and below the aquifer, we set the permeability to average values ($\overline{k_x}$ and $\overline{k_z}$) derived from the aquifer permeability and the caprock permeability, k_{cap} , as shown in Figure S4. The source term I is conditional since it accounts for a ramping-up of the injection rate, a ramping-down of the

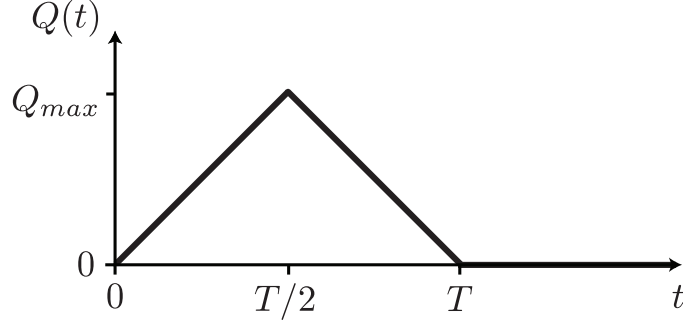


Figure S2: In our model, the injection rate of CO₂ increases linearly to a maximum, Q_{max} , decreases linearly to zero, and then remains at zero.

injection rate, and then no injection, as shown in Figure S2:

$$I(z, t) = \begin{cases} \delta(x)\mathcal{U}(z; D, D + H) \frac{2Q_{max}}{WH} \frac{t}{T} & 0 \leq t < T/2, \\ \delta(x)\mathcal{U}(z; D, D + H) \frac{2Q_{max}}{WH} \left(1 - \frac{t}{T}\right) & T/2 \leq t < T, \\ 0 & T \leq t, \end{cases}$$

where T_i is the injection time (Figure from main paper) and \mathcal{U} is the rectangular function, which allows injection only within the aquifer:

$$\mathcal{U}(z) = \begin{cases} 1 & D \leq z < D + H, \\ 0 & \text{otherwise.} \end{cases}$$

With these expressions, the model for pressure becomes:

$$c\partial_t p - \frac{k_x(z)}{\mu_w} \partial_{xx} p - \partial_z \left(\frac{k_z(z)}{\mu_w} (\partial_z p - \rho_w g) \right) = I(z, t) \quad (\text{S23})$$

$$X_{min} < x < X_{max}, \quad 0 < z < D + H + B, \quad t > 0,$$

where X_{min} is the distance to the nearest lateral boundary and X_{max} is the distance to the farthest lateral boundary. In practice, these boundaries correspond to the edges of the pressure-model domain (see Section 4).

The initial condition is hydrostatic pressure. The boundary condition at the top of the basin is a constant-pressure condition, and the boundary condition at the bottom of the basin is a

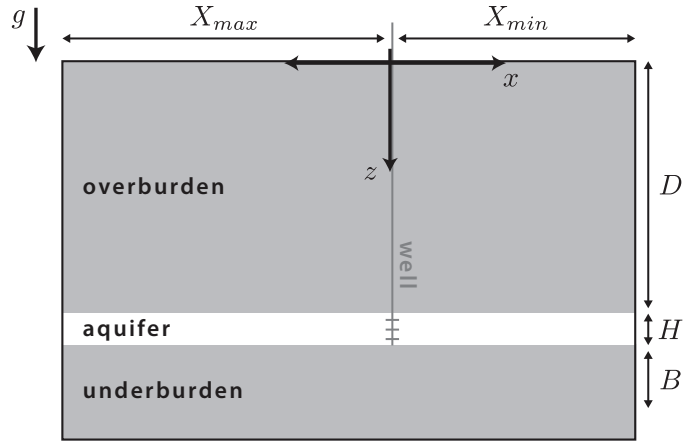


Figure S3: Since we consider injection from a line-drive array of wells, our pressure model is two dimensional: it captures behavior in a plane perpendicular to the line-drive array that extends from the ground surface to the basement. We position the center of the coordinate system where the line-drive array intersects the surface.

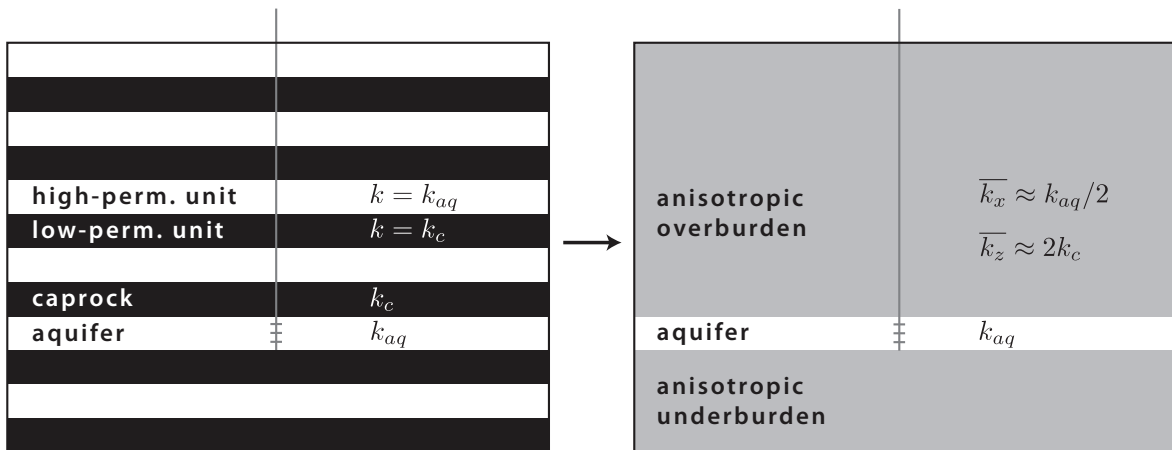


Figure S4: We model the entire thickness of a basin by assuming that it consists of multiple layers of high-permeability and low-permeability rock. We assume that each layer of high-permeability rock has the same permeability as the aquifer, and that each layer of low-permeability rock has the same permeability as the caprock. Under these assumptions, we average the permeabilities of all the layers above and below the aquifer to get homogeneous, but anisotropic permeabilities of the overburden and underburden.

no-flow condition. The boundary conditions at the sides of the basin may be either no-flow conditions or constant-pressure conditions depending on the geology. We assume that the same boundary condition applies over an entire side of the basin.

Non-dimensional form of the equations. We choose the following non-dimensional variables:

$$\tilde{p} = \frac{p - (p_o + \bar{\rho}_w g z)}{\bar{P}}, \quad \tau = \frac{t}{T_i}, \quad \xi = \frac{x}{L}, \quad \zeta = \frac{z}{H}. \quad (\text{S24})$$

We define the characteristic pressure and the characteristic length in the x -direction as:

$$\bar{P} = \frac{2Q_{max}}{HW} \sqrt{\frac{\mu_w T_i}{k_{aq} c}}, \quad L = \sqrt{\frac{k_{aq} T_i}{\mu_w c}}.$$

The non-dimensional form of the pressure model is:

$$\partial_\tau \tilde{p} - \lambda_\xi(\zeta) \partial_{\xi\xi} \tilde{p} - \partial_\zeta (\lambda(\zeta) \partial_\zeta \tilde{p}) = \tilde{I}(\zeta), \quad (\text{S25})$$

$$\Xi_{min} < \xi < \Xi_{max}, \quad 0 < \zeta < 1 + \Omega + \beta, \quad \tau > 0,$$

where the dimensionless lengths in the basin are given by:

$$\Xi_{min} = \frac{X_{min}}{L}, \quad \Xi_{max} = \frac{X_{max}}{L}, \quad \Omega = \frac{D}{H}, \quad \beta = \frac{B}{H}.$$

λ_ξ and λ_ζ are dimensionless diffusion coefficients given by:

$$\lambda_\xi(\zeta) = \begin{cases} 1 & \Omega \leq \zeta < \Omega + 1, \\ 1/2 & \text{otherwise,} \end{cases}$$

and

$$\lambda_\zeta(\zeta) = \begin{cases} \frac{k_{aq} T_i}{\mu_w c H^2} & \Omega \leq \zeta < \Omega + 1, \\ \frac{2k_{cap} T_i}{\mu_w c H^2} & \text{otherwise.} \end{cases}$$

The dimensionless injection function is:

$$\tilde{I}(\zeta, \tau) = \begin{cases} \delta(\xi) \mathcal{U}(\zeta; \Omega, \Omega + 1) \tau & 0 \leq \tau < 1/2, \\ \delta(\xi) \mathcal{U}(\zeta; \Omega, \Omega + 1) (1 - \tau) & 1/2 \leq \tau < 1, \\ 0 & 1 \leq \tau. \end{cases}$$

3.2 Pressure-limited capacity

For a given injection period T , a particular injection scenario characterized by Q_{max} will lead to a particular maximum pressure in the aquifer. There is a value of Q_{max} for which the maximum pressure will reach the fracture pressure of the aquifer. We define the volume injected in this scenario to be the pressure-limited storage capacity. In our ramp-up, ramp-down injection scenario, the volume injected is

$$V_p = \frac{1}{2}Q_{max}T. \quad (\text{S26})$$

The maximum injection rate can be obtained by rearranging the expression for the non-dimensional pressure, \tilde{p} (Eq. S24):

$$Q_{max} = HW \sqrt{\frac{k_{aq}c}{\mu_w T} \frac{p - (p_o + \bar{\rho}_w g z)}{2\tilde{p}}}.$$

Setting the pressure to the fracture pressure, $p = P_{frac}$, and the dimensionless pressure to the maximum dimensionless pressure, $\tilde{p} = \tilde{p}_{max}$, yields the maximum injection rate for which the pressure will just reach the fracture pressure. Substituting into the expression for injection volume and multiplying by the density of CO₂ yields the storage capacity in mass of CO₂, \mathcal{C}_p :

$$\mathcal{C}_p = \rho_g HW \sqrt{\frac{k_{aq}cT}{\mu_w} \frac{P_{frac} - (p_o + \bar{\rho}_w g D)}{4\tilde{p}_{max}}}. \quad (\text{S27})$$

We determine the maximum dimensionless pressure \tilde{p}_{max} by solving the pressure model (Eq. S25) numerically. We use a second-order finite-volume method in space with a Crank-Nicolson time discretization [16].

We define the fracture pressure, P_{frac} , to be the pressure required to create a tensile fracture in an aquifer [18, 19]. Ignoring the cohesive strength of the aquifer rock, a tensile fracture occurs when the pore pressure equals the least principal stress. When this stress is vertical, we calculate it to be the weight of the overburden:

$$P_{frac} = \bar{\rho}_o g D + p_o, \quad (\text{S28})$$

where $\bar{\rho}_o$ is the average bulk density of the overburden, which we approximate to be 2300 kg/m³ [20]. When it is horizontal, we approximate it using the bilateral constraint [18, p.282]. This constraint provides a relationship between the effective horizontal stress, σ'_h , and the effective vertical stress, σ'_v :

$$\sigma'_h = \frac{\nu}{1 - \nu} \sigma'_v,$$

$$\sigma_h - P_p = \frac{\nu}{1 - \nu} (\sigma_v - P_p),$$

where σ_h is the principle horizontal stress, σ_v is the vertical principle stress, ν is the Poisson ratio, and P_p is the pore pressure. Assuming that the pore pressure in a basin is hydrostatic, we solve this equation for the initial horizontal stress in an aquifer at depth D . We use this as an estimate of the pressure required to create a vertical fracture in rock with negligible cohesive strength:

$$P_{frac} = \frac{\nu}{1 - \nu} (\bar{\rho}_o g D - \bar{\rho}_w g D) + p_o + \bar{\rho}_w g D, \quad (\text{S29})$$

We determine whether the least principal stress is horizontal or vertical by using a stress map for the United States [21].

4 Methodology for application of the models

We calculate the storage capacity of eleven deep saline aquifers in the conterminous United States. We select these aquifers on the basis of their (1) size, (2) depth, and (3) structural integrity, and (4) on the availability of data . We select the largest aquifers because our model applies at large lateral length scales and because large aquifers will contribute the most strongly to the nationwide storage capacity. We select aquifers located at depths greater than 800 m to ensure that CO₂ will be stored efficiently as a high-density supercritical fluid. We study aquifers with as few major faults as possible to help reduce the possibility of leakage. While there are likely many deep saline aquifers that meet these criteria, we further restrict our study to those

aquifers that have been well characterized and for which the data is publicly available.

Aquifer boundaries. For each aquifer, we use the four criteria stated above—sufficient size, depth, structural integrity, and data—to determine which parts of it are suitable for sequestration. In general, these criteria may be evaluated at a range of length scales. For example, faults and pinchouts in the caprock may occur at scales ranging from the sub-meter scale or less to the regional scale. Since we calculate storage capacity at the basin scale, we evaluate these criteria at the basin scale and assume that small-scale variations will have small impacts on the storage capacity. When one of these criteria is not met at the basin scale, we exclude the appropriate region from our analysis by setting a boundary (Fig. S5).

Some types of boundaries impose boundary conditions in the pressure model (Fig. S5). We set constant pressure boundaries at outcrops. We set no-flow boundaries where the reservoir pinches out between two confining layers, changes to low-permeability rock ($k \leq 10$ millidarcy (mD), $1 \text{ darcy} = 10^{-12} \text{ m}^2$), or becomes cut by basin-scale faults. While faults may be either conductive or sealing, we set them to be no-flow boundaries so that the calculation of pressure-limited capacity is conservative.

Model domains. Within the boundaries of an aquifer, we determine the area over which to apply the trapping model. This region defines the maximum allowable extent of the plume when fully trapped, L_T , and the width of the well array, W . We select model domains in which the aquifer properties exhibit sufficient uniformity for the trapping model to capture basin-scale behavior of the injected CO_2 . In addition, we orient the model domains according to the dominant transport direction. If the transport directions are not co-linear, we compare N_s and N_f to determine the dominant process (Eq. S18). We evaluate N_s and N_f using values of their parameters averaged over the entire area within the reservoir boundaries. However, if the depth and isopotential contours are very complicated within some part of that area such that transport









Criterion for suitable aquifers	Feature marked	Boundary condition in pressure model	Symbol
Sufficient data	Limit of available data	no flow	
Aquifer continuity	Reservoir pinchouts	no flow	
	Low-perm. regions	no flow	
Low potential of leakage	Faults	no flow	
	Outcrops	constant pressure	
	Caprock pinchouts	<i>not a pressure boundary</i>	
	High-perm. region in caprock	<i>not a pressure boundary</i>	
Sufficient depth	800m - depth contour	<i>not a pressure boundary</i>	

Figure S5: We exclude portions of an aquifer from our analysis if they do not meet the four criteria in this table. In our geologic maps, we delineate these regions by drawing boundaries. Some of these boundaries impose boundary conditions in the pressure model.

from ground water flow or up-slope migration can not be approximated as one-dimensional, we exclude that area from our averaging.

Another constraint on the size of a model domain comes from an assumption in the trapping model: since the model assumes that all behavior perpendicular to the well-array has a negligible or higher-order effect on migration, it rigorously applies to domains in which the ratio of the length parallel to the intended well array to the length parallel to transport is large. While we usually choose domains with an aspect ratio of two or larger, in some cases we use domains that have an aspect ratio closer to one. In these cases, the trapping model predicts a migration distance that is longer than the real migration distance of a given volume of CO₂, since the spread of the real plume parallel to the well array would be important.

In addition to setting the trapping model domain, we set the area over which to apply the pressure model. Since we use the same well array in the pressure model as we do in the trapping model, the widths of these two domains are the same. However, their lengths are often different because not all of the aquifer boundaries correspond to boundary conditions in the pressure model (Fig. S5). This is because regions are not suitable for storing CO₂ may be suitable for “storing” some of the pressure perturbation due to injection. The distances from the well array to the edges of the pressure model domain define the distances to the lateral boundaries in the pressure model, X_{min} and X_{max} (Eq. S23).

As with the trapping model domains, the pressure-model domains should have large aspect ratios for the pressure model to be strictly valid. However, this is difficult to accomplish in practice, and many of the pressure model domains in this study have aspect ratios near one or less. In these cases, pressure diffusion in the direction parallel to the well array becomes important, resulting in a smaller overpressure at the well array for a given injection scenario compared to the model predictions. Since the model overestimates the pressure rise in these cases, it underestimates the pressure-limited capacity (Eq. S27).

Model parameters. Within a model domain, we set the parameters in the models in three ways (Table S1): by using aquifer data directly, by using aquifer data to calculate the parameters, or by estimation. We list the method we use and the value of each parameter in the section describing each aquifer (*e.g.* Table S2).

We use aquifer data directly to set parameters such as the aquifer depth, thickness, porosity, salinity, and permeability. Since the data often exhibit large uncertainty and variability at the basin scale, we choose representative values. We choose these values to make the storage capacity calculations conservative. For example, if an aquifer exhibits a wide range of porosities, we choose a low value in the range, which will result in a lower trapping-limited storage capacity.

When aquifer data cannot be used directly, we use it to calculate the required parameters. We calculate CO₂ viscosity and density as functions of temperature and pressure [22]. We calculate the temperature in an aquifer, T_{aq} , using the surface temperature, T_s , and the geothermal gradient, G . We calculate the fluid pressure assuming a hydrostatic gradient. Brine density, brine viscosity, and the solubility of CO₂ in brine are functions of salinity in addition to temperature and pressure. While aquifer brines may contain a wide variety of salts, we treat them as consisting of only water and sodium chloride (NaCl), which is by far the dominant salt in nearly every deep saline aquifer [23]. We calculate the density and viscosity of brine using correlations based on temperature, pressure, and concentration of sodium chloride [24]. We determine the solubility of CO₂ in brine from published experimental data for salinities up four molal [25] and from a correlation for higher salinities [26].

In the trapping model, the relevant measure of CO₂ solubility is the volume of free-phase CO₂ that can be dissolved per unit volume of brine saturated with CO₂. This parameter, χ_v (Eq. S9), can be calculated from the solubility in terms of mass fraction, χ_m :

$$\chi_v = \frac{\rho_d}{\rho_g} \chi_m.$$

To calculate the density of CO₂-saturated brine, ρ_d , we use the following formula [27, 28]:

$$\rho_d = \frac{\rho_w}{1 - \chi_m(1 - V_\phi \rho_w^*/M_g)},$$

where M_g is the molar mass of CO₂, ρ_w^* is the density of pure water at aquifer conditions, and V_ϕ is the apparent molar volume of CO₂ in the brine, given by the following correlation [28]:

$$V_\phi = 37.51 \times 10^{-6} - (9.585 \times 10^{-8})T_{aq} + (8.740 \times 10^{-10})T_{aq}^2 - (5.044 \times 10^{-13})T_{aq}^3,$$

where T_{aq} is in degrees Celsius and V_ϕ is in m³/mol.

When there is insufficient data to determine the required parameters, we estimate them. Since little or no data was available for the compressibility of the aquifers and caprocks in this study, we set the average compressibility for every basin to $c = 10^{-10} \text{ Pa}^{-1}$, as has been done in other basin-scale studies [29]. We do not pursue a more rigorous approach because published compressibility data for many types of aquifers and caprocks are equal to within the variability and uncertainty of the data, and also similar to the compressibility of water at the pressure and temperature conditions of deep aquifers. For example, published values for sandstones and limestones generally range from 1×10^{-11} to $1 \times 10^{-10} \text{ Pa}^{-1}$ [30, 31], while published values for low-porosity shales and mudstones ($\phi < 0.2$) generally range from 1×10^{-11} to $1 \times 10^{-9} \text{ Pa}^{-1}$ [32–35]. Similarly, we set the Poisson ratio of the aquifers or caprocks to 0.3 in every basin, which is a value characteristic of many sedimentary rocks [30].

When data on caprock permeability is unavailable, we estimate it to be 0.01 mD [36–38]. While rocks deeper than about 3 km can exhibit much lower permeability [39], we use this value for all confining units under the assumption that small fractures that are likely widespread at the basin scale will produce effective permeabilities of this order or higher.

Since aquifer-specific data on the multiphase-flow characteristics of CO₂ and brine was also unavailable, we estimate the connate water saturation, residual CO₂ saturation, and the

endpoint relative permeability to CO_2 . Based on published data, we take $S_{wc} = 0.4$, $S_{gr} = 0.3$, and $k_{gr}^* = 0.6$ [40]. These values correspond to $\Gamma = 0.5$.

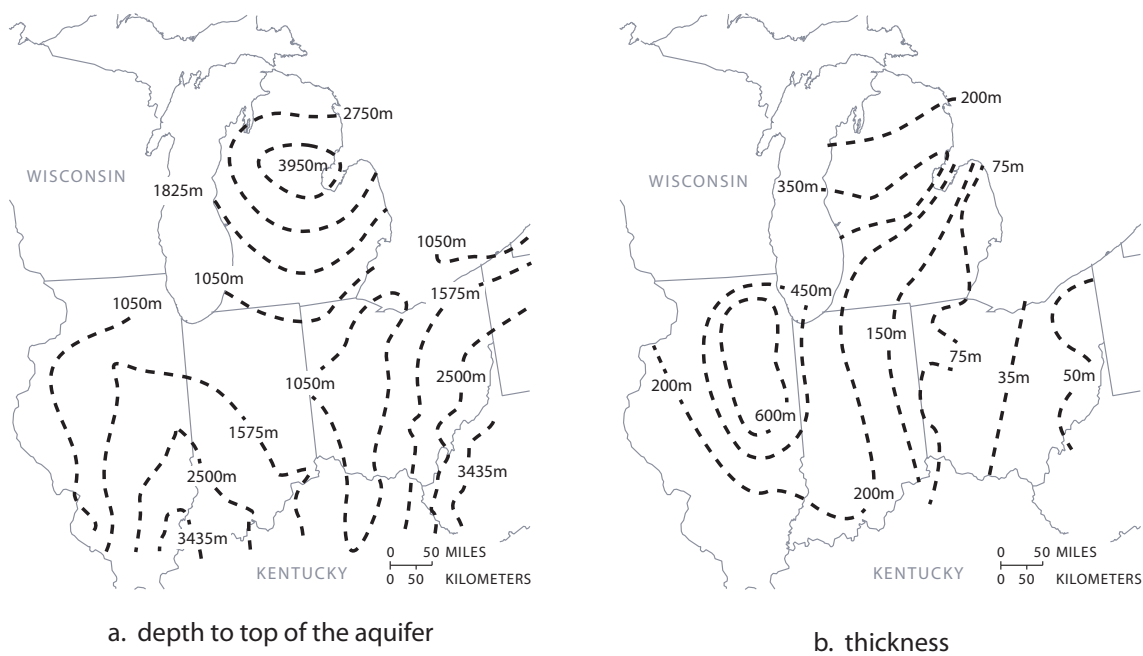
5 Aquifer data

5.1 Mt. Simon Sandstone

The Mt. Simon Sandstone is widespread in the Midwestern United States, as shown in Figure S6. It is a transgressive sandstone that consists dominantly of quartz arenite [41, 42]. Near its base, the formation tends to be conglomeratic with igneous pebbles [43, 44]. Lenses of sandy to silty shale are interbedded in the lower part of the formation in Illinois, and in the upper part of the formation throughout the Midwest [42, p.B13].

The Mt. Simon Sandstone is overlain by the Eau Claire Formation, which is composed of silty dolomites, dolomitic sandstones, and shale [41]. This formation has been identified as a regional confining unit by a number of authors [42, 45, 46]. The Mt. Simon unconformably overlies Precambrian igneous and metamorphic rocks, which we take as an aquiclude [43, 44].

In this study, we model sequestration in deep parts of the formation that lie in the Michigan Basin, Illinois Basin, and the Indiana-Ohio Platform. Within each region, we identify a single model domain, as shown in Figure S7. The data for each domain are shown in Tables S2, S3, and S4.



a. depth to top of the aquifer

b. thickness

Figure S6: The Mt. Simon Sandstone is widespread in the Midwest. It is deepest and thickest in the centers of the Illinois, Michigan, and Appalachian Basins. (a) Modified from [41, Fig.A2-3],[47, Map c1mtingsong], and [48, Fig.3]. (b) Modified from [41, Fig.A2-2],[49, Fig.2], and [48, Fig.4].

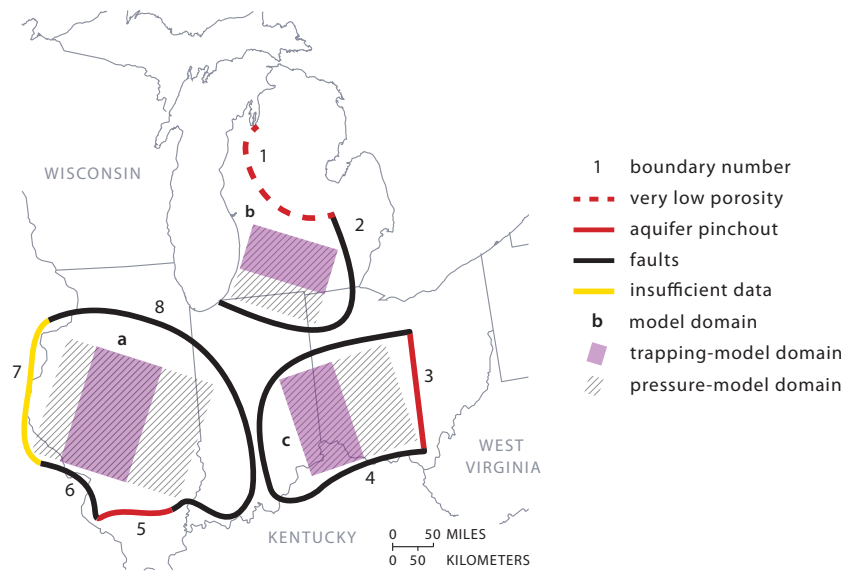


Figure S7: We divide the Mt. Simon Sandstone into regions **a**, **b**, and **c** using eight boundaries. Boundary 1 corresponds to where the porosity becomes very low due to diagenesis ($\phi < 0.1$) [48]. Boundary 3 corresponds to where the Mt. Simon Sandstone pinches out into thinner sandstones [49, Fig.2], and Boundary 5 corresponds to where it pinches out between the Precambrian basement and the caprock [49, Fig.2]. Boundary 7 corresponds to the edge of available depth and thickness maps [47, Map c1mSimonag]. Boundaries 2, 4, 6 and 8 correspond to basin-scale faults[41, 50]. Within each region, we set the extent and orientation of the model domains based on the aquifer’s topography since upslope migration is the dominant transport mechanism.

Table S2: Parameters for Region a of the Mt. Simon Sandstone.

Parameter	Symbol	Value	Data Source	Reference
Residual CO ₂ saturation	S_{rg}	0.3	estimated	[40, 51]
Connate water saturation	S_{wc}	0.4	estimated	[40, 51]
Endpoint relative permeability to CO ₂	k_{rg}^*	0.6	estimated	[40, 51]
Coefficient of CO ₂ -saturated-brine flux	α	0.01	estimated	[52, 53]
Compressibility (GPa ⁻¹)	c	0.1	estimated	[30, Table C1]
Undrained Poisson ratio	ν	0.3	estimated	[30, Table C1]
Geothermal gradient (°C/km)	G_T	20	aquifer data	[54, 55]
Surface temperature (°C)	T_s	10	aquifer data	[56]
Depth to top of aquifer (m)	D	2000	aquifer data	[47, Map c1mtsimong]
Depth from aquifer to bedrock (m)	B	0	aquifer data	[41]
Net aquifer thickness (m)	H	400	aquifer data	[49, Fig.2]
Length of model domain (km)	L_{aq}	100	aquifer data	Fig. S7
Length of pressure domain (km)	L_{pres}	300	aquifer data	Fig. S7
Width of well array (km)	W	200	aquifer data	Fig. S7
Porosity	ϕ	0.2	aquifer data	[49]
Caprock slope (degrees)	ϑ	0.5	calculated	[47, Map c1mtsimong]
Darcy velocity (cm/yr)	U	1	calculated	[57, Fig.43]
Aquifer permeability (mD)	k_{aq}	100	aquifer data	[41, p.57]
Mean vertical permeability (mD)	k_{cap}	0.01	estimated	[36–38]
Lateral overburden permeability (mD)	\bar{k}_x	50	calculated	Fig. S4
Vertical overburden permeability (mD)	\bar{k}_z	0.02	calculated	Fig. S4
Salinity (ppm)	s	100000	aquifer data	[58]
CO ₂ solubility (volume fraction)	χ_v	0.05	calculated	[25]
Brine density (kg/m ³)	ρ_w	1000	calculated	[24]
CO ₂ density (kg/m ³)	ρ_g	700	calculated	[22]
Brine density change from diss. (kg/m ³)	$\Delta\rho_d$	6	calculated	[28, 59]
Brine viscosity (mPa s)	μ_w	0.8	calculated	[24]
CO ₂ viscosity (mPa s)	μ_g	0.06	calculated	[22]
Fracture (MPa)	P_{frac}	40	calculated	Eq. S29,S28; [21]

Table S3: Parameters for Region b of the Mt. Simon Sandstone.

Parameter	Symbol	Value	Data Source	Reference
Residual CO ₂ saturation	S_{rg}	0.3	estimated	[40, 51]
Connate water saturation	S_{wc}	0.4	estimated	[40, 51]
Endpoint relative permeability to CO ₂	k_{rg}^*	0.6	estimated	[40, 51]
Coefficient of CO ₂ -saturated-brine flux	α	0.01	estimated	[52]
Compressibility (GPa ⁻¹)	c	0.1	estimated	[30–35]
Undrained Poisson ratio	ν	0.3	estimated	[30, Table C1]
Geothermal gradient (°C/km)	G_T	20	aquifer data	[54, 55]
Surface temperature (°C)	T_s	9	aquifer data	[56]
Depth to top of aquifer (m)	D	2000	aquifer data	[48, Fig.4]
Depth from aquifer to bedrock (m)	B	0	aquifer data	[41]
Net aquifer thickness (m)	H	200	aquifer data	[48, Fig.4]
Length of model domain (km)	L_t	200	aquifer data	Fig. S7
Length of pressure domain (km)	L_{pres}	200	aquifer data	Fig. S7
Width of well array (km)	W	200	aquifer data	Fig. S7
Porosity	ϕ	0.2	aquifer data	[48]
Caprock slope (degree)	ϑ	0.7	calculated	[48, Fig.4]
Darcy velocity (cm/yr)	U	1	calculated	[57, Fig.43]
Aquifer permeability (mD)	k_{aq}	100	aquifer data	[41, p.57]
Caprock permeability (mD)	k_c	0.01	estimated	[36–38]
Lateral overburden permeability (mD)	\bar{k}_x	50	calculated	Fig. S4
Vertical overburden permeability (mD)	\bar{k}_z	0.02	calculated	Fig. S4
Salinity (g/L)	s	200	aquifer data	[60, Fig.37]
CO ₂ solubility (volume fraction)	χ_v	0.04	calculated	[6, 25]
Brine density (kg/m ³)	ρ_w	1000	calculated	[24]
CO ₂ density (kg/m ³)	ρ_g	800	calculated	[22]
Brine density change from diss. (kg/m ³)	$\Delta\rho_d$	8	calculated	[28, 59]
Brine viscosity (mPa s)	μ_w	1	calculated	[24]
CO ₂ viscosity (mPa s)	μ_g	0.07	calculated	[22]
Fracture pressure (MPa)	P_{frac}	40	calculated	Eq. S29,S28; [21]

Table S4: Parameters for Region **c** of the Mt. Simon Sandstone.

Parameter	Symbol	Value	Data Source	Reference
Residual CO ₂ saturation	S_{rg}	0.3	estimated	[40, 51]
Connate water saturation	S_{wc}	0.4	estimated	[40, 51]
Endpoint relative permeability to CO ₂	k_{rg}^*	0.6	estimated	[40, 51]
Coefficient of CO ₂ -saturated-brine flux	α	0.01	estimated	[52]
Compressibility (GPa ⁻¹)	c	0.1	estimated	[30–35]
Undrained Poisson ratio	ν	0.3	estimated	[30, Table C1]
Geothermal gradient (°C/km)	G_T	20	aquifer data	[54, 55]
Surface temperature (°C)	T_s	10	aquifer data	[56]
Depth to top of aquifer (m)	D	1000	aquifer data	[47, Map c1simong]
Depth from aquifer to bedrock (m)	B	0	aquifer data	[41]
Net aquifer thickness (m)	H	100	aquifer data	[48, Fig.4]
Length of model domain (km)	L_t	300	aquifer data	Fig. S7
Length of pressure domain (km)	L_{pres}	200	aquifer data	Fig. S7
Width of well array (km)	W	200	aquifer data	Fig. S7
Porosity	ϕ	0.2	estimated	[19]
Caprock slope (degree)	ϑ	0.001	calculated	[47, Map c1simong]
Darcy velocity (cm/yr)	U	1	calculated	[57, Fig.43]
Aquifer permeability (mD)	k_{aq}	100	aquifer data	[41, p.57]
Caprock permeability (mD)	k_c	0.01	estimated	[36–38]
Lateral overburden permeability (mD)	\bar{k}_x	50	calculated	Fig. S4
Vertical overburden permeability (mD)	\bar{k}_z	0.02	calculated	Fig. S4
Salinity (g/L)	s	200	aquifer data	[60, Fig.37]
CO ₂ solubility (volume fraction)	χ_v	0.04	calculated	[6, 25]
Brine density (kg/m ³)	ρ_w	1000	calculated	[24]
CO ₂ density (kg/m ³)	ρ_g	700	calculated	[22]
Brine density change from diss. (kg/m ³)	$\Delta\rho_d$	7	calculated	[28, 59]
Brine viscosity (mPa s)	μ_w	1	calculated	[24]
CO ₂ viscosity (mPa s)	μ_g	0.06	calculated	[22]
Fracture pressure (MPa)	P_{frac}	20	calculated	Eq. S29,S28; [21]

5.2 Black Warrior River Aquifer

Following previous studies, we model a number of Cretaceous rocks in the southeastern Coastal Plain as a single aquifer called the Black Warrior River Aquifer [61–64]. This aquifer begins in central Alabama and Georgia, where it either outcrops or pinches out, and from there it deepens and thickens toward the Gulf of Mexico. In Alabama and northwestern Florida, it consists of rocks in the Eutaw and McShan Formations and the Tuscaloosa Group. In Georgia and northeastern Florida, it consists of rocks in the Eutaw Formation, Tuscaloosa Formation,

and the Atkinson Formation [61, Fig.72]. These rocks are mostly sandstone interbedded with siltstone, shale, and mudstone [61, 62, 64]. They were deposited in a variety of settings, including fluvial, deltaic, and marine environments.

A variety of rocks underlie the aquifer. These rocks include Precambrian crystalline rocks, Paleozoic and Mesozoic sedimentary rocks, and Lower Mesozoic redbeds and diabase [61, Fig.76]. While some of these rocks are porous and permeable, we do not model them because they are very poorly characterized. The aquifer is overlain by the Selma Group, which consists mostly of chalk and is recognized by many authors as a regional aquitard [61, 62, 64].

A variety of geologic features constrain the region of the Black Warrior River Aquifer that is suitable for sequestration, as shown in Figure S8. Within this region, we identify four model domains, also shown in Figure S8. The data for each domain are shown in Tables S5, S6, S7, and S8.

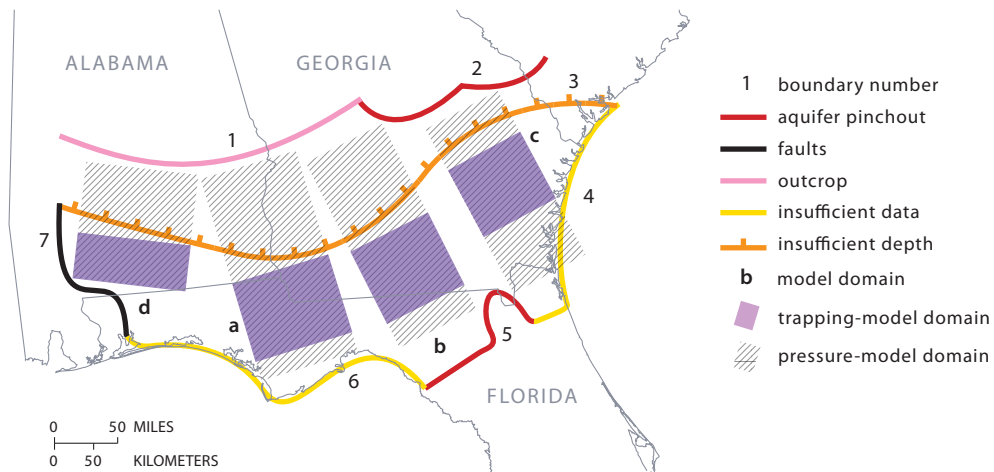


Figure S8: We identify seven boundaries that constrain the portion of the Black Warrior River Aquifer that is suitable for sequestration. Boundary 1 corresponds to where the aquifer crops out in central Alabama and Georgia [61, Fig.79]. Boundary 2 corresponds to where it pinches out between the overlying Chattahoochee River Aquifer and underlying low-permeability rocks [61]. Boundary 3 marks where the aquifer becomes shallower than 800m [61, Fig.79]. Boundaries 4 and 6 correspond to edge of available depth maps [61, 62, 65]. Boundary 5 shows where the aquifer pinches out or becomes very thin [65, Plate 3A]. Finally, Boundary 7 corresponds to where the aquifer becomes offset by a fault system by up to hundreds of meters. Within these boundaries, we identify four regions in which to apply our models (Regions a, b, c, and d).

Table S5: Parameters for Region a of the Black Warrior River Aquifer.

Parameter	Symbol	Value	Data Source	Reference
Residual CO ₂ saturation	S_{rg}	0.3	estimated	[40, 51]
Connate water saturation	S_{wc}	0.4	estimated	[40, 51]
Endpoint relative permeability to CO ₂	k_{rg}^*	0.6	estimated	[40, 51]
Coefficient of CO ₂ -saturated-brine flux	α	0.01	estimated	[52, 53]
Compressibility (GPa ⁻¹)	c	0.1	estimated	[30, Table C1]
Undrained Poisson ratio	ν	0.3	estimated	[30, Table C1]
Geothermal gradient (°C/km)	G_T	30	aquifer data	[54, 55]
Surface temperature (°C)	T_s	20	aquifer data	[56]
Depth to top of aquifer (m)	D	1000	aquifer data	[62, Plate41],[66]
Depth from aquifer to bedrock (m)	B	0	aquifer data	[61, Fig.76]
Net aquifer thickness (m)	H	1000	aquifer data	[62, Plate 42]
Length of model domain (km)	L_T	100	aquifer data	Fig. S8
Length of pressure domain (km)	L_{press}	300	aquifer data	Fig. S8
Width of well array (km)	W	100	aquifer data	Fig. S8
Porosity	ϕ	0.2	estimated	[19]
Caprock slope (degrees)	ϑ	0.5	calculated	[62, Plate41]
Darcy velocity (cm/yr)	U	1 ^a	calculated	[67, p.D68]
Aquifer permeability (mD)	k_{aq}	100 ^b	aquifer data	[68, Fig.30C][62, Plate 42]
Mean vertical permeability (mD)	k_{cap}	0.01	aquifer data	[69]
Lateral overburden permeability (mD)	\bar{k}_x	50	calculated	Fig. S4
Vertical overburden permeability (mD)	\bar{k}_z	0.02	calculated	Fig. S4
Salinity (g/L)	s	100	aquifer data	[70, Plate 2]
CO ₂ solubility (volume fraction)	χ_v	0.05	calculated	[25]
Brine density (kg/m ³)	ρ_w	1000	calculated	[24]
CO ₂ density (kg/m ³)	ρ_g	700	calculated	[22]
Brine density change from diss. (kg/m ³)	$\Delta\rho_d$	8	calculated	[28, 59]
Brine viscosity (mPa s)	μ_w	0.8	calculated	[24]
CO ₂ viscosity (mPa s)	μ_g	0.05	calculated	[22]
Fracture pressure (MPa)	P_{frac}	20	calculated	Eq. S29,S28; [21]

^a There are no data available to calculate the Darcy velocity in the deep Black Warrior River Aquifer. In the shallow aquifer, Darcy velocities of about 10 cm/yr have been estimated using simulations and isotopic data [67, p.D68]. However, the region suitable for sequestration is more than 100 km south of where the data were taken and more than 750 m deeper. Since velocity generally decreases with depth and distance from recharge sources, I arbitrarily lower the shallow aquifer velocity by a factor of 10. The resulting value is commensurate with velocities in other deep saline aquifers such as the Mt. Simon Sandstone.

^b Calculated from mapped values of transmissivity between 80 and 399 m²/day [68, Fig.30C] and aquifer thickness [62, Plate 42].

Table S6: Parameters for Region b of the Black Warrior River Aquifer.

Parameter	Symbol	Value	Data Source	Reference
Residual CO ₂ saturation	S_{rg}	0.3	estimated	[40, 51]
Connate water saturation	S_{wc}	0.4	estimated	[40, 51]
Endpoint relative permeability to CO ₂	k_{rg}^*	0.6	estimated	[40, 51]
Coefficient of CO ₂ -saturated-brine flux	α	0.01	estimated	[52, 53]
Compressibility (GPa ⁻¹)	c	0.1	estimated	[30, Table C1]
Undrained Poisson ratio	ν	0.3	estimated	[30, Table C1]
Geothermal gradient (°C/km)	G_T	20	aquifer data	[54, 55]
Surface temperature (°C)	T_s	20	aquifer data	[56]
Depth to top of aquifer (m)	D	100	aquifer data	[62, Plate41],[66]
Depth from aquifer to bedrock (m)	B	0	aquifer data	[61, Fig.76]
Net aquifer thickness (m)	H	300	aquifer data	[62, Plate 42]
Length of model domain (km)	L_T	100	aquifer data	Fig. S8
Length of pressure domain (km)	L_{pres}	300	aquifer data	Fig. S8
Width of well array (km)	W	100	aquifer data	Fig. S8
Porosity	ϕ	0.2	estimated	[19]
Caprock slope (degrees)	ϑ	0.2	calculated	[62, Plate41]
Darcy velocity (cm/yr)	U	1 ^a	calculated	[67, p.D68]
Aquifer permeability (mD)	k_{aq}	400 ^b	aquifer data	[68, Fig.30C][62, Plate 42]
Mean vertical permeability (mD)	k_{cap}	0.01	aquifer data	[69]
Lateral overburden permeability (mD)	\bar{k}_x	200	calculated	Fig. S4
Vertical overburden permeability (mD)	\bar{k}_z	0.02	calculated	Fig. S4
Salinity (g/L)	s	10	aquifer data	[70, Plate 2]
CO ₂ solubility (volume fraction)	χ_v	0.07	calculated	[25]
Brine density (kg/m ³)	ρ_w	1000	calculated	[24]
CO ₂ density (kg/m ³)	ρ_g	700	calculated	[22]
Brine density change from diss. (kg/m ³)	$\Delta\rho_d$	10	calculated	[28, 59]
Brine viscosity (mPa s)	μ_w	0.7	calculated	[24]
CO ₂ viscosity (mPa s)	μ_g	0.06	calculated	[22]
Fracture pressure (MPa)	P_{frac}	10	calculated	Eq. S29,S28; [21]

^a There are no data available to calculate the Darcy velocity in the deep Black Warrior River Aquifer. In the shallow aquifer, Darcy velocities of about 10 cm/yr have been estimated using simulations and isotopic data [67, p.D68]. However, the region suitable for sequestration is more than 100 km south of where the data were taken and more than 750 m deeper. Since velocity generally decreases with depth and distance from recharge sources, I arbitrarily lower the shallow aquifer velocity by a factor of 10. The resulting value is commensurate with velocities in other deep saline aquifers such as the Mt. Simon Sandstone.

^b Calculated from mapped values of transmissivity between 80 and 399 m²/day [68, Fig.30C] and aquifer thickness [62, Plate 42].

Table S7: Parameters for Region C of the Black Warrior River Aquifer.

Parameter	Symbol	Value	Data Source	Reference
Residual CO ₂ saturation	S_{rg}	0.3	estimated	[40, 51]
Connate water saturation	S_{wc}	0.4	estimated	[40, 51]
Endpoint relative permeability to CO ₂	k_{rg}^*	0.6	estimated	[40, 51]
Coefficient of CO ₂ -saturated-brine flux	α	0.01	estimated	[52, 53]
Compressibility (GPa ⁻¹)	c	0.1	estimated	[30, Table C1]
Undrained Poisson ratio	ν	0.3	estimated	[30, Table C1]
Geothermal gradient (°C/km)	G_T	20	aquifer data	[54, 55]
Surface temperature (°C)	T_s	20	aquifer data	[56]
Depth to top of aquifer (m)	D	1000	aquifer data	[62, Plate41],[66]
Depth from aquifer to bedrock (m)	B	0	aquifer data	[61, Fig.76]
Net aquifer thickness (m)	H	200	aquifer data	[62, Plate 42]
Length of model domain (km)	L_T	90	aquifer data	Fig. S8
Length of pressure domain (km)	L_{pres}	200	aquifer data	Fig. S8
Width of well array (km)	W	100	aquifer data	Fig. S8
Porosity	ϕ	0.2	estimated	[19]
Caprock slope (degrees)	ϑ	0.2	calculated	[62, Plate41]
Darcy velocity (cm/yr)	U	1 ^a	calculated	[67, p.D68]
Aquifer permeability (mD)	k_{aq}	900 ^b	aquifer data	[68, Fig.30C][62, Plate 42]
Mean vertical permeability (mD)	k_{cap}	0.01	aquifer data	[69]
Lateral overburden permeability (mD)	\bar{k}_x	500	calculated	Fig. S4
Vertical overburden permeability (mD)	\bar{k}_z	0.02	calculated	Fig. S4
Salinity (g/L)	s	10	aquifer data	[70, Plate 2]
CO ₂ solubility (volume fraction)	χ_v	0.07	calculated	[25]
Brine density (kg/m ³)	ρ_w	1000	calculated	[24]
CO ₂ density (kg/m ³)	ρ_g	700	calculated	[22]
Brine density change from diss. (kg/m ³)	$\Delta\rho_d$	10	calculated	[28, 59]
Brine viscosity (mPa s)	μ_w	0.7	calculated	[24]
CO ₂ viscosity (mPa s)	μ_g	0.06	calculated	[22]
Fracture pressure (MPa)	P_{frac}	20	calculated	Eq. S29,S28; [21]

^a There are no data available to calculate the Darcy velocity in the deep Black Warrior River Aquifer. In the shallow aquifer, Darcy velocities of about 10 cm/yr have been estimated using simulations and isotopic data [67, p.D68]. However, the region suitable for sequestration is more than 100 km south of where the data were taken and more than 750 m deeper. Since velocity generally decreases with depth and distance from recharge sources, I arbitrarily lower the shallow aquifer velocity by a factor of 10. The resulting value is commensurate with velocities in other deep saline aquifers such as the Mt. Simon Sandstone.

^b Calculated from mapped values of transmissivity between 80 and 399 m²/day [68, Fig.30C] and aquifer thickness [62, Plate 42].

Table S8: Parameters for Region d of the Black Warrior River Aquifer.

Parameter	Symbol	Value	Data Source	Reference
Residual CO ₂ saturation	S_{rg}	0.3	estimated	[40, 51]
Connate water saturation	S_{wc}	0.4	estimated	[40, 51]
Endpoint relative permeability to CO ₂	k_{rg}^*	0.6	estimated	[40, 51]
Coefficient of CO ₂ -saturated-brine flux	α	0.01	estimated	[52, 53]
Compressibility (GPa ⁻¹)	c	0.1	estimated	[30, Table C1]
Undrained Poisson ratio	ν	0.3	estimated	[30, Table C1]
Geothermal gradient (°C/km)	G_T	30	aquifer data	[54, 55]
Surface temperature (°C)	T_s	20	aquifer data	[56]
Depth to top of aquifer (m)	D	1000	aquifer data	[62, Plate41],[66]
Depth from aquifer to bedrock (m)	B	0	aquifer data	[61, Fig.76]
Net aquifer thickness (m)	H	2000	aquifer data	[62, Plate 42]
Length of model domain (km)	L_T	60	aquifer data	Fig. S8
Length of pressure domain (km)	L_{pres}	100	aquifer data	Fig. S8
Width of well array (km)	W	100	aquifer data	Fig. S8
Porosity	ϕ	0.2	estimated	[19]
Caprock slope (degrees)	ϑ	0.6	calculated	[62, Plate41]
Darcy velocity (cm/yr)	U	1 ^a	calculated	[67, p.D68]
Aquifer permeability (mD)	k_{aq}	60 ^b	aquifer data	[68, Fig.30C][62, Plate 42]
Mean vertical permeability (mD)	k_{cap}	0.01	aquifer data	[69]
Lateral overburden permeability (mD)	\bar{k}_x	30	calculated	Fig. S4
Vertical overburden permeability (mD)	\bar{k}_z	0.02	calculated	Fig. S4
Salinity (g/L)	s	80	aquifer data	[70, Plate 2]
CO ₂ solubility (volume fraction)	χ_v	0.06	calculated	[25]
Brine density (kg/m ³)	ρ_w	1000	calculated	[24]
CO ₂ density (kg/m ³)	ρ_g	700	calculated	[22]
Brine density change from diss. (kg/m ³)	$\Delta\rho_d$	9	calculated	[28, 59]
Brine viscosity (mPa s)	μ_w	0.7	calculated	[24]
CO ₂ viscosity (mPa s)	μ_g	0.05	calculated	[22]
Fracture pressure (MPa)	P_{frac}	20	calculated	Eq. S29,S28; [21]

^a There are no data available to calculate the Darcy velocity in the deep Black Warrior River Aquifer. In the shallow aquifer, Darcy velocities of about 10 cm/yr have been estimated using simulations and isotopic data [67, p.D68]. However, the region suitable for sequestration is more than 100 km south of where the data were taken and more than 750 m deeper. Since velocity generally decreases with depth and distance from recharge sources, I arbitrarily lower the shallow aquifer velocity by a factor of 10. The resulting value is commensurate with velocities in other deep saline aquifers such as the Mt. Simon Sandstone.

^b Calculated from mapped values of transmissivity between 80 and 399 m²/day [68, Fig.30C] and aquifer thickness [62, Plate 42].

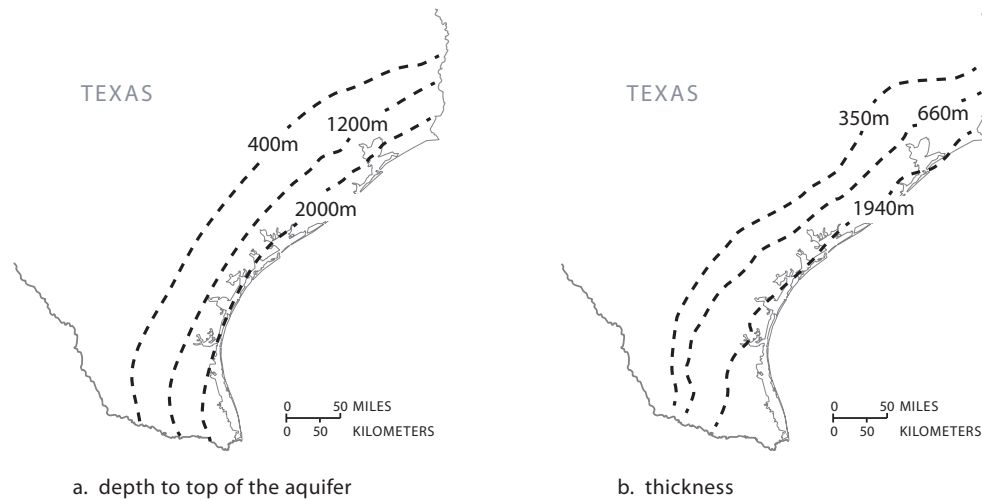


Figure S9: The Frio Formation is located on the east coast of Texas. It dips and thickens toward the coast. (a) Modified from [47, Map c1friog1]. (b) Modified from [47, Map c4friog].

5.3 Frio Formation

The Frio Formation occurs in the Gulf Basin in Texas. Starting at outcrops about 150km inland from the coast, it dips and thickens uniformly toward the coast as shown in Figure S9, reaching depths of more than 3000m below sea level [71, p.21].

The Frio Formation is highly heterogeneous, consisting of interfingering marine and non-marine sands and shales [72]. These sediments occur in a variety of facies such as deltaic and fluvial facies [73]. The Frio Formation is overlain by the Anuhac Formation and underlain by the Vicksburg Group and Jackson Group. These units are composed dominantly of clay and form an effective aquitard and aquiclude [74].

We model sequestration in a broad region of the Frio Formation along the Texas coast, as shown in Figure S10. Within this region, we identify three regions in which to apply our models (Regions a, b, and c). The data for each region are shown in Tables S9, S10, and S11.

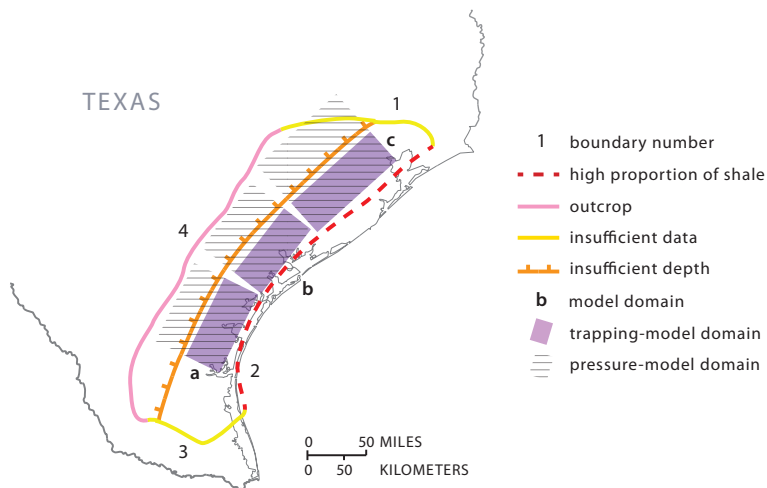


Figure S10: We identify four boundaries that constrain the portion of the Frio Formation that is suitable for sequestration. Boundaries 1 and 3 correspond to the edges of available depth and thickness maps [47]. Boundary 2 corresponds to where the proportion of shale in the formation becomes greater than 80% [47, Map 5frio]. Boundary 4 corresponds to outcrops [47]. Within these boundaries, we identify three regions in which to apply our models (Regions a, b, and c).

Table S9: Parameters for Region a of the Frio Formation.

Parameter	Symbol	Value	Data Source	Reference
Residual CO ₂ saturation	S_{rg}	0.3	estimated	[40, 51]
Connate water saturation	S_{wc}	0.4	estimated	[40, 51]
Endpoint relative permeability to CO ₂	k_{rg}^*	0.6	estimated	[40, 51]
Coefficient of CO ₂ -saturated-brine flux	α	0.01	estimated	[52, 53]
Compressibility (GPa ⁻¹)	c	0.1	estimated	[30, Table C1]
Undrained Poisson ratio	ν	0.3	estimated	[30, Table C1]
Geothermal gradient (°C/km)	G_T	30	aquifer data	[54, 55]
Surface temperature (°C)	T_s	20	aquifer data	[56]
Depth to top of aquifer (m)	D	1000	aquifer data	[47, Map c1friog1]
Depth from aquifer to bedrock (m)	B	10000	aquifer data	[75]
Net aquifer thickness (m)	H	2000	aquifer data	[47, Map c3friog]
Length of model domain (km)	L_T	50	aquifer data	Fig. S10
Length of pressure domain (km)	L_{pres}	100	aquifer data	Fig. S10
Width of well array (km)	W	100	aquifer data	Fig. S10
Porosity	ϕ	0.2	aquifer data	[76, Fig.10]
Caprock slope (degrees)	ϑ	2	calculated	[72, Fig.2]
Darcy velocity (cm/yr)	U	10 ^a	calculated	[77]
Aquifer permeability (mD)	k_{aq}	400	aquifer data	[76, Fig.8]
Mean vertical permeability (mD)	k_{cap}	0.01	estimated	[36–38]
Lateral overburden permeability (mD)	\bar{k}_x	200	calculated	Fig. S4
Vertical overburden permeability (mD)	\bar{k}_z	0.02	calculated	Fig. S4
Salinity (g/L)	s	50	aquifer data	[78, Fig.2A]
CO ₂ solubility (volume fraction)	χ_v	0.07	calculated	[25]
Brine density (kg/m ³)	ρ_w	1000	calculated	[24]
CO ₂ density (kg/m ³)	ρ_g	500	calculated	[22]
Brine density change from diss. (kg/m ³)	$\Delta\rho_d$	8	calculated	[28, 59]
Brine viscosity (mPa s)	μ_w	0.8	calculated	[24]
CO ₂ viscosity (mPa s)	μ_g	0.04	calculated	[22]
Fracture pressure (MPa)	P_{frac}	20	calculated	Eq. S29,S28; [21]

^a We set the Darcy velocity to 10 cm/yr based on reported ranges for the velocity [77] and values in other deep saline aquifers.

Table S10: Parameters for Region b of the Frio Formation.

Parameter	Symbol	Value	Data Source	Reference
Residual CO ₂ saturation	S_{rg}	0.3	estimated	[40, 51]
Connate water saturation	S_{wc}	0.4	estimated	[40, 51]
Endpoint relative permeability to CO ₂	k_{rg}^*	0.6	estimated	[40, 51]
Coefficient of CO ₂ -saturated-brine flux	α	0.01	estimated	[52, 53]
Compressibility (GPa ⁻¹)	c	0.1	estimated	[30, Table C1]
Undrained Poisson ratio	ν	0.3	estimated	[30, Table C1]
Geothermal gradient (°C/km)	G_T	30	aquifer data	[54, 55]
Surface temperature (°C)	T_s	20	aquifer data	[56]
Depth to top of aquifer (m)	D	1000	aquifer data	[47, Map c1frieg1]
Depth from aquifer to bedrock (m)	B	10000	aquifer data	[75]
Net aquifer thickness (m)	H	900	aquifer data	[47, Map c3frieg]
Length of model domain (km)	L_T	40	aquifer data	Fig. S10
Length of pressure domain (km)	L_{pres}	100	aquifer data	Fig. S10
Width of well array (km)	W	100	aquifer data	Fig. S10
Porosity	ϕ	0.2	aquifer data	[76, Fig.10]
Caprock slope (degrees)	ϑ	2	calculated	[72, Fig.2]
Darcy velocity (cm/yr)	U	10 ^a	calculated	[77]
Aquifer permeability (mD)	k_{aq}	400	aquifer data	[76, Fig.8]
Mean vertical permeability (mD)	k_{cap}	0.01	estimated	[36–38]
Lateral overburden permeability (mD)	\bar{k}_x	200	calculated	Fig. S4
Vertical overburden permeability (mD)	\bar{k}_z	0.02	calculated	Fig. S4
Salinity (g/L)	s	50	aquifer data	[78, Fig.2A]
CO ₂ solubility (volume fraction)	χ_v	0.08	calculated	[25]
Brine density (kg/m ³)	ρ_w	1000	calculated	[24]
CO ₂ density (kg/m ³)	ρ_g	500	calculated	[22]
Brine density change from diss. (kg/m ³)	$\Delta\rho_d$	8	calculated	[28, 59]
Brine viscosity (mPa s)	μ_w	0.6	calculated	[24]
CO ₂ viscosity (mPa s)	μ_g	0.04	calculated	[22]
Fracture pressure (MPa)	P_{frac}	20	calculated	Eq. S29,S28; [21]

^a We set the Darcy velocity to 10 cm/yr based on reported ranges for the velocity [77] and values in other deep saline aquifers.

Table S11: Parameters for Region c of the Frio Formation.

Parameter	Symbol	Value	Data Source	Reference
Residual CO ₂ saturation	S_{rg}	0.3	estimated	[40, 51]
Connate water saturation	S_{wc}	0.4	estimated	[40, 51]
Endpoint relative permeability to CO ₂	k_{rg}^*	0.6	estimated	[40, 51]
Coefficient of CO ₂ -saturated-brine flux	α	0.01	estimated	[52, 53]
Compressibility (GPa ⁻¹)	c	0.1	estimated	[30, Table C1]
Undrained Poisson ratio	ν	0.3	estimated	[30, Table C1]
Geothermal gradient (°C/km)	G_T	30	aquifer data	[54, 55]
Surface temperature (°C)	T_s	20	aquifer data	[56]
Depth to top of aquifer (m)	D	1000	aquifer data	[47, Map c1frieg1]
Depth from aquifer to bedrock (m)	B	10000	aquifer data	[75]
Net aquifer thickness (m)	H	700	aquifer data	[47, Map c3frieg]
Length of model domain (km)	L_T	50	aquifer data	Fig. S10
Length of pressure domain (km)	L_{pres}	100	aquifer data	Fig. S10
Width of well array (km)	W	100	aquifer data	Fig. S10
Porosity	ϕ	0.2	aquifer data	[76, Fig.10]
Caprock slope (degrees)	ϑ	6	calculated	[72, Fig.2]
Darcy velocity (cm/yr)	U	10 ^a	calculated	[77]
Aquifer permeability (mD)	k_{aq}	400	aquifer data	[76, Fig.8]
Mean vertical permeability (mD)	k_{cap}	0.01	estimated	[36–38]
Lateral overburden permeability (mD)	\bar{k}_x	200	calculated	Fig. S4
Vertical overburden permeability (mD)	\bar{k}_z	0.02	calculated	Fig. S4
Salinity (g/L)	s	100	aquifer data	[78, Fig.2A]
CO ₂ solubility (volume fraction)	χ_v	0.08	calculated	[25]
Brine density (kg/m ³)	ρ_w	1000	calculated	[24]
CO ₂ density (kg/m ³)	ρ_g	500	calculated	[22]
Brine density change from diss. (kg/m ³)	$\Delta\rho_d$	8	calculated	[28, 59]
Brine viscosity (mPa s)	μ_w	0.6	calculated	[24]
CO ₂ viscosity (mPa s)	μ_g	0.04	calculated	[22]
Fracture pressure (MPa)	P_{frac}	20	calculated	Eq. S29,S28; [21]

^a We set the Darcy velocity to 10 cm/yr based on reported ranges for the velocity [77] and values in other deep saline aquifers.

5.4 Madison Limestone

The Madison Limestone occurs in the Williston Basin [79]. In general, it dips and thickens towards the center of the basin in western North Dakota, as shown Figure S11.

The Madison Limestone consists of a sequence of carbonates and evaporates that are divided into three formations [80]. From oldest to youngest, these are the Lodgepole Limestone, the Mission Canyon Limestone, and the Charles Formation. The Lodgepole Limestone consists mainly of argillaceous, thin-bedded limestone and dolomite. The Mission Canyon Limestone consists mainly of limestone that is coarsely crystalline at its base and finer at its top. The Charles Formation consists of anhydrite and halite with interbedded dolomite and limestone.

In the Williston Basin, the Madison Limestone is overlain by the Big Snowy Group [80]. This group consists mostly of shale and sandstone, with minor limestone. We model it together with the Charles Formation as an aquitard. The aquifer is underlain by the Bakken Formation in the Williston Basin, which consists of more than 30 meters of shale and siltstone [80]. We model this formation as an aquiclude.

We model sequestration in two regions of the Madison Limestone, as shown in Figure S12. Within each region, we identify one model domain. The data for each domain are shown in Tables S12 and S13.

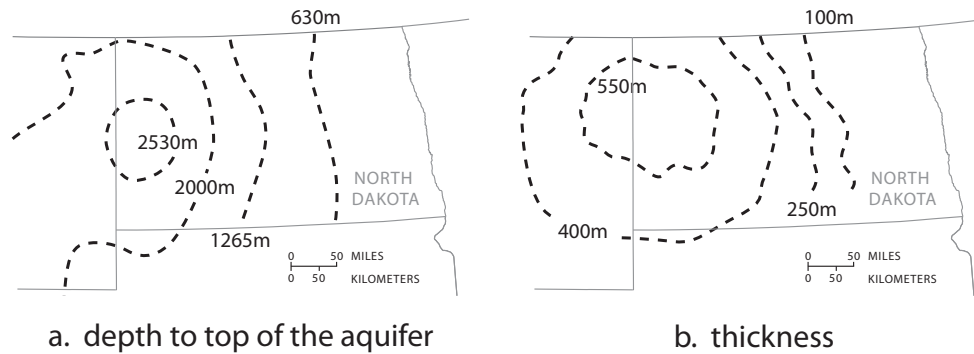


Figure S11: The Madison Limestone is located in Williston Basin in North Dakota, South Dakota, and Montana. The basin is roughly bowl-shaped, with the center and deepest part of the bowl located in western North Dakota. (a) Modified from [47, Map c1madisong]. (b) Modified from [80, Fig.11].

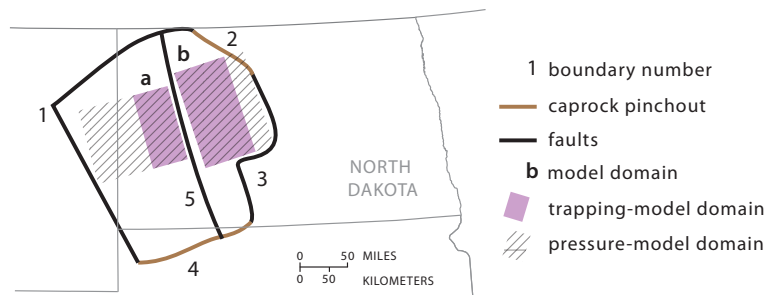


Figure S12: We identify five boundaries that constrain the portion of the Frio Formation that is suitable for sequestration. Boundaries 1, 3, and 5 correspond to basin-scale faults and lineaments [80, Fig.16]. Boundaries 2 and 4 correspond to where the caprock pinches out [80, Fig.12]. Within these boundaries, we identify two regions in which to apply our models (Regions a and b).

Table S12: Parameters for Region a of the Madison Limestone.

Parameter	Symbol	Value	Data Source	Reference
Residual CO ₂ saturation	S_{rg}	0.3	estimated	[40, 51]
Connate water saturation	S_{wc}	0.4	estimated	[40, 51]
Endpoint relative permeability to CO ₂	k_{rg}^*	0.6	estimated	[40, 51]
Coefficient of CO ₂ -saturated-brine flux	α	0.01	estimated	[52, 53]
Compressibility (GPa ⁻¹)	c	0.1	estimated	[30, Table C1]
Undrained Poisson ratio	ν	0.3	estimated	[30, Table C1]
Geothermal gradient (°C/km)	G_T	40	aquifer data	[54, 55]
Surface temperature (°C)	T_s	6	aquifer data	[56]
Depth to top of aquifer (m)	D	3000	aquifer data	[17]
Depth from aquifer to bedrock (m)	B	2000	aquifer data	[75]
Net aquifer thickness (m)	H	600	aquifer data	[17]
Length of model domain (km)	L_T	60	aquifer data	Fig. S12
Length of pressure domain (km)	L_{pres}	200	aquifer data	Fig. S12
Width of well array (km)	W	100	aquifer data	Fig. S12
Porosity	ϕ	0.08	estimated	[17]
Caprock slope (degrees)	ϑ	0.4	calculated	[17]
Darcy velocity (cm/yr)	U	8	calculated	[17]
Aquifer permeability (mD)	k_{aq}	60	aquifer data	[17]
Mean vertical permeability (mD)	k_{cap}	0.01	estimated	[36–38]
Lateral overburden permeability (mD)	\bar{k}_x	30	calculated	Fig. S4
Vertical overburden permeability (mD)	\bar{k}_z	0.02	calculated	Fig. S4
Salinity (g/L)	s	200	aquifer data	[79, Fig.61]
CO ₂ solubility (volume fraction)	χ_v	0.05	calculated	[25]
Brine density (kg/m ³)	ρ_w	1000	calculated	[24]
CO ₂ density (kg/m ³)	ρ_g	500	calculated	[22]
Brine density change from diss. (kg/m ³)	$\Delta\rho_d$	5	calculated	[28, 59]
Brine viscosity (mPa s)	μ_w	0.4	calculated	[24]
CO ₂ viscosity (mPa s)	μ_g	0.04	calculated	[22]
Fracture pressure (MPa)	P_{frac}	30	calculated	Eq. S29,S28; [21]

Table S13: Parameters for Region **b** of the Madison Limestone.

Parameter	Symbol	Value	Data Source	Reference
Residual CO ₂ saturation	S_{rg}	0.3	estimated	[40, 51]
Connate water saturation	S_{wc}	0.4	estimated	[40, 51]
Endpoint relative permeability to CO ₂	k_{rg}^*	0.6	estimated	[40, 51]
Coefficient of CO ₂ -saturated-brine flux	α	0.01	estimated	[52, 53]
Compressibility (GPa ⁻¹)	c	0.1	estimated	[30, Table C1]
Undrained Poisson ratio	ν	0.3	estimated	[30, Table C1]
Geothermal gradient (°C/km)	G_T	40	aquifer data	[54, 55]
Surface temperature (°C)	T_s	6	aquifer data	[56]
Depth to top of aquifer (m)	D	2000	aquifer data	[17]
Depth from aquifer to bedrock (m)	B	1000	aquifer data	[75]
Net aquifer thickness (m)	H	500	aquifer data	[17]
Length of model domain (km)	L_T	90	aquifer data	Fig. S12
Length of pressure domain (km)	L_{pres}	100	aquifer data	Fig. S12
Width of well array (km)	W	200	aquifer data	Fig. S12
Porosity	ϕ	0.08	estimated	[17]
Caprock slope (degrees)	ϑ	0.5	calculated	[17]
Darcy velocity (cm/yr)	U	5	calculated	[17]
Aquifer permeability (mD)	k_{aq}	60	aquifer data	[17]
Mean vertical permeability (mD)	k_{cap}	0.01	estimated	[36–38]
Lateral overburden permeability (mD)	\bar{k}_x	30	calculated	Fig. S4
Vertical overburden permeability (mD)	\bar{k}_z	0.02	calculated	Fig. S4
Salinity (g/L)	s	300	aquifer data	[79, Fig.61]
CO ₂ solubility (volume fraction)	χ_v	0.03	calculated	[25]
Brine density (kg/m ³)	ρ_w	1000	calculated	[24]
CO ₂ density (kg/m ³)	ρ_g	500	calculated	[22]
Brine density change from diss. (kg/m ³)	$\Delta\rho_d$	11	calculated	[28, 59]
Brine viscosity (mPa s)	μ_w	0.6	calculated	[24]
CO ₂ viscosity (mPa s)	μ_g	0.04	calculated	[22]
Fracture pressure (MPa)	P_{frac}	30	calculated	Eq. S29,S28; [21]

5.5 Navajo-Nugget Aquifer

The Navajo-Nugget Aquifer is sufficiently deep for sequestration in the eastern Uinta Basin in northeastern Utah and the Green River Basin in southwest Wyoming [81, Figure 10]. In the eastern Uinta Basin, it consists of the Glen Canyon Sandstone. In the Green River Basin, it consists of the Nugget Sandstone [81, Plate 1]. These rocks were deposited primarily in an eolian environment, but contain minor fluvial components. They typically consist of massive, crossbedded sandstone that has well-sorted, very fine to medium grains [81, p.C17].

The Navajo-Nugget Aquifer is overlain by the Carmel-Twin Creek Confining Unit. This unit consists mostly of siltstone and shale with some interbedded gypsum. The aquifer is underlain by the Chinle-Moenkopi Confining Unit. This unit consists mostly of siltstone, claystone, and limestone [81, Table 1].

We model sequestration from one well array in both the Uinta Basin and the Green River Basin, as shown in Figure S13. The data for these regions are shown in Tables S14 and S15.

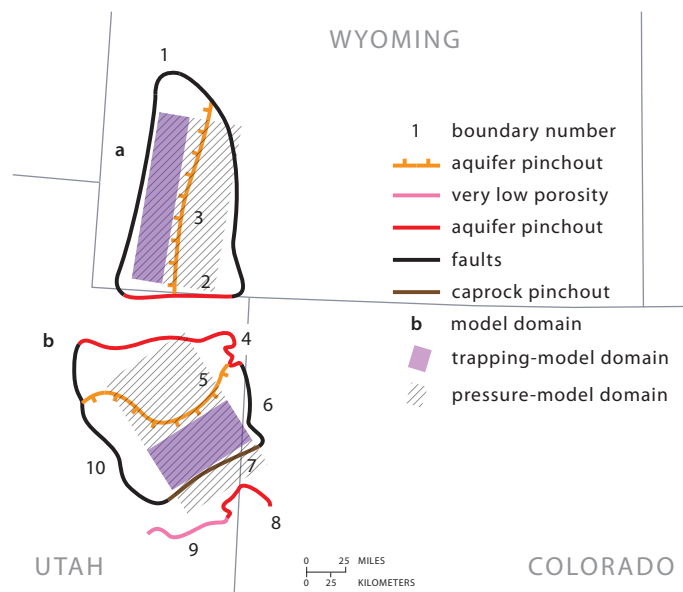


Figure S13: We identify ten boundaries that constrain the portion of the Navajo-Nugget Aquifer that is suitable for sequestration. Boundaries 1, 6, and 10 correspond to basin-scale faults in Mesozoic rocks [81, Fig.6]. Boundaries 2, 4, and 8 mark where the Navajo-Nugget Aquifer is absent [82, Fig.14]. Boundaries 3 and 5 correspond to where the aquifer becomes more than 4000 m deep, which we consider to be too deep for a cost-effective sequestration project [66, 82]. Boundary 7 corresponds to the farthest extent of the Carmel-Twin Creek Confining Unit [81, Plate 2B]. Lastly, Boundary 9 corresponds to where the Navajo-Nugget Aquifer crops out [82, Fig.14]

Table S14: Parameters for Region a of the Navajo-Nugget Aquifer.

Parameter	Symbol	Value	Data Source	Reference
Residual CO ₂ saturation	S_{rg}	0.3	estimated	[40, 51]
Connate water saturation	S_{wc}	0.4	estimated	[40, 51]
Endpoint relative permeability to CO ₂	k_{rg}^*	0.6	estimated	[40, 51]
Coefficient of CO ₂ -saturated-brine flux	α	0.01	estimated	[52, 53]
Compressibility (GPa ⁻¹)	c	0.1	estimated	[30, Table C1]
Undrained Poisson ratio	ν	0.3	estimated	[30, Table C1]
Geothermal gradient (°C/km)	G_T	30	aquifer data	[54, 55]
Surface temperature (°C)	T_s	6	aquifer data	[56]
Depth to top of aquifer (m)	D	3000	aquifer data	[66, 82]
Depth from aquifer to bedrock (m)	B	500	aquifer data	[75, 81, 82]
Net aquifer thickness (m)	H	200	aquifer data	[81, Plate 3A]
Length of trapping-model domain (km)	L_T	30	aquifer data	Fig. S13
Length of pressure-model domain (km)	L_{pres}	90	aquifer data	Fig. S13
Width of well array (km)	W	200	aquifer data	Fig. S13
Porosity	ϕ	0.2	estimated	[81, Fig.30]
Caprock slope (degrees)	ϑ	2	calculated	[82]
Darcy velocity (cm/yr)	U	10 ^a	calculated	[82, Fig.15]
Aquifer permeability (mD)	k_{aq}	100 ^b	calculated	[81, Figs.33,46]
Mean vertical permeability (mD)	k_{cap}	0.01	estimated	[36–38]
Lateral overburden permeability (mD)	\bar{k}_x	50	calculated	Fig. S4
Vertical overburden permeability (mD)	\bar{k}_z	0.02	calculated	Fig. S4
Salinity (g/L)	s	35	aquifer data	[82, Fig.19]
CO ₂ solubility (volume fraction)	χ_v	0.07	calculated	[6, 25]
Brine density (kg/m ³)	ρ_w	1000	calculated	[24]
CO ₂ density (kg/m ³)	ρ_g	600	calculated	[22]
Brine density change from diss. (kg/m ³)	$\Delta\rho_d$	9	calculated	[28, 59]
Brine viscosity (mPa s)	μ_w	0.4	calculated	[24]
CO ₂ viscosity (mPa s)	μ_g	0.05	calculated	[22]
Fracture pressure (MPa)	P_{frac}	70	calculated	Eq. S29,S28; [21]

^a In deep parts of the aquifer where we model sequestration, hydraulic head measurements are not available. As a result, we calculate the Darcy velocity based on head measurements in the shallower parts of the reservoir. While the actual velocity in the model domain is likely lower, the exact value of the Darcy velocity does not affect the capacity estimation since migration is driven dominantly by slope ($N_s/N_f \gg 1$).

^b Hydraulic conductivity data for the Navajo-Nugget Aquifer generally comes from outcrops or shallow wells, where it ranges from at least 0.03 to 3 m/day [81, Figs.33,46]. This corresponds to permeabilities in the range of about 40 to 4000 mD. Since regions suitable for sequestration are deeply buried, we set the permeability to a low value in this range.

Table S15: Parameters for Region b of the Navajo-Nugget Aquifer.

Parameter	Symbol	Value	Data Source	Reference
Residual CO ₂ saturation	S_{rg}	0.3	estimated	[40, 51]
Connate water saturation	S_{wc}	0.4	estimated	[40, 51]
Endpoint relative permeability to CO ₂	k_{rg}^*	0.6	estimated	[40, 51]
Coefficient of CO ₂ -saturated-brine flux	α	0.01	estimated	[52, 53]
Compressibility (GPa ⁻¹)	c	0.1	estimated	[30, Table C1]
Undrained Poisson ratio	ν	0.3	estimated	[30, Table C1]
Geothermal gradient (°C/km)	G_T	30	aquifer data	[54, 55]
Surface temperature (°C)	T_s	10	aquifer data	[56]
Depth to top of aquifer (m)	D	3000	aquifer data	[66, 82]
Depth from aquifer to bedrock (m)	B	5000	aquifer data	[75, 81, 82]
Net aquifer thickness (m)	H	200	aquifer data	[81, Plate 3A]
Length of trapping-model domain (km)	L_T	50	aquifer data	Fig. S13
Length of pressure-model domain (km)	L_{pres}	200	aquifer data	Fig. S13
Width of well array (km)	W	100	aquifer data	Fig. S13
Porosity	ϕ	0.2	estimated	[81, Fig.30]
Caprock slope (degrees)	ϑ	2	calculated	[82]
Darcy velocity (cm/yr)	U	10 ^a	calculated	[82, Fig.15]
Aquifer permeability (mD)	k_{aq}	100 ^b	calculated	[81, Figs.33,46]
Mean vertical permeability (mD)	k_{cap}	0.01	estimated	[36–38]
Lateral overburden permeability (mD)	\bar{k}_x	50	calculated	Fig. S4
Vertical overburden permeability (mD)	\bar{k}_z	0.02	calculated	Fig. S4
Salinity (g/L)	s	35	aquifer data	[82, Fig.19]
CO ₂ solubility (volume fraction)	χ_v	0.07	calculated	[6, 25]
Brine density (kg/m ³)	ρ_w	1000	calculated	[24]
CO ₂ density (kg/m ³)	ρ_g	600	calculated	[22]
Brine density change from diss. (kg/m ³)	$\Delta\rho_d$	10	calculated	[28, 59]
Brine viscosity (mPa s)	μ_w	0.4	calculated	[24]
CO ₂ viscosity (mPa s)	μ_g	0.05	calculated	[22]
Fracture pressure (MPa)	P_{frac}	60	calculated	Eq. S29,S28; [21]

^a In deep parts of the aquifer where we model sequestration, hydraulic head measurements are not available. As a result, we calculate the Darcy velocity based on head measurements in the shallower parts of the reservoir. While the actual velocity in the model domain is likely lower, the exact value of the Darcy velocity does not affect the capacity estimation since migration is driven dominantly by slope ($N_s/N_f \gg 1$).

^b Hydraulic conductivity data for the Navajo-Nugget Aquifer generally comes from outcrops or shallow wells, where it ranges from at least 0.03 to 3 m/day [81, Figs.33,46]. This corresponds to permeabilities in the range of about 40 to 4000 mD. Since regions suitable for sequestration are deeply buried, we set the permeability to a low value in this range.

5.6 Morrison Formation

The Morrison Formation occurs in the northwestern corner of New Mexico in the San Juan Basin, as shown in Figure S14. It consists of five members that have varying extents [83, p.48]. The bottom three members are the Salt Wash Member, the Recapture Member, and the Westwater Canyon Member. These members consist mainly of interbedded sandstone and claystone, and are the target members for sequestration in our study [84, p.135-155]. They are overlain by the Brushy Basin Member and the Jackpile Sandstone Member. The Brushy Basin member consists predominantly of claystone that contains varying amounts of silt and sand [84, p.135-156]. We take it to be the caprock in our study.

The Morrison Formation is underlain by the Wanakah Formation in the San Juan Basin. The uppermost member of this formation is the Todilto Member, which consists of limestone overlain by gypsum and anhydrite. The Wanakah Formation has been identified in previous hydrologic studies as a confining unit, and we take it to be the aquiclude in our study [83, p.54].

We model sequestration in the center of the San Juan Basin, as shown in Figure S15. The data for this region are shown in Table S16.

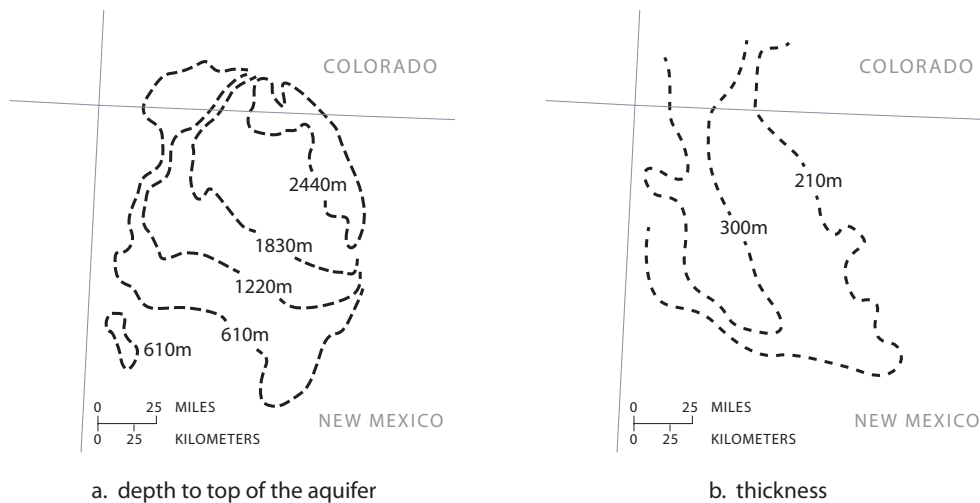


Figure S14: (a) The Morrison Formation deepens toward a northwest-southeast axis in the northeastern part of the San Juan Basin. Modified from [85, Fig.6]. (b) It thickens toward a north-south axis in the western part of the basin. Modified from [85, Fig.5].

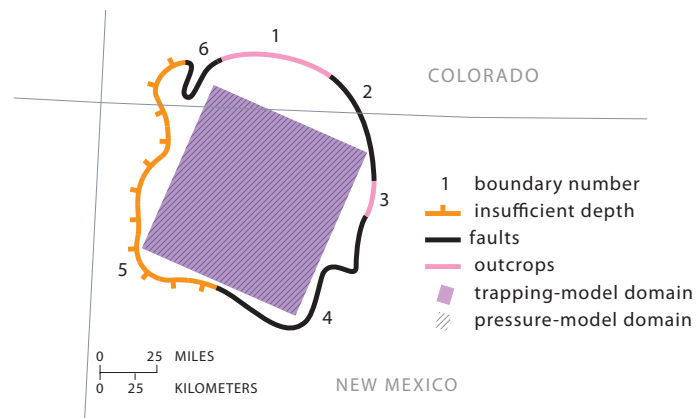


Figure S15: We identify six boundaries that constrain the portion of the Morrison Formation that is suitable for sequestration. Boundaries 1 and 3 correspond to outcrops, and Boundary 5 corresponds to where the depth to the top of the formation becomes less than 800 m [85, Fig.6]. Boundaries 2, 4, and 6 exclude major faults or fault systems in the San Juan Basin from the study area [83, Fig.7].

Table S16: Parameters for the Morrison Formation.

Parameter	Symbol	Value	Data Source	Reference
Residual CO ₂ saturation	S_{rg}	0.3	estimated	[40, 51]
Connate water saturation	S_{wc}	0.4	estimated	[40, 51]
Endpoint relative permeability to CO ₂	k_{rg}^*	0.6	estimated	[40, 51]
Coefficient of CO ₂ -saturated-brine flux	α	0.01	estimated	[52, 53]
Compressibility (GPa ⁻¹)	c	0.1	estimated	[30, Table C1]
Undrained Poisson ratio	ν	0.3	estimated	[30, Table C1]
Geothermal gradient (°C/km)	G_T	30	aquifer data	[54, 55]
Surface temperature (°C)	T_s	10	aquifer data	[56]
Depth to top of aquifer (m)	D	2000 ^a	aquifer data	[85, Fig.6][84, Fig.29]
Depth from aquifer to bedrock (m)	B	1000	aquifer data	[75]
Net aquifer thickness (m)	H	200 ^b	aquifer data	[85, Fig.5][84, Fig.29]
Length of trapping-model domain (km)	L_T	100	aquifer data	Fig. S15
Length of pressure-model domain (km)	L_{pres}	100	aquifer data	Fig. S15
Width of well array (km)	W	100	aquifer data	Fig. S15
Porosity	ϕ	0.2	estimated	
Caprock slope (degrees)	ϑ	0.9	calculated	[85, Fig.7]
Darcy velocity (cm/yr)	U	8	calculated	[83, Fig.52][85, Fig.8]
Aquifer permeability (mD)	k_{aq}	70 ^c	calculated	[85, Fig.9]
Mean vertical permeability (mD)	k_{cap}	0.01	estimated	[36–38]
Lateral overburden permeability (mD)	\bar{k}_x	40	calculated	Fig. S4
Vertical overburden permeability (mD)	\bar{k}_z	0.02	calculated	Fig. S4
Salinity (g/L)	s	5	aquifer data	[85, Fig.15]
CO ₂ solubility (volume fraction)	χ_v	0.09	calculated	[25]
Brine density (kg/m ³)	ρ_w	1000	calculated	[24]
CO ₂ density (kg/m ³)	ρ_g	600	calculated	[22]
Brine density change from diss. (kg/m ³)	$\Delta\rho_d$	10	calculated	[28, 59]
Brine viscosity (mPa s)	μ_w	0.4	calculated	[24]
CO ₂ viscosity (mPa s)	μ_g	0.04	calculated	[22]
Fracture pressure (MPa)	P_{frac}	50	calculated	Eq. S29,S28; [21]

^a We calculate the depth of the target members—the Salt Wash Member, the Recapture Member, and the Westwater Canyon Member—by adding the depth of the Morrison Formation [85, Fig.6] to the thickness of the Brushy Basin Member [84, Fig.29], which is the topmost unit of the formation. We ignore the Jackpile Sandstone Member since it exists mainly in the southern part of the basin outside of the trapping model domain.

^b We calculate the thickness of the target members by subtracting the thickness of the Brushy Basin Member [84, Fig.29] from the thickness of entire the Morrison Formation [85, Fig.5].

^c We found only a few values of transmissivity within the model domain. To calculate permeability, we divide the transmissivity at each location by the aquifer thickness at that location to determine hydraulic conductivity, and then multiply that value by μ_w/ρ_w to get permeability.

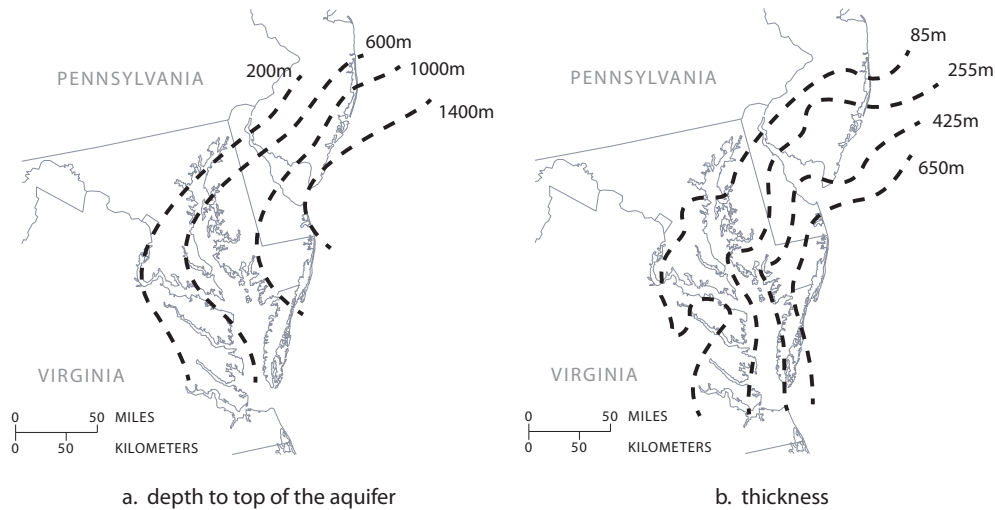


Figure S16: (a) The western limit of the aquifer is the Fall Line, where it pinches out against crystalline rock [87]. From the Fall Line, it dips and thickens seaward. (a) Modified from [47, Map c1potomac]. (b) Modified from [47, Map c3potomac].

5.7 Lower Potomac Aquifer

While the Lower Potomac Aquifer underlies almost the entire North Atlantic Coastal Plain, we study sequestration in Maryland and Delaware. Here it consists mostly of sediments deposited in fluvial or deltaic environments: it contains lenses of sand and gravel with interstitial clay [86, p.G30]. These lenses constitute between 20 and 60% of the aquifer thickness, and are interbedded with clayey and silty layers.

The aquifer is bounded above by a confining unit composed mostly of clay and sandy clay beds. It is bounded below by crystalline bedrock [86, 87].

While the Lower Potomac Aquifer extends under the Chesapeake Bay and the Atlantic Ocean, we study CO₂ storage only under the Delmarva Peninsula, as shown in Figure S17. The data for this region is shown in Table S17.

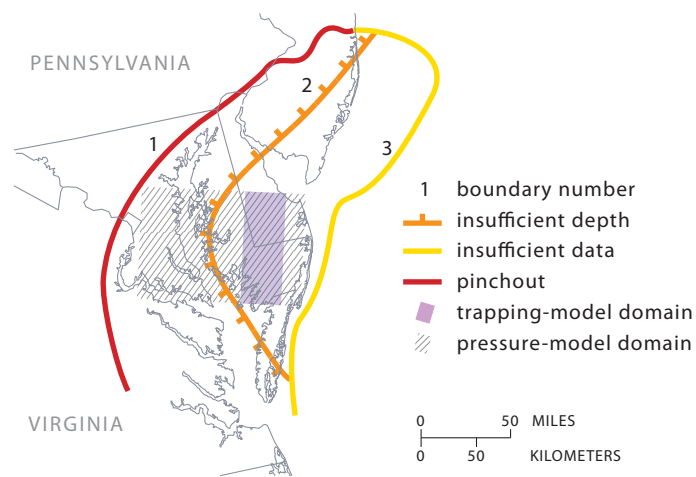


Figure S17: We identify 3 boundaries that constrain the portion of the Lower Potomac Aquifer that is suitable for sequestration. Boundary 1 corresponds to the Fall Line, where Coastal Plain sediments crop out or pinch out against the crystalline basement [86, Plate 1A,1B]. Since it is unclear whether the Lower Potomac pinches out or crops out in the study area, we choose this boundary to be a pinchout boundary to make our capacity estimates conservative. Boundary 2 corresponds to where the top of the aquifer becomes less than 800 m deep [47, Map c1potomac]. Boundary 3 corresponds to the limits of the aquifer depth and thickness maps [47, Maps c1potomac, c3potomac].

Table S17: Parameters for the Lower Potomac Aquifer.

Parameter	Symbol	Value	Data Source	Reference
Residual CO ₂ saturation	S_{rg}	0.3	estimated	[40, 51]
Connate water saturation	S_{wc}	0.4	estimated	[40, 51]
Endpoint relative permeability to CO ₂	k_{rg}^*	0.6	estimated	[40, 51]
Coefficient of CO ₂ -saturated-brine flux	α	0.01	estimated	[52, 53]
Compressibility (GPa ⁻¹)	c	0.1	estimated	[30, Table C1]
Undrained Poisson ratio	ν	0.3	estimated	[30, Table C1]
Geothermal gradient (°C/km)	G_T	30	aquifer data	[54, 55]
Surface temperature (°C)	T_s	10	aquifer data	[56]
Depth to top of aquifer (m)	D	1000	aquifer data	[47, Map c1potomac]
Depth from aquifer to bedrock (m)	B	0	aquifer data	[87, Fig.19,20]
Net aquifer thickness (m)	H	400	aquifer data	[47, Map c4potomac]
Length of trapping-model domain (km)	L_T	40	aquifer data	Fig. S17
Length of pressure-model domain (km)	L_{pres}	100	aquifer data	Fig. S17
Width of well array (km)	W	100	aquifer data	Fig. S17
Porosity	ϕ	0.2	estimated	
Caprock slope (degrees)	ϑ	0.3	calculated	[86, Plate 7B]
Darcy velocity (cm/yr)	U	10	calculated	[17, Table A.1]
Aquifer permeability (mD)	k_{aq}	3000	calculated	[17, Table A.1]
Mean vertical permeability (mD)	k_{cap}	0.1	estimated	[36–38]
Lateral overburden permeability (mD)	\bar{k}_x	2000	calculated	Fig. S4
Vertical overburden permeability (mD)	\bar{k}_z	0.2	calculated	Fig. S4
Salinity (g/L)	s	5	aquifer data	[87, Fig.57]
CO ₂ solubility (volume fraction)	χ_v	0.1	calculated	[25]
Brine density (kg/m ³)	ρ_w	1000	calculated	[24]
CO ₂ density (kg/m ³)	ρ_g	500	calculated	[22]
Brine density change from diss. (kg/m ³)	$\Delta\rho_d$	10	calculated	[28, 59]
Brine viscosity (mPa s)	μ_w	0.7	calculated	[24]
CO ₂ viscosity (mPa s)	μ_g	0.04	calculated	[22]
Fracture pressure (MPa)	P_{frac}	20	calculated	Eq. S29,S28; [21]

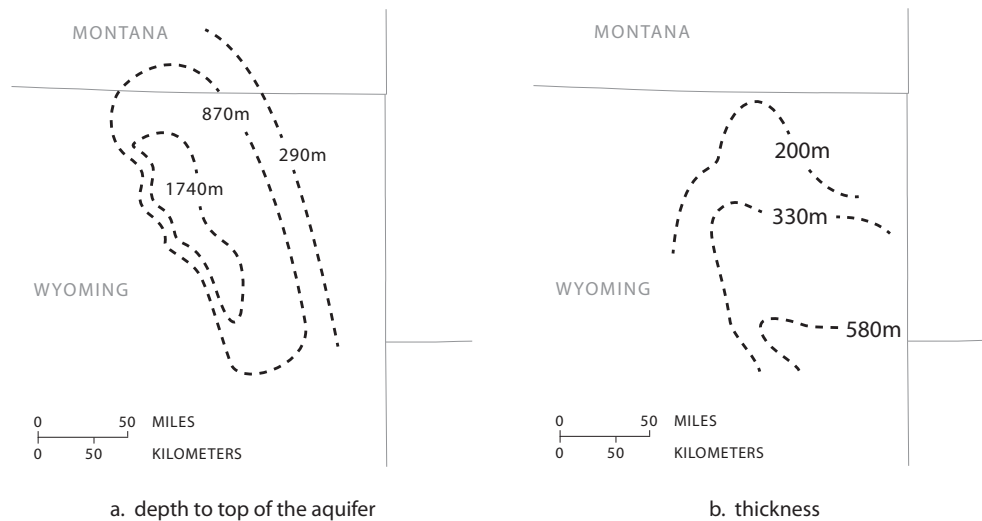


Figure S18: The Fox Hills Sandstone deepens along the axis of the Powder River Basin, which runs northwest to southeast. It thickens toward the southeast. (a) Modified from [47, Map c1foxhillsg]. (b) Modified from [47, Map c3foxhillsg].

5.8 Fox Hills Sandstone

The Fox Hills Sandstone occurs in the Powder River Basin, which is located in northeastern Wyoming. In general, it consists of massive, fine- to medium-grained sandstone with siltstone and minor shale, which are sometimes interbedded [88, p.T68]. The depth to the top of these rocks and their thickness are shown in Figure S18.

The Fox Hills Sandstone is conformably overlain by and intertongued with the Lance Formation in Wyoming, which provides an extensive top seal [44, p.82]. It is conformably underlain by marine shale and siltstone in the Lewis Shale or Pierre Shale, which forms an aquiclude [89, Plate II].

We model sequestration in the center of the Powder River Basin, as shown in Figure S19. The data for this region is shown in Table S18.

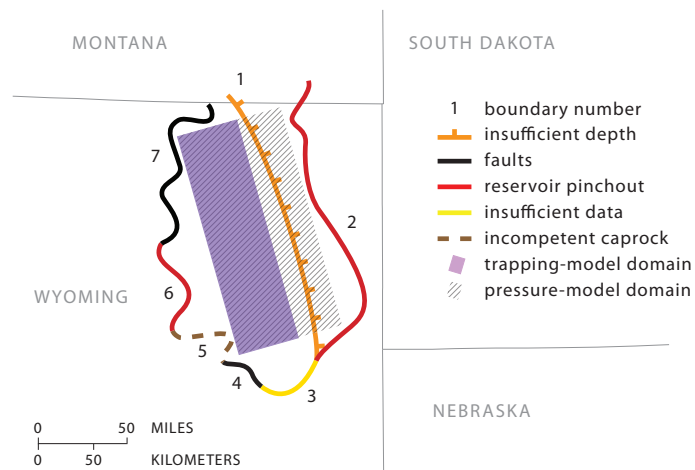


Figure S19: We identify 7 boundaries that constrain the portion of the Fox Hills Sandstone that is suitable for sequestration. Boundary 1 corresponds to where the top of the reservoir becomes less than 800 m deep [47, Map c1fohillsg]. Boundaries 2 and 6 correspond to where we interpret the reservoir to pinch out. While we found no cross sections of the reservoir at these locations, we base this interpretation on the observation that the caprock and rocks stratigraphically below the reservoir crop out contiguously there [79, Fig.56]. Boundary 3 corresponds to the limit of the reservoir depth and thickness maps [47, Maps c1fohillsg, c3fohillsg]. Boundaries 4 and 7 correspond to basin-scale faults [79, Fig.56]. Lastly, Boundary 5 corresponds to where the caprock contains more than 50% sand [47, Map 81fohillsg].

Table S18: Parameters for the Fox Hills Sandstone.

Parameter	Symbol	Value	Data Source	Reference
Residual CO ₂ saturation	S_{rg}	0.3	estimated	[40, 51]
Connate water saturation	S_{wc}	0.4	estimated	[40, 51]
Endpoint relative permeability to CO ₂	k_{rg}^*	0.6	estimated	[40, 51]
Coefficient of CO ₂ -saturated-brine flux	α	0.01	estimated	[52, 53]
Compressibility (GPa ⁻¹)	c	0.1	estimated	[30, Table C1]
Undrained Poisson ratio	ν	0.3	estimated	[30, Table C1]
Geothermal gradient (°C/km)	G_T	30	aquifer data	[54, 55]
Surface temperature (°C)	T_s	10	aquifer data	[56]
Depth to top of aquifer (m)	D	1000	aquifer data	[47, Map c1foxhillsg]
Depth from aquifer to bedrock (m)	B	4000	aquifer data	[75]
Net aquifer thickness (m)	H	200	aquifer data	[47, Map 4foxhills]
Length of trapping-model domain (km)	L_T	100	aquifer data	Fig. S19
Length of pressure-model domain (km)	L_{pres}	100	aquifer data	Fig. S19
Width of well array (km)	W	200	aquifer data	Fig. S19
Porosity	ϕ	0.2	estimated	
Caprock slope (degrees)	ϑ	1	calculated	[47, Map c1foxhillsg]
Darcy velocity (cm/yr)	U	10 ^a	calculated	[79, Fig.56], [90]
Aquifer permeability (mD)	k_{aq}	100	calculated	[90]
Mean vertical permeability (mD)	k_{cap}	.01	estimated	[36–38]
Lateral overburden permeability (mD)	\bar{k}_x	50	calculated	Fig. S4
Vertical overburden permeability (mD)	\bar{k}_z	0.02	calculated	Fig. S4
Salinity (g/L)	s	2	aquifer data	[79, Fig.57]
CO ₂ solubility (volume fraction)	χ_v	0.1	calculated	[25]
Brine density (kg/m ³)	ρ_w	1000	calculated	[24]
CO ₂ density (kg/m ³)	ρ_g	500	calculated	[22]
Brine density change from diss. (kg/m ³)	$\Delta\rho_d$	11	calculated	[28, 59]
Brine viscosity (mPa s)	μ_w	0.7	calculated	[24]
CO ₂ viscosity (mPa s)	μ_g	0.04	calculated	[22]
Fracture pressure (MPa)	P_{frac}	10	calculated	Eq. S29,S28; [21]

^a We calculate the Darcy velocity with Darcy's law, using a head gradient of 0.003 [79, Fig.56].

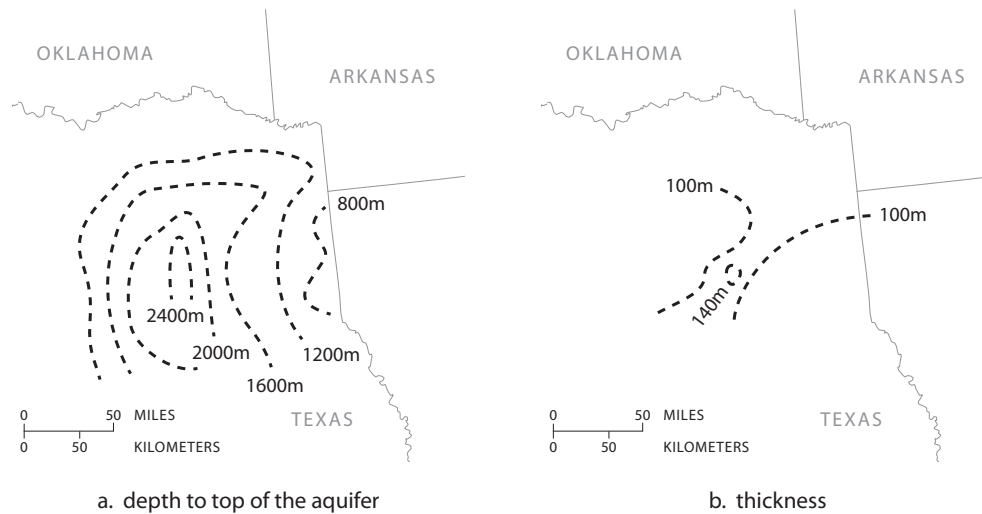


Figure S20: The Paluxy Formation deepens and thickens toward the center of the East Texas Basin. (a) Modified from [47, Map c1paluxyg]. (b) Modified from [47, Map c3paluxyg].

5.9 Paluxy Sandstone

While the Paluxy Formation is widespread throughout the Gulf Coastal Plain, we focus on deep parts of the formation in the East Texas Basin, which lies in northeastern Texas [91]. The depth to the top of the formation and its thickness is shown in Figure S20.

In the East Texas Basin, the Paluxy Formation is a quartz arenite, but in some areas can contain up to fifty percent clay [44, p.163]. It is overlain by the Goodland Limestone, which can be fairly porous and is likely a poor caprock. This limestone, however, is overlain by the Kiamichi Shale. We model this shale as the aquitard in our study and ignore the intervening Goodland Limestone since it is thin compared to the Paluxy Formation. The Paluxy is underlain by interbedded shale and limestone in the Glen Rose Formation, which we model as the aquiclude [91].

We model sequestration in the center of the East Texas Basin, as shown in Figure S21. The data for this region is shown in Table S19.

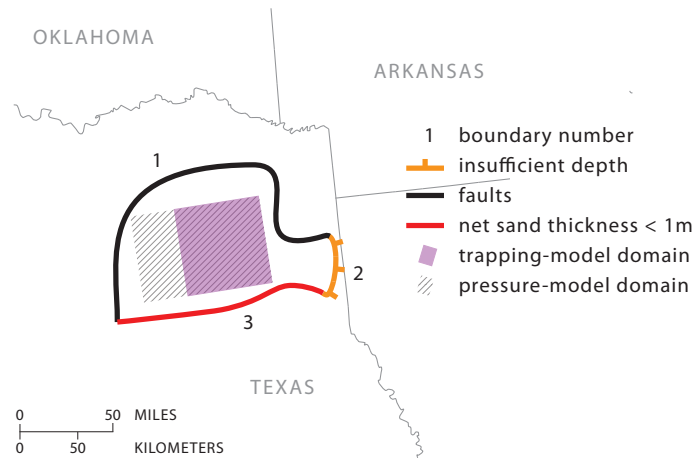


Figure S21: We identify three boundaries that constrain the portion of the Paluxy Sandstone that is suitable for sequestration. Boundary 1 corresponds to the edges of four major fault zones: the Mexia Fault Zone, the Talco Fault Zone, and the South Arkansas Fault Zone [91, Fig.3]. Boundary 2 corresponds to where the top of the formation becomes less than 800m deep [47, Map c1paluxyg]. Boundary 3 marks where the net sand thickness in the formation becomes less than 1m [47, Map c4paluxyg].

Table S19: Parameters for the Paluxy Sandstone.

Parameter	Symbol	Value	Data Source	Reference
Residual CO ₂ saturation	S_{rg}	0.3	estimated	[40, 51]
Connate water saturation	S_{wc}	0.4	estimated	[40, 51]
Endpoint relative permeability to CO ₂	k_{rg}^*	0.6	estimated	[40, 51]
Coefficient of CO ₂ -saturated-brine flux	α	0.01	estimated	[52, 53]
Compressibility (GPa ⁻¹)	c	0.1	estimated	[30, Table C1]
Undrained Poisson ratio	ν	0.3	estimated	[30, Table C1]
Geothermal gradient (°C/km)	G_T	30	aquifer data	[54, 55]
Surface temperature (°C)	T_s	20	aquifer data	[56]
Depth to top of aquifer (m)	D	2000	aquifer data	[47, Map c1paluxyg]
Depth from aquifer to bedrock (m)	B	6000	aquifer data	[75][47, Map c1paluxyg]
Net aquifer thickness (m)	H	15	aquifer data	[47, Map c3paluxyg]
Length of trapping-model domain (km)	L_T	70	aquifer data	Fig. S21
Length of pressure-model domain (km)	L_{pres}	100	aquifer data	Fig. S21
Width of well array (km)	W	80	aquifer data	Fig. S21
Porosity	ϕ	0.2	aquifer data	[47, Map 14paluxy]
Caprock slope (degrees)	ϑ	1	calculated	[47, Map c1paluxyg]
Darcy velocity (cm/yr)	U	5.0 ^a	estimated	
Aquifer permeability (mD)	k_{aq}	300	aquifer data	[47, Map 2paluxy]
Mean vertical permeability (mD)	k_{cap}	0.01	estimated	[36–38]
Lateral overburden permeability (mD)	\bar{k}_x	100	calculated	Fig. S4
Vertical overburden permeability (mD)	\bar{k}_z	0.02	calculated	Fig. S4
Salinity (ppm)	s	100000	aquifer data	[47, Map 12cpaluxy]
CO ₂ solubility (volume fraction)	χ_v	0.05	calculated	[25]
Brine density (kg/m ³)	ρ_w	1000	calculated	[24]
CO ₂ density (kg/m ³)	ρ_g	600	calculated	[22]
Brine density change from diss. (kg/m ³)	$\Delta\rho_d$	7	calculated	[28, 59]
Brine viscosity (mPa s)	μ_w	0.5	calculated	[24]
CO ₂ viscosity (mPa s)	μ_g	0.04	calculated	[22]
Fracture pressure (MPa)	P_{frac}	30	calculated	Eq. S29,S28; [21]

^a We found no data on Darcy velocity or hydraulic head in the Paluxy Formation. In the absence of data, we choose a reasonable value based on experience with other deep saline aquifers. Ultimately, this value is unimportant since slope dominates transport ($N_s/N_f \approx 200$).

5.10 St. Peter Sandstone

While the St. Peter Sandstone is widespread in the Mississippi River Valley, we model sequestration only in the Illinois Basin where it is sufficiently deep and well characterized. The structure of the formation in this basin is shown in Figure S22.

The stratigraphy of the St. Peter Sandstone is complicated. It consists of three members whose occurrence and size vary with location: the Kress Member, the Tonti Member, and the Starved Rock Sandstone Member. The Kress Member is the lowermost unit and is present only in central and northern Illinois Basin. It is composed of poorly-sorted, cherty conglomerate, clayey sandstone, and shale. The Tonti Member is the middle member and is generally the most widespread and thickest unit in the St. Peter. It is a fine-grained, very pure quartz arenite. The Starved Rock Sandstone is the uppermost member and is mostly present in the northern and central Illinois Basin. It is a quartz sandstone like the Tonti Member, but is medium-grained and more cross-bedded [42, 43].

The St. Peter Sandstone is overlain by at least four different formations or groups in different parts of the Illinois Basin: the Dutchtown Limestone [92, Fig.5-10], the Joachim Dolomite [92, Fig.5-11], the Platteville Group, and the Glenwood Formation [43, p.63]. While these rocks exhibit a variety of different lithologies, we take them as a group to be an aquitard because all of the rocks contain low-permeability layers. For example, the Dutchtown Limestone contains beds of shale; the Joachim Dolomite contains beds of shale, gypsum, and anhydrite; the Platteville Group contains beds of chert and shale; and the uppermost layer in the Glenwood Formation is composed of shale. Other authors have also suggested that at least some of these rocks will act as a caprock [42, 44]. If this assumption is wrong, the overlying Maquoketa Shale is a well-recognized caprock [42, 46].

The St. Peter Sandstone is underlain by a variety of rocks since its base is a major regional unconformity [43, Fig.O-13]. In the southernmost part of the Illinois Basin, it is underlain by

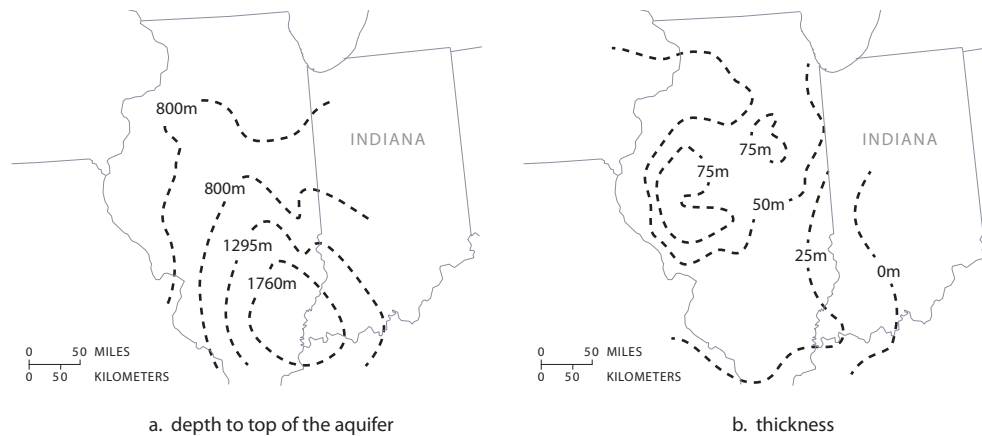


Figure S22: (a) The St. Peter Sandstone dips toward the center of the Illinois Basin in southern Illinois. Modified from [47, Map c1stpeter]. (b) Its thickness is highly variable due to irregularities in an unconformity at the base of the formation and post-depositional erosion [43, p.62]. In some areas, this erosion has completely removed the St. Peter. Modified from [47, Map c3stpeter].

the Everton Dolomite. In the northernmost part of the basin, it is underlain by the Cambrian Potosi Dolomite, Franconia Formation, and Eminance Formation. In most of the remaining parts of the region, the St. Peter is underlain by Ordovician rocks in the Prairie du Chien Group: the Shakopee Dolomite, the New Richmond Sandstone, the Oneota Dolomite, and the Gunter Sandstone [43, p.45-60]. Although we do not identify these rocks as a regional aquiclude, we do not consider them for sequestration since their geology is complex and can be very different from the overlying St. Peter Sandstone.

We model sequestration in southern Illinois, as shown in Figure S23. The data for this region are shown in Table S20.

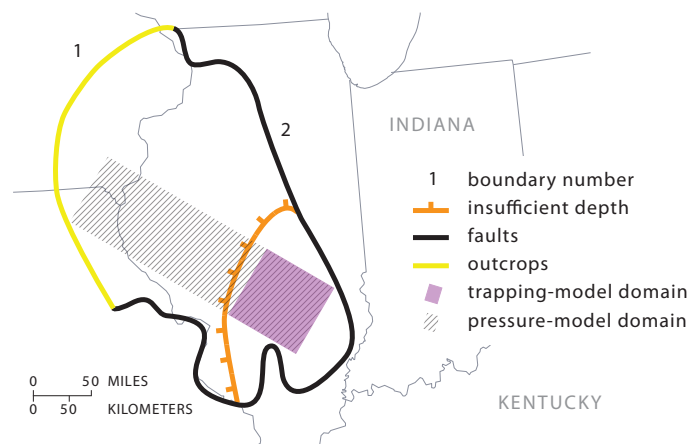


Figure S23: We identify two boundaries that constrain the portion of the St. Peter Sandstone in the Illinois Basin that is suitable for sequestration. Boundary 1 corresponds to the end of the available depth and formation thickness maps [47, Maps c1stpeter, c3stpeter]. Boundary 2 corresponds to basin-scale faults [50].

Table S20: Parameters for the St. Peter Sandstone.

Parameter	Symbol	Value	Data Source	Reference
Residual CO ₂ saturation	S_{rg}	0.3	estimated	[40, 51]
Connate water saturation	S_{wc}	0.4	estimated	[40, 51]
Endpoint relative permeability to CO ₂	k_{rg}^*	0.6	estimated	[40, 51]
Coefficient of CO ₂ -saturated-brine flux	α	0.01	estimated	[52, 53]
Compressibility (GPa ⁻¹)	c	0.1	estimated	[30, Table C1]
Undrained Poisson ratio	ν	0.3	estimated	[30, Table C1]
Geothermal gradient (°C/km)	G_T	20	aquifer data	[54, 55]
Surface temperature (°C)	T_s	10	aquifer data	[56]
Depth to top of aquifer (m)	D	2000	aquifer data	[47, Map c1stpeter]
Depth from aquifer to bedrock (m)	B	1000	aquifer data	[47, Map c1stpeter][75]
Net aquifer thickness (m)	H	40	aquifer data	[47, Map c1stpeter]
Length of trapping-model domain (km)	L_T	100	aquifer data	Fig. S23
Length of pressure-model domain (km)	L_{pres}	400	aquifer data	Fig. S23
Width of well array (km)	W	100	aquifer data	Fig. S23
Porosity	ϕ	0.06	calculated	[93]
Caprock slope (degrees)	ϑ	0.5	calculated	[47, Map c1stpeter]
Darcy velocity (cm/yr)	U	1	calculated	[46, Fig.27C]
Aquifer permeability (mD)	k_{aq}	50 ^a	aquifer data	[46, Fig.19C]
Mean vertical permeability (mD)	k_{cap}	0.01	estimated	[36–38]
Lateral overburden permeability (mD)	\bar{k}_x	30	calculated	Fig. S4
Vertical overburden permeability (mD)	\bar{k}_z	0.02	calculated	Fig. S4
Salinity (ppm)	s	100000	aquifer data	[94, Fig.13]
CO ₂ solubility (volume fraction)	χ_v	0.05	calculated	[6, 25]
Brine density (kg/m ³)	ρ_w	1000	calculated	[24]
CO ₂ density (kg/m ³)	ρ_g	800	calculated	[22]
Brine density change from diss. (kg/m ³)	$\Delta\rho_d$	8	calculated	[28, 59]
Brine viscosity (mPa s)	μ_w	1	calculated	[24]
CO ₂ viscosity (mPa s)	μ_g	0.07	calculated	[22]
Fracture pressure (MPa)	P_{frac}	30	calculated	Eq. S29,S28; [21]

^a We calculate permeability from mapped values of hydraulic conductivity that range from about 40 to 190 m/yr [46, Fig.19C]. To convert to permeability, we assume a density of 1000 kg/m³ and a viscosity of 0.5 mPa s.

5.11 Cedar Keys and Lawson Dolomites

The Lawson Formation and lower Cedar Keys Formation occur in Florida in the South Florida Basin. The depth to the top of these rocks and their thickness is shown in Figure S24.

The Lawson Formation consists of two members [95, Table 1]. Its lower member is mostly white chalk that is irregularly interbedded with chalky dolomite or dolomitic chalk. Its upper member is finely to coarsely crystalline dolomite that contains gypsum and anhydrite [65, p.G26-G27]. The Lawson Formation overlies unnamed carbonate beds of Taylor age. Over the Florida peninsula, these beds consist mostly of chalky dolomite interbedded with few beds of shale or marlstone [95]. We choose these beds to be the bottom boundary in our model since we found almost no information about them.

The Lawson Formation is unconformably overlain by the lower Cedar Keys Formation, which consists of limestone [65]. It is overlain by the middle Cedar Keys Formation, which consists of massively bedded anhydrite [44, p.72]. These anhydrite beds are nearly impermeable and are the caprock in our study [61].

We model sequestration in the center of the Florida peninsula, as shown in Figure S25. The data for this region is shown in Table S21.

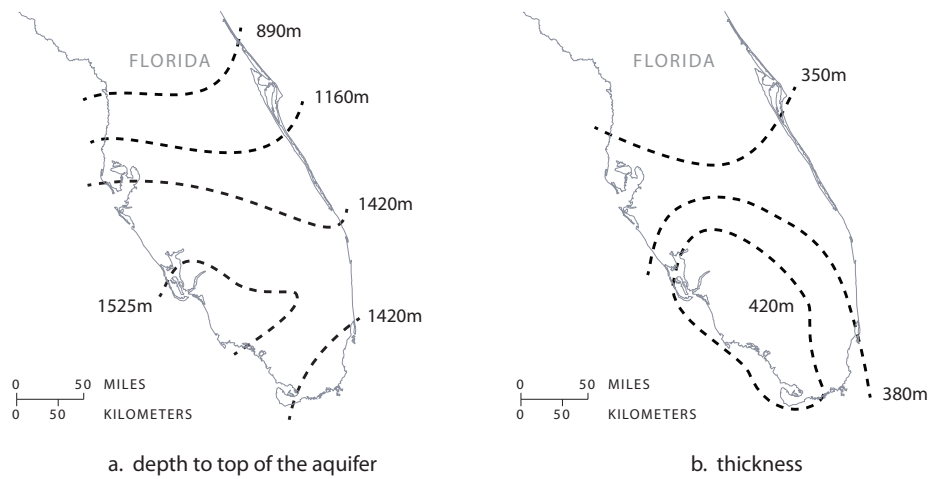


Figure S24: The Cedar Keys and Lawson Dolomites deepen and thicken toward the south-western part of the Florida peninsula. (a) Modified from [47, Map c1cedarkey]. (b) Modified from [47, Map c3cedarkeyg].

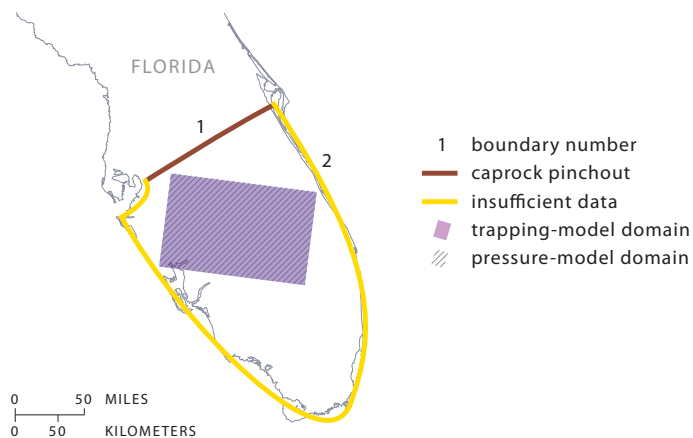


Figure S25: We identify 2 boundaries that constrain the portion of the Cedar Keys and Lawson Dolomites that is suitable for sequestration. Boundary 1 corresponds to the limit of the caprock for the overlying Floridan Aquifer. While maps show that the middle Cedar Keys Formation, which we take as the caprock in this study, does not pinchout here, we put a boundary for safety since the maps are likely very inaccurate [96]. Boundary 2 corresponds to the edges of the reservoir depth and thickness maps [47, Maps c1cedarkey, c3cedarkeyg].

Table S21: Parameters for the Cedar Keys and Lawson Dolomites.

Parameter	Symbol	Value	Data Source	Reference
Residual CO ₂ saturation	S_{rg}	0.3	estimated	[40, 51]
Connate water saturation	S_{wc}	0.4	estimated	[40, 51]
Endpoint relative permeability to CO ₂	k_{rg}^*	0.6	estimated	[40, 51]
Coefficient of CO ₂ -saturated-brine flux	α	0.01	estimated	[52, 53]
Compressibility (GPa ⁻¹)	c	0.1	estimated	[30, Table C1]
Undrained Poisson ratio	ν	0.3	estimated	[30, Table C1]
Geothermal gradient (°C/km)	G_T	20	aquifer data	[54, 55]
Surface temperature (°C)	T_s	20	aquifer data	[56]
Depth to top of aquifer (m)	D	2000	aquifer data	[47, Map c1cedarkey]
Depth from aquifer to bedrock (m)	B	2000	aquifer data	[75][47]
Net aquifer thickness (m)	H	400	aquifer data	[47, Map c3cedarkeyg]
Length of trapping-model domain (km)	L_T	100	aquifer data	Fig. S25
Length of pressure-model domain (km)	L_{pres}	100	aquifer data	Fig. S25
Width of well array (km)	W	200	aquifer data	Fig. S25
Porosity	ϕ	0.2	aquifer data	[44]
Caprock slope (degrees)	ϑ	0.2	calculated	[47, Map c1cedarkey]
Darcy velocity (cm/yr)	U	0 ^a	estimated	
Aquifer permeability (mD)	k_{aq}	10	aquifer data	[44]
Mean vertical permeability (mD)	k_{cap}	0.01	estimated	[36–38]
Lateral overburden permeability (mD)	\bar{k}_x	5	calculated	Fig. S4
Vertical overburden permeability (mD)	\bar{k}_z	0.02	calculated	Fig. S4
Salinity (g/L)	s	100 ^b	aquifer data	[44]
CO ₂ solubility (volume fraction)	χ_v	0.05	calculated	[25]
Brine density (kg/m ³)	ρ_w	1000	calculated	[24]
CO ₂ density (kg/m ³)	ρ_g	800	calculated	[22]
Brine density change from diss. (kg/m ³)	$\Delta\rho_d$	8	calculated	[28, 59]
Brine viscosity (mPa s)	μ_w	0.7	calculated	[24]
CO ₂ viscosity (mPa s)	μ_g	0.07	calculated	[22]
Fracture pressure (MPa)	P_{frac}	30	calculated	Eq. S29,S28; [21]

^a We found no data on Darcy velocity or hydraulic head in the Cedar Keys and Lawson Dolomites. In the absence of data, we set the Darcy velocity to zero. However, since the slope of the aquifer is small ($\theta = 0.18$), a nonzero velocity may change the results. For example, if the Darcy velocity has the same magnitude as that in the overlying Floridan aquifer ($U = 1.8$ cm/yr [61, Fig.60]), then $N_s/N_f = 2$ and ground water flow is not negligible.

^b We found no data on salinity in the Cedar Keys and Lawson Dolomites. However, some data are available for the overlying and underlying formations: brine in the overlying Upper Floridan Aquifer has a salinity of a few grams per liter [61, Fig.68], and brine in the underlying Sunniland Limestone has a salinity of a few hundred grams per liter. For the salinity of brine in the Cedar Keys and Lawson Dolomites, we choose a middle value of 100 g/L.

6 Sensitivity analysis

Because hydrogeologic data for saline aquifers are highly uncertain, we analyze the sensitivity of both the migration model and the pressure model to variations in their input parameters. We calculate the relative sensitivity of the capacity of an aquifer C to a parameter \mathcal{P} as:

$$\tilde{S} = \left. \frac{\mathcal{P}_0}{C_0} \frac{\partial C}{\partial \mathcal{P}} \right|_{\mathcal{P}_0}, \quad (\text{S30})$$

where \mathcal{P}_0 is the baseline value of the parameter and C_0 is the baseline capacity. The baseline for each aquifer is the set of parameter values given in the appropriate preceding section (*e.g.*, Table S22) and the corresponding capacity (Table S23). For the pressure model, the baseline values and the sensitivities depend on the injection time. We assess the sensitivity for each aquifer at three different injection times— $T = 50, 100,$ and 150 years—to define three baselines. These injection times bracket the key time horizon in our study, 100 years.

For both the migration model and the pressure model, the relative sensitivities vary between -1 and 2 within individual aquifers, indicating the relative importance of some parameters over others. For example, the migration model is highly sensitive to the width of the well array, W , the length of the model domain, L , and the aquifer thickness, H —key parameters for calculating an aquifer’s pore volume—but is relatively insensitive to the aquifer permeability, k_{aq} . The pressure model is highly sensitive to the aquifer depth, D , and the average density of the overburden, $\bar{\rho}_o$ —two key parameters for calculating the fracture pressure—but is relatively insensitive to salinity, s . All sensitivities for the migration model are listed in Table S22; all sensitivities for the pressure model are listed in Table S23.

Table S22: Sensitivity of the migration model to its input parameters.

Reservoir	Region	W	H	D	T_s	G	$\overline{p_w}$	s	k_{aq}	ϕ	S_{wc}	S_{gr}	k_{gr}^*	α	θ	U	L_T
Mt. Simon	a	1	0.49	0.71	0.1	-0.75	0.19	-0.73	0	1	-0.097	0.87	-0.85	0.54	-0.46	0	1.6
Mt. Simon	b	1	0.64	0.72	0.094	-0.53	0.17	-0.78	0.021	1	0.12	1.2	-0.82	0.37	-0.31	-0.021	1.4
Mt. Simon	c	1	1	0.74	0.17	-0.51	0.0052	-0.15	0.0071	1	-0.49	0.0086	-0.93	0	0.0071	0.17	1
Black Warrior River	a	1	0.77	0.77	0.19	-2.1	0.054	-0.34	0	1	0.44	1.7	-0.89	0.2	-0.2	0	1.2
Black Warrior River	b	1	0.88	0.56	0.14	-0.73	0.061	-0.069	0	1	-0.51	0.068	-0.76	0.069	-0.1	-0.013	1.1
Black Warrior River	c	1	0.91	0.46	0.14	-0.7	0.034	-0.028	0	1	-0.64	0.031	-0.92	-0.018	-0.078	0	0.98
Black Warrior River	d	1	0.94	0.73	0.22	-1.6	0.032	-0.18	0	1	0.65	2	-0.86	0.084	-0.056	0	1.1
Frio	a	1	0.99	1.7	0.27	-1.1	-0.0058	-0.14	0.0044	1	0.71	2.1	-0.77	0.014	-0.031	0	1
Frio	b	1	0.94	1.7	0.23	-1.2	0.025	-0.15	0	1	0.69	2.1	-0.76	0.038	-0.059	0	1
Frio	c	1	1	1.2	0.22	-1	0.011	-0.15	0.0012	1	0.72	2.1	-0.84	0.015	0.0091	0.0013	1
Madison	a	1	0.92	1.2	0.047	-0.59	0.064	-0.25	0.0067	1	0.6	1.9	-0.82	0.075	-0.067	-0.0013	1.1
Madison	b	1	0.78	1.5	-0.012	-0.75	0.15	-0.44	-0.017	1	0.53	1.7	-1	0.14	-0.16	-0.086	1.1
Navajo-Nugget	a	1	0.78	0.98	-0.035	-0.48	-0.034	-0.15	0	1	0.61	1.9	-0.83	0.13	-0.2	0	1.1
Navajo-Nugget	b	1	0.67	1.1	0.077	-0.54	0.22	-0.21	0	1	0.28	1.4	-0.76	0.36	-0.3	0	1.4
Morrison		1	0.56	1	0.085	-0.83	0.18	-0.056	0	1	0.1	1.2	-0.81	0.43	-0.4	0	1.5
Potomac		1	0.53	2.6	0.11	-2.3	0.17	-0.039	-0.0082	1	0.0031	1	-0.89	0.47	-0.44	0.011	1.5
Fox Hills		1	0.54	2.6	0.11	-2.3	0.16	-0.012	0	1	0.011	1	-0.88	0.46	-0.42	0	1.5
Paluxy		1	0.39	1.3	0.089	-1	0.52	-0.72	0	1	-0.31	0.54	-0.84	0.62	-0.55	0	1.7
St. Peter		1	0.89	0.26	0.073	-0.39	0.053	-0.29	0	1	-0.12	0.37	-0.66	0.036	-0.1	0	1
Cedar Keys		1	0.64	0.64	0.13	-0.5	0.17	-0.43	0	1	-0.36	0.31	-0.69	0.25	-0.33	0	1.3

Table S23: Sensitivity of the pressure model to its input parameters for three different injection times.

Reservoir	Region	T (years)	W	H	D	T _s	G	\bar{p}_w	s	k _{aq}	k _{cap}	c	ν	\bar{p}_o	B	L _{Pmin}	L _{Pmax}	
Mt. Simon	a	50	1	0.64	1.4	0.11	-0.027	-0.77	-0.16	0.5	0.18	0.32	0	1.8	0	0	0	0
		100	1	0.58	1.4	0.11	-0.013	-0.77	-0.17	0.5	0.21	0.29	0	1.8	0	0	0	0
		150	1	0.55	1.4	0.12	-0.0025	-0.77	-0.18	0.5	0.23	0.26	0	1.8	0	0	0	0
Mt. Simon	b	50	1	0.48	1.5	0.099	0.085	-0.77	-0.24	0.5	0.26	0.24	0	1.8	0	0	0	0
		100	1	0.41	1.5	0.1	0.092	-0.77	-0.25	0.5	0.3	0.2	0	1.8	0	0	0	0
		150	1	0.38	1.5	0.11	0.1	-0.77	-0.26	0.5	0.32	0.18	0	1.8	0	0	0	0
Mt. Simon	c	50	1	0.48	1.4	0.12	-0.049	-0.77	-0.26	0.5	0.26	0.24	0	1.8	0	0	0.00071	0
		100	1	0.43	1.4	0.12	-0.037	-0.77	-0.27	0.5	0.29	0.22	0	1.8	0	0	0.0075	0
		150	1	0.41	1.4	0.13	-0.027	-0.77	-0.26	0.5	0.32	0.21	0	1.8	0	0	0.025	0
Black Warrior River	a	50	1	0.77	1.3	0.17	-0.79	-0.77	-0.1	0.32	0.12	0.38	1.4	1.8	0	0	0	0
		100	1	0.73	1.1	0.12	-0.84	-0.77	-0.11	0.5	0.18	0.31	1.4	1.8	0	0	0	0
		150	1	0.68	0.87	0.081	-1.3	-0.77	-0.12	0.6	0.24	0.25	1.4	1.8	0	0	0	0
Black Warrior River	b	50	1	0.57	1.4	0.26	-0.18	-0.77	-0.032	0.46	0.23	0.27	1.4	1.8	0	0	0.038	0
		100	1	0.48	1.3	0.28	-0.15	-0.77	-0.035	0.4	0.3	0.2	1.4	1.8	0	0	0.097	-0.00087
		150	1	0.43	1.3	0.3	-0.13	-0.77	-0.038	0.37	0.36	0.14	1.4	1.8	0	0	0.13	-0.0033
Black Warrior River	c	50	1	0.46	1.4	0.26	-0.16	-0.77	-0.061	0.49	0.28	0.23	1.4	1.8	0	0	0.023	0.027
		100	1	0.42	1.3	0.26	-0.17	-0.77	-0.066	0.46	0.36	0.17	1.4	1.8	0	0	0.067	0.06
		150	1	0.39	1.2	0.26	-0.16	-0.77	-0.072	0.45	0.43	0.12	1.4	1.8	0	0	0.097	0.079
Black Warrior River	d	50	1	0.79	1.4	0.16	-0.61	-0.77	-0.086	0.5	0.11	0.39	1.4	1.8	0	0	0	0
		100	1	0.73	1.4	0.17	-0.59	-0.77	-0.092	0.5	0.15	0.35	1.4	1.8	0	0	0	0
		150	1	0.68	1.4	0.18	-0.57	-0.77	-0.098	0.5	0.19	0.31	1.4	1.8	0	0	0	0
Frio	a	50	1	0.7	2.1	0.18	-0.52	-0.77	-0.092	0.56	0.15	0.29	1.4	1.8	0	0	0	-0.18
		100	1	0.67	2.1	0.18	-0.45	-0.77	-0.094	0.62	0.17	0.21	1.4	1.8	0	0	0	-0.36
		150	1	0.66	2.2	0.19	-0.41	-0.77	-0.095	0.66	0.17	0.17	1.4	1.8	0	0	0	-0.47
Frio	b	50	1	0.59	2.1	0.19	-0.51	-0.77	-0.099	0.54	0.2	0.26	1.4	1.8	0	0	0	-0.12
		100	1	0.55	2.1	0.2	-0.45	-0.77	-0.1	0.59	0.22	0.18	1.4	1.8	0	0	0	-0.27
		150	1	0.54	2.1	0.2	-0.41	-0.77	-0.1	0.62	0.23	0.15	1.4	1.8	0	0	0	-0.36
Frio	c	50	1	0.51	1.8	0.19	-0.4	-0.77	-0.14	0.5	0.14	0.25	1.4	1.8	0	0	0	-0.00064
		100	1	0.47	1.8	0.19	-0.38	-0.77	-0.14	0.5	0.28	0.22	1.4	1.8	0	0	0	-0.011
		150	1	0.45	1.8	0.2	-0.36	-0.77	-0.15	0.51	0.31	0.18	1.4	1.8	0.00048	0	-0.032	
Madison	a	50	1	0.53	1.8	0.041	-0.031	-0.77	-0.13	0.49	0.23	0.27	0	1.8	0.0013	0	0.0042	
		100	1	0.45	1.8	0.042	-0.0052	-0.77	-0.14	0.5	0.26	0.24	0	1.8	0.015	0	0.031	
		150	1	0.4	1.8	0.043	-0.0027	-0.77	-0.14	0.5	0.26	0.24	0	1.8	0.036	0.00064	0.061	
Madison	b	50	1	0.46	1.1	0.056	-0.93	-0.77	-0.15	-0.35	0.26	0.23	0	1.8	0.011	0	0	
		100	1	0.39	1.1	0.057	-0.89	-0.77	-0.15	-0.32	0.27	0.22	0	1.8	0.06	0	0	
		150	1	0.36	1.1	0.057	-0.86	-0.77	-0.15	-0.29	0.27	0.22	0	1.8	0.1	0	0	
Navajo-Nugget	a	50	1	0.32	1.9	0.056	0.26	-0.77	-0.13	0.5	0.34	0.16	0	1.8	0	0	0.00044	
		100	1	0.28	1.9	0.057	0.27	-0.77	-0.13	0.5	0.36	0.14	0	1.8	0	0	0.0093	
		150	1	0.27	1.9	0.058	0.27	-0.77	-0.13	0.49	0.37	0.14	0	1.8	0	0	0.028	
Navajo-Nugget	b	50	1	0.43	1.6	0.087	0.005	-0.77	-0.12	0.33	0.29	0.21	0	1.8	0.14	0	0	
		100	1	0.43	1.6	0.087	0.0047	-0.77	-0.12	0.33	0.28	0.22	0	1.8	0.22	0	0	
		150	1	0.43	1.6	0.087	0.0044	-0.77	-0.12	0.34	0.29	0.21	0	1.8	0.26	0.00028	0.00055	
Morrison		50	1	0.36	1.8	0.11	0.063	-0.77	-0.031	0.5	0.3	0.2	0	1.8	0.041	0.16	0	
		100	1	0.31	1.9	0.11	0.061	-0.77	-0.03	0.5	0.3	0.2	0	1.8	0.11	0.26	0	
		150	1	0.27	1.9	0.11	0.065	-0.77	-0.031	0.5	0.3	0.2	0	1.8	0.15	0.32	0.00067	
Potomac		50	1	0.43	2.4	0.15	-1.3	-0.77	-0.022	0.29	0.32	0.39	0	1.8	0	0.2	0.4	
		100	1	0.31	2.2	0.17	-1.3	-0.77	-0.026	0.26	0.47	0.27	0	1.8	0	0.24	0.48	
		150	1	0.24	2.1	0.19	-1.3	-0.77	-0.029	0.25	0.57	0.18	0	1.8	0	0.25	0.49	
Fox Hills		50	1	0.36	2.6	0.15	-1.1	-0.77	-0.011	0.5	0.34	0.16	0	1.8	0	0.67	0	
		100	1	0.36	2.7	0.16	-1.1	-0.77	-0.012	0.5	0.39	0.11	0	1.8	0	0.65	0.00075	
		150	1	0.37	2.7	0.17	-1.1	-0.77	-0.012	0.5	0.42	0.08	0	1.8	0	0.63	0.0036	
Paluxy		50	1	0.27	1.7	0.16	-0.13	-0.77	-0.21	0.47	0.36	0.15	1.4	1.8	0	0.025	0.028	
		100	1	0.24	1.7	0.17	-0.14	-0.77	-0.23	0.44	0.38	0.15	1.4	1.8	0	0.072	0.06	
		150	1	0.23	1.7	0.17	-0.15	-0.77	-0.23	0.42	0.4	0.16	1.4	1.8	0.00051	0.11	0.081	
St. Peter		50	1	0.27	1.4	0.15	0.046	-0.77	-0.16	0.5	0.36	0.14	0	1.8	0.0022	0	0	
		100	1	0.24	1.4	0.15	0.049	-0.77	-0.16	0.5	0.37	0.13	0	1.8	0.017	0.00012	0	
		150	1	0.23	1.4	0.15	0.049	-0.77	-0.16	0.5	0.37	0.13	0	1.8	0.035	0.0015	0	
Cedar Keys		50	1	0.5	1.4	0.19	0.051	-0.77	-0.13	0.5	0.25	0.25	1.4	1.8	0	0	0	
		100	1	0.45	1.4	0.2	0.063	-0.77	-0.13	0.5	0.27	0.23	1.4	1.8	0.00079	0	0	
		150	1	0.43	1.4	0.2	0.069	-0.77	-0.14	0.5	0.28	0.22	1.4	1.8	0.0037	0	0	

7 Uncertainty analysis

7.1 Uncertainty in input parameters

To quantify uncertainty in the hydrogeologic properties of an aquifer, we estimate a low and high value for each input parameter using one of three methods. This is a simplification of hydrogeologic uncertainty, since in reality each parameter would be associated with a probability density function (PDF) of possible values. We use this simplified approach here because detailed PDFs are not available.

We estimate the low and high values of each parameter using one of three methods. For some parameters, such as surface temperature and geothermal gradient, we estimate an absolute uncertainty $\Delta\mathcal{P}$ and apply it symmetrically about the baseline value, so that the low and high values of a parameter \mathcal{P} with baseline value \mathcal{P}_0 will be $\mathcal{P}_{\text{low}} = \mathcal{P}_0 - \Delta\mathcal{P}/2$ and $\mathcal{P}_{\text{high}} = \mathcal{P}_0 + \Delta\mathcal{P}/2$, respectively (Table S24). For other parameters, such as aquifer depth and thickness, we estimate a relative uncertainty ψ and apply it symmetrically about the baseline value, so that the low and high values will be $\mathcal{P}_{\text{low}} = (1 - \psi/2)\mathcal{P}_0$ and $\mathcal{P}_{\text{high}} = (1 + \psi/2)\mathcal{P}_0$, respectively (Table S25). The remaining parameters—the groundwater velocity, compressibility, and permeability of the aquifer and caprock—are often assumed to be log-normally distributed, so we estimate a relative uncertainty Ψ in the log of the parameter. The corresponding low and high values will then be $\mathcal{P}_{\text{low}} = \mathcal{P}_0^{1+\Psi/2}$ and $\mathcal{P}_{\text{high}} = \mathcal{P}_0^{1-\Psi/2}$. We take the relative uncertainty in the log to be $\Psi = 0.03$ for all of these log-normally distributed parameters.

7.2 Uncertainty in capacity

Uncertainty in the hydrogeologic properties of an aquifer leads to uncertainty in its storage capacity. We using the low, baseline, and high values of each parameter estimated in the previous section to calculate the uncertainty in each aquifer’s storage capacity with two different methods.

Table S24: Parameters for which we estimate an absolute uncertainty, and corresponding absolute uncertainties $\Delta\mathcal{P}$.

Parameter	Symbol	$\Delta\mathcal{P}$
Connate water saturation [–]	S_{wc}	0.2
Residual CO ₂ saturation [–]	S_{gr}	0.2
Endpoint relative permeability to CO ₂ [–]	k_{gr}^*	0.2
Coefficient of CO ₂ -saturated-brine flux [–]	α	0.002
Average density of water in overburden [kg/m ³]	$\bar{\rho}_w$	20
Average density of overburden [kg/m ³]	$\bar{\rho}_o$	230
Surface temperature [°C]	T_s	1
Geothermal gradient [°C/km]	G	2

Table S25: Parameters for which we estimate a relative uncertainty, and corresponding relative uncertainties $\psi = \Delta\mathcal{P}/\mathcal{P}$.

Parameter	Symbol	ψ
Depth to top of aquifer	D	0.2
Depth from aquifer to bedrock	B	0.2
Net aquifer thickness	H	0.2
Width of well array	W	0.1
Length of model domain	L_t	0.1
Distance from well array to closest pressure boundary	L_{Pmin}	0.1
Distance from well array to farthest pressure boundary	L_{Pmax}	0.1
Porosity	ϕ	0.4
Caprock slope	ϑ	0.2
Salinity	s	0.1

In the Extrema Method, we calculate low and high values of the capacity by choosing the set of parameter values that will give the lowest capacity and the set that will give the highest capacity. To do so, we choose either the low or high value of each parameter as driven by the sensitivity analysis: to calculate the high capacity, for example, we take the high value of all parameters to which the capacity has a positive sensitivity, and the low value of all parameters to which the capacity has a negative sensitivity.

In the PDF Method, we generate a PDF for the capacity by estimating the capacity for every

possible combination of the low, baseline, and high values of the parameters. The uncertainty in the capacity is then the standard deviation of this PDF. Since using the migration and pressure models to calculate the capacity for every parameter combination is computationally infeasible, we instead extrapolate the capacity for each combination using the sensitivity analysis:

$$C = C_0 + \tilde{S}_{\mathcal{P}_1}\Delta\mathcal{P}_1 + \tilde{S}_{\mathcal{P}_2}\Delta\mathcal{P}_2 + \tilde{S}_{\mathcal{P}_3}\Delta\mathcal{P}_3 + \dots, \quad (\text{S31})$$

where the $\Delta\mathcal{P}_i = \mathcal{P}_i - \mathcal{P}_{i,0}$, $i = 1 \dots N$, are the uncertainties in the N input parameters and $\tilde{S}_{\mathcal{P}_i}$ are the associated sensitivities. Using Eq. (S31), we calculate a capacity for every possible combination of the low, baseline, and high values of each parameter for all $N = 16$ input parameters, generating $3^{16} \approx 43 \times 10^6$ values of capacity that compose the approximate PDF of capacity.

We calculate the uncertainties in the migration-limited capacity and the pressure-limited capacity independently. For the migration-limited capacity, the low capacities derived from the Extrema Method, C_l , are about 20–40% of the baseline capacity, and the high capacities, C_h , are about 200–350% of the baseline capacity (Table S26). From the PDF Method, the probability density functions are symmetric because the uncertainties in most of the input parameters are symmetric, and those with asymmetric uncertainties (Darcy velocity and permeability) exhibit low sensitivities (Figure S26). As a result, the mean capacities from these distributions, \bar{C} , are nearly the same as the baseline capacities, C_0 . One standard deviation, σ_C , is about 30 – 45% of the baseline capacity, and the upper end of the uncertainty window calculated from one standard deviation— $\bar{C} + \sigma_C$ —is then about 130 to 145% of the baseline capacity (Table S26).

We use one standard deviation as the appropriate measure of uncertainty from the PDF Method for both migration-limited and pressure-limited capacities. We do not use two standard deviations because the uncertainty window derived from two standard deviations is typically large to the point of being meaningless: for most of the well arrays, the lower end of the uncer-

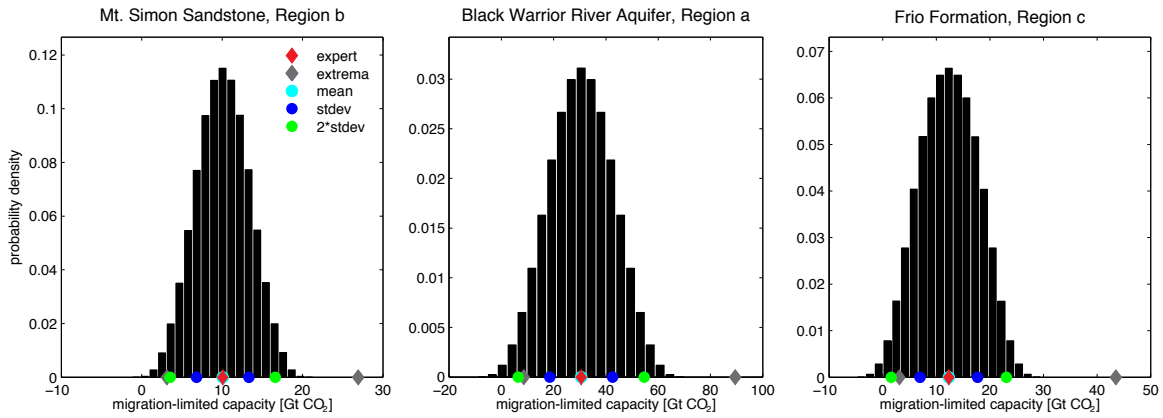


Figure S26: Approximate probability density functions for the migration-limited capacity of three well arrays.

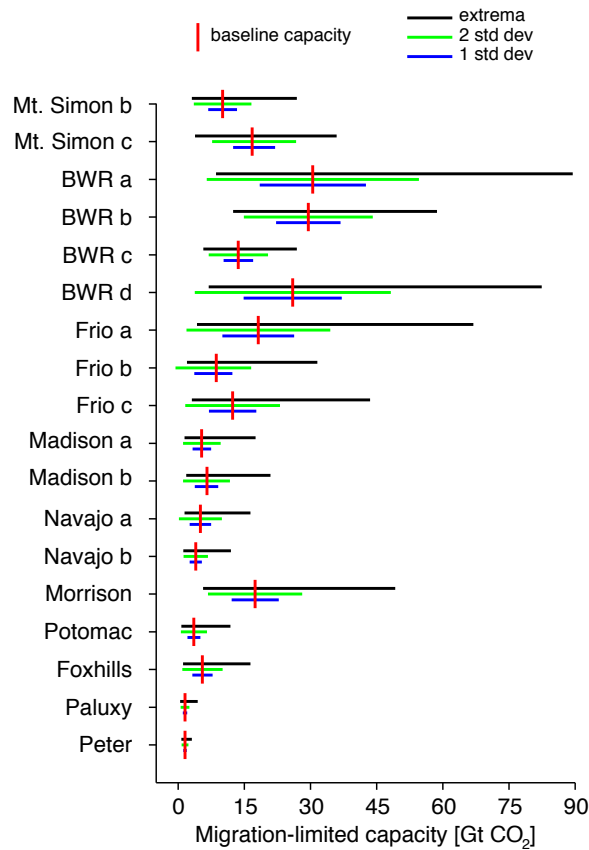


Figure S27: The baseline migration-limited capacity and three measures of uncertainty for nearly all the well arrays in the study. We do not show Mt. Simon, Region a or Cedar Keys because their baseline capacities and uncertainties are so large that the data for other aquifers becomes obscured.

Table S26: Uncertainty in migration-limited capacity.

Reservoir	Region	C_0	\bar{C}	$\frac{\bar{C}-C_0}{C_0}$	σ_C	$\frac{\sigma_C}{C_0}$	C_l	$\frac{C_l-C_0}{C_0}$	C_h	$\frac{C_h-C_0}{C_0}$
Mt. Simon	a	88	88	0	27	0.31	29	-0.67	250	1.8
Mt. Simon	b	10	10	0	3.3	0.32	3.1	-0.69	27	1.7
Mt. Simon	c	17	17	0.027	4.8	0.28	3.8	-0.77	36	1.1
Black Warrior River	a	31	31	0	12	0.39	8.6	-0.72	89	1.9
Black Warrior River	b	30	30	0	7.3	0.25	12	-0.58	59	0.99
Black Warrior River	c	14	14	0	3.4	0.25	5.7	-0.58	27	0.97
Black Warrior River	d	26	26	0	11	0.43	6.9	-0.73	82	2.2
Frio	a	18	18	0	8.1	0.45	4.3	-0.77	67	2.7
Frio	b	8.6	8	-0.075	4.3	0.5	2	-0.76	32	2.7
Frio	c	12	12	0	5.4	0.44	3.1	-0.75	44	2.5
Madison	a	5.3	5.4	0.015	2.1	0.4	1.4	-0.73	18	2.3
Madison	b	6.6	6.4	-0.016	2.7	0.41	1.8	-0.72	21	2.2
Navajo-Nugget	a	5.1	5.1	0	2.4	0.48	1.4	-0.72	16	2.2
Navajo-Nugget	b	4	4	0	1.4	0.35	1.2	-0.7	12	2
Morrison		17	17	0	5.3	0.31	5.7	-0.68	49	1.8
Potomac		3.6	3.6	0.0038	1.5	0.42	0.74	-0.79	12	2.3
Foxhills		5.5	5.5	0	2.3	0.42	1.1	-0.79	16	2
Paluxy		1.5	1.5	0	0.5	0.32	0.47	-0.7	4.4	1.9
St. Peter		1.6	1.6	0	0.38	0.24	0.72	-0.55	3.1	0.97
Cedar Keys		87	87	0	22	0.25	38	-0.57	180	1.1

tainty window is below the low capacity from the Extrema Method, and in at least one case goes to zero (Figures S27 & S29). Indeed, the approximate probability density functions from which they are calculated often reach into negative capacities, indicating that the lower ends of the uncertainty windows derived from them are also too low (Figures S26 & S28). The upper ends of the uncertainty windows are likely also too low, since the high capacity from the Extrema Method suggests that the true probability density function is skewed to the right.

For the pressure-limited capacity, the low capacities derived from the Extrema Method are generally 30% of the baseline capacity, and the high capacities are generally 300 to 400% of the baseline capacity (Table S27). Compared with the migration-limited capacity, the high capacities are typically a larger fraction of the baseline capacity because the pressure model has more

input parameters with large uncertainty, such as the compressibility and caprock permeability, and is more sensitive to the shared parameters with large uncertainties, such as the aquifer permeability. These parameters with large-uncertainties also have asymmetric uncertainties, and cause the capacity distributions obtained from the PDF Method to be asymmetric and often multi-peaked (Figure S28). As a result, the mean capacities from these distributions, \bar{C} , are different from the baseline capacities, C_0 (Figure S29). One standard deviation, σ_C , is about 50 – 60% of the baseline capacity, leading to error windows that are about 100 – 120% of the baseline capacity (Table S27).

We extend the uncertainty results from one injection time to all injection times by prorating. We calculate the high and low capacities from the Extrema Method at all injection times as:

$$C_l(T) = C_0(T) \frac{C_l(100 \text{ yrs})}{C_0(100 \text{ yrs})}, \quad C_h(T) = C_0(T) \frac{C_h(100 \text{ yrs})}{C_0(100 \text{ yrs})}, \quad (\text{S32})$$

where $C_l(T)$ and $C_h(T)$ are the low and high capacities at any injection time, T , respectively; $C_l(100 \text{ yrs})$ and $C_h(100 \text{ yrs})$ are the low and high capacities for an injection time of 100 years, respectively; and $C_0(100 \text{ yrs})$ is the baseline capacity for an injection time of 100 years. We choose to prorate based on the results at 100 years because that is the important time horizon in our study; the results obtained by prorating from an average of the results at 50, 100, and 150 years are extremely similar. We calculate the uncertainty window from the PDF Method at all injection times as:

$$C_{\mp\sigma}(T) = C_0(T) \frac{\bar{C}(100 \text{ yrs}) \mp \sigma_C(100 \text{ yrs})}{C_0(100 \text{ yrs})}, \quad (\text{S33})$$

where $C_{-\sigma}(T)$ and $C_{+\sigma}(T)$ are, respectively, the lower and upper ends of the uncertainty window based on one standard deviation at all injection times, T ; $\bar{C}(100 \text{ yrs})$ is the mean capacity at an injection time of 100 years; and $\sigma_C(100 \text{ yrs})$ is the standard deviation at an injection time of 100 years.

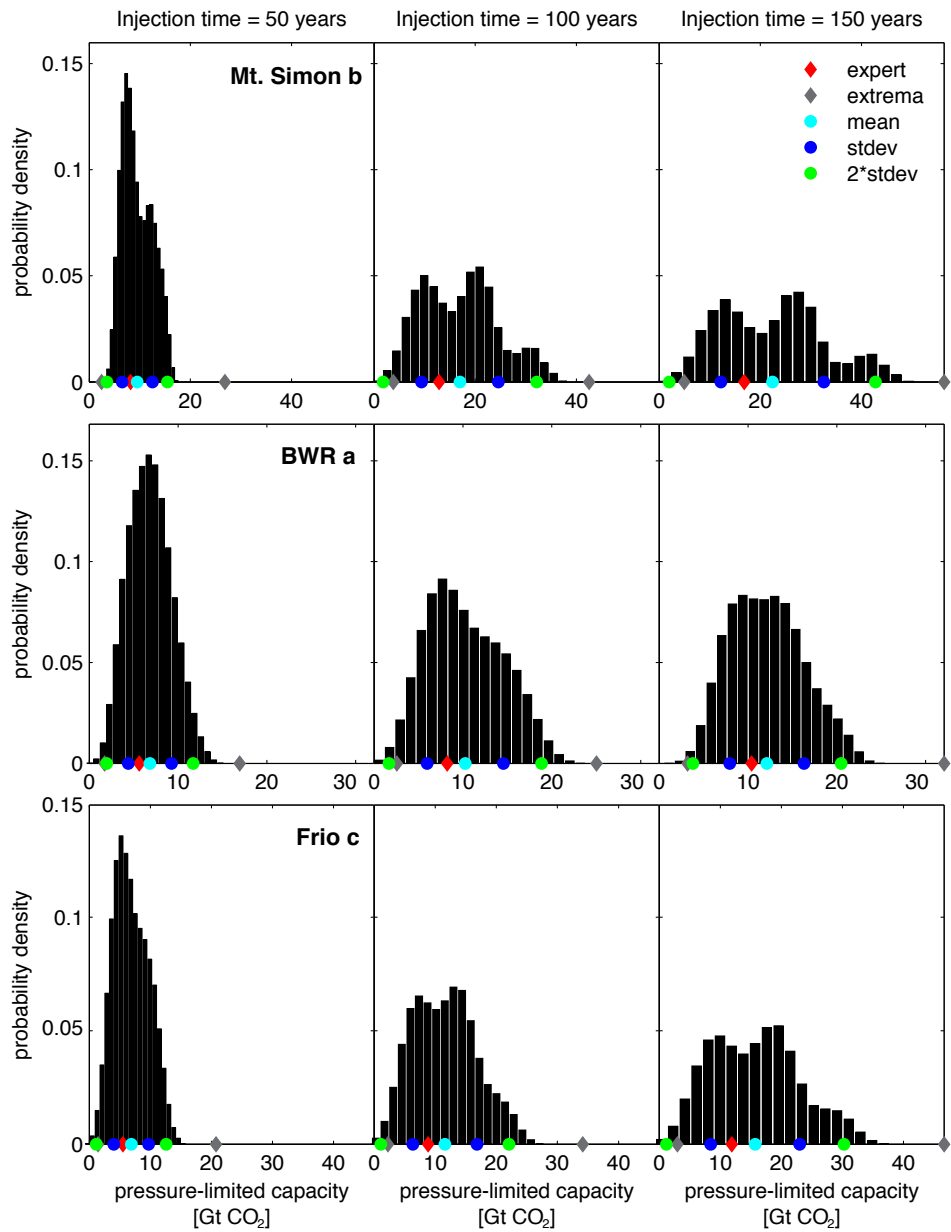


Figure S28: Approximate probability density functions for the pressure-limited capacity of three well arrays.

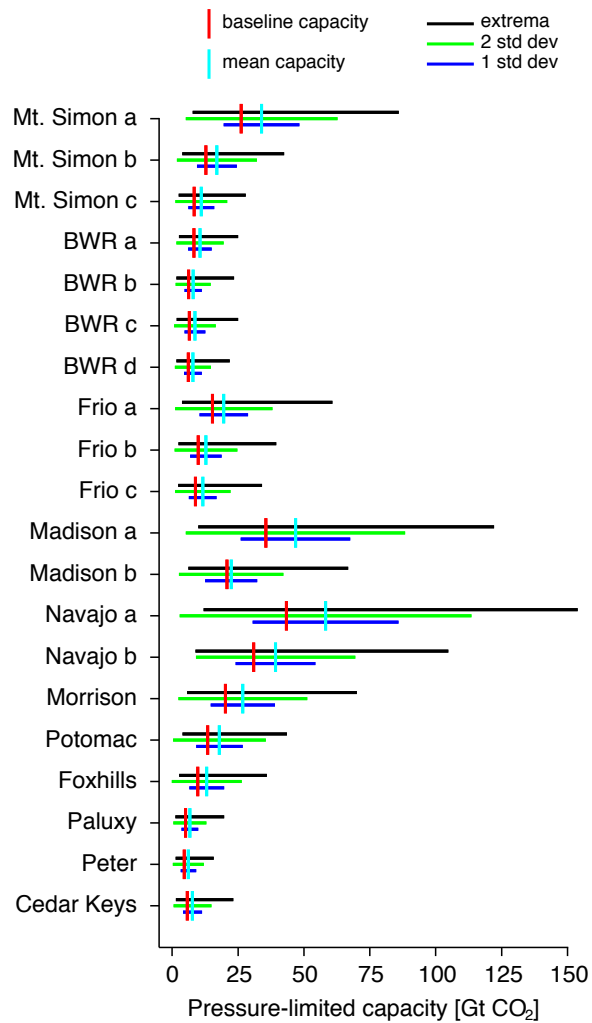


Figure S29: The baseline and mean pressure-limited capacity with three measures of uncertainty for all well arrays.

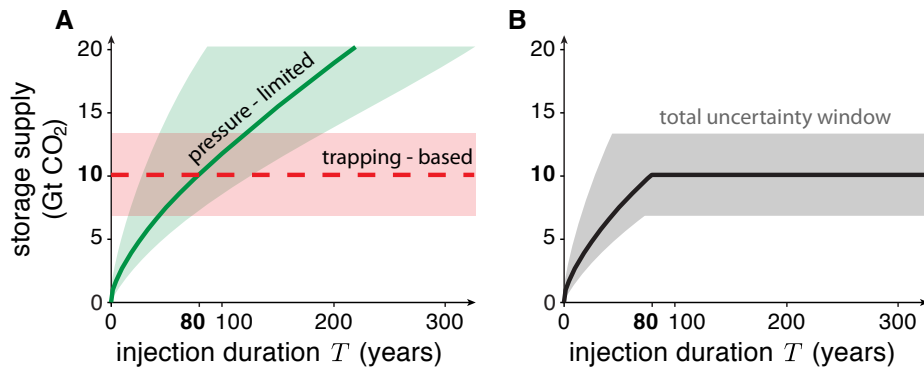


Figure S30: **(A)** The migration-limited and pressure-limited capacity for Region b of the Mt. Simon Sandstone, with uncertainty windows based on one standard deviation of the approximate PDF. **(B)** The total uncertainty window combines the uncertainties from both types of capacity. The upper boundary of the window corresponds to the lowermost of the two upper boundaries, and the lower boundary corresponds to the lowermost of the two lower boundaries.

To construct the complete uncertainty window for a particular aquifer, we combine the uncertainties from the migration-limited and pressure-limited capacities, as shown in Figure S30. To construct the complete uncertainty window for the entire US storage supply, we combine the uncertainties from all the aquifers.

Table S27: Uncertainty in pressure-limited capacity.

Reservoir	Region	T	C_0	\bar{C}	$\frac{\bar{C}-C_0}{C_0}$	σ_C	$\frac{\sigma_C}{C_0}$	C_l	$\frac{C_l-C_0}{C_0}$	C_h	$\frac{C_h-C_0}{C_0}$
Mt. Simon	a	50	16	21	0.29	8.8	0.54	4.9	-0.7	53	2.2
		100	26	34	0.3	14	0.55	7.8	-0.7	86	2.3
		150	35	46	0.3	20	0.56	10	-0.7	120	2.3
Mt. Simon	b	50	8.2	11	0.31	4.7	0.57	2.4	-0.7	27	2.3
		100	13	17	0.32	7.6	0.59	3.8	-0.7	43	2.3
		150	17	22	0.33	10	0.61	5	-0.71	56	2.3
Mt. Simon	c	50	4.9	6.4	0.31	2.8	0.57	1.5	-0.7	16	2.3
		100	8.4	11	0.32	4.9	0.59	2.5	-0.71	28	2.3
		150	12	15	0.33	7	0.61	3.4	-0.71	39	2.4
Black Warrior River	a	50	5.6	6.8	0.21	2.4	0.43	1.7	-0.69	17	2
		100	8.2	11	0.28	4.5	0.54	2.6	-0.69	25	2
		150	10	14	0.33	6.6	0.63	3.2	-0.69	32	2.1
Black Warrior River	b	50	3.7	4.8	0.28	2	0.53	0.98	-0.74	14	2.7
		100	6.2	8	0.29	3.3	0.53	1.6	-0.74	23	2.8
		150	8.5	11	0.3	4.8	0.57	2.2	-0.75	33	2.9
Black Warrior River	c	50	3.8	5	0.3	2.2	0.56	1	-0.74	14	2.8
		100	6.6	8.7	0.32	4	0.61	1.7	-0.74	25	2.8
		150	9.1	12	0.34	6	0.66	2.3	-0.75	35	2.9
Black Warrior River	d	50	4.3	5.5	0.27	2.4	0.55	1.2	-0.72	15	2.4
		100	6.1	7.9	0.28	3.4	0.56	1.7	-0.73	22	2.6
		150	7.7	10	0.29	4.4	0.56	2.1	-0.73	28	2.6
Frio	a	50	9.2	12	0.27	5.2	0.56	2.3	-0.75	35	2.8
		100	15	20	0.28	9.2	0.6	3.7	-0.76	61	3
		150	21	28	0.28	13	0.62	5	-0.77	87	3
Frio	b	50	5.9	7.5	0.28	3.3	0.57	1.5	-0.75	23	2.8
		100	9.9	13	0.29	6	0.6	2.4	-0.76	40	3
		150	14	18	0.3	8.6	0.62	3.3	-0.76	56	3.1
Frio	c	50	5.5	6.9	0.25	2.9	0.52	1.4	-0.74	21	2.8
		100	8.8	12	0.31	5.2	0.59	2.3	-0.75	34	2.9
		150	12	16	0.32	7.3	0.61	3	-0.75	47	2.9
Madison	a	50	21	28	0.31	12	0.57	6	-0.72	74	2.5
		100	36	47	0.32	21	0.58	9.9	-0.72	120	2.4
		150	48	63	0.32	28	0.59	13	-0.72	160	2.4
Madison	b	50	13	14	0.065	6.5	0.48	3.9	-0.71	44	2.3
		100	21	22	0.077	9.9	0.48	6.1	-0.71	67	2.2
		150	27	29	0.086	12	0.46	7.9	-0.71	86	2.2
Navajo-Nugget	a	50	25	34	0.34	16	0.63	7.1	-0.72	90	2.5
		100	43	58	0.34	28	0.64	12	-0.72	150	2.6
		150	59	80	0.35	38	0.64	16	-0.73	210	2.6
Navajo-Nugget	b	50	18	23	0.27	9.1	0.49	5.2	-0.72	64	2.4
		100	31	39	0.27	15	0.49	8.8	-0.72	100	2.4
		150	41	53	0.27	21	0.5	12	-0.71	140	2.4
Morrison		50	12	16	0.33	7.3	0.6	3.4	-0.72	42	2.5
		100	20	27	0.33	12	0.6	5.7	-0.72	70	2.5
		150	27	36	0.33	16	0.61	7.6	-0.72	94	2.5
Potomac		50	9.5	12	0.29	5.2	0.55	2.9	-0.7	29	2.1
		100	13	18	0.33	8.8	0.65	4	-0.71	44	2.2
		150	17	24	0.37	13	0.75	4.9	-0.71	58	2.3
Fox Hills		50	5.8	7.8	0.34	3.8	0.65	1.6	-0.72	21	2.6
		100	9.7	13	0.35	6.6	0.68	2.7	-0.73	36	2.7
		150	13	18	0.36	9.4	0.71	3.6	-0.73	50	2.8
Paluxy		50	2.9	3.8	0.33	1.8	0.62	0.7	-0.76	11	2.9
		100	5	6.7	0.33	3.2	0.62	1.2	-0.75	20	2.9
		150	7	9.3	0.33	4.4	0.63	1.7	-0.75	27	2.9
St. Peter		50	2.5	3.4	0.35	1.6	0.64	0.7	-0.72	8.6	2.5
		100	4.5	6.2	0.35	3	0.65	1.3	-0.72	16	2.5
		150	6.5	8.8	0.36	4.2	0.65	1.8	-0.72	22	2.5
Cedar Keys		50	3.4	4.5	0.33	2.1	0.61	0.84	-0.75	14	3
		100	5.8	7.7	0.34	3.6	0.62	1.4	-0.76	23	3
		150	7.9	11	0.34	5	0.63	1.9	-0.76	32	3.1

8 Synopsis of aquifer data and storage capacities

Table S28: General ranges in the input parameters for both the pressure model and the trapping model. For errors in input parameters, see Tables S25 & S24.

Parameter	Symbol	Value	Data Source	Reference
Residual CO ₂ saturation	S_{rg}	0.2 – 0.4	experiments	[40, 51]
Connate water saturation	S_{wc}	0.3 – 0.5	experiments	[40, 51]
Endpoint relative permeability to CO ₂	k_{rg}^*	0.5 – 0.7	experiments	[40, 51]
Coefficient of CO ₂ -saturated-brine flux	α	0.01	estimated	[52, 53]
Compressibility (GPa ⁻¹)	c	4e-11 – 3e-10 ^a	experiments	[30, Table C1]
Undrained Poisson ratio	ν	0.28 – 0.33	experiments	[30, Table C1]
Geothermal gradient (°C/km)	G_T	15 – 40	nationwide data	[54, 55]
Surface temperature (°C)	T_s	0 – 21	nationwide data	[56]
Depth to top of aquifer (m)	D	800 – 3000 ^b	nationwide data	see text
Depth from aquifer to bedrock (m)	B	0 – 13,000	nationwide data	[75]
Net aquifer thickness (m)	H	≤ 500	nationwide data	see text
Length of trapping-model domain (km)	L_T	50 – 500	aquifer data	[97]
Length of pressure-model domain (km)	L_{pres}	50 – 500	nationwide data	[97]
Width of well array (km)	W	50 – 500	nationwide data	[97]
Porosity	ϕ	0 – 0.3	nationwide data	[19]
Caprock slope (degrees)	ϑ	0 – 2	nationwide data	see text
Darcy velocity (cm/yr)	U	0 – 10	nationwide data	[98, p.145]
Aquifer permeability (mD)	k_{aq}	10 – 1000	nationwide data	[19, 99]
Mean vertical permeability (mD)	k_{cap}	1e-8 – 1	experiments	[36–38]
Salinity (g/L)	s	0 – 450 ^c	nationwide data	[44]
CO ₂ solubility (volume fraction)	χ_v	0.01 – 0.14	$f(T, P, s)$	[25]
Brine density (kg/m ³)	ρ_w	959 – 1130	$f(T, P, s)$	[24]
CO ₂ density (kg/m ³)	ρ_g	200 – 800	$f(T, P)$	[22]
CO ₂ -saturated-brine density (kg/m ³)	ρ_s	969 – 1133	$f(T, P, s, \chi_v)$	[28]
Brine viscosity (mPa s)	μ_w	0.2 – 1.2	$f(T, P, s)$	[24]
CO ₂ viscosity (mPa s)	μ_g	0.03 – 0.07	$f(T, P)$	[22]
Fracture pressure (MPa)	P_{frac}	10 – 70	$f(\rho_o, \rho_w, D, \phi)$	Eq. S29,S28; [21]

^a Range for sandstones. The compressibility of limestone and mudstone are within this range (limestone, $c \approx 6e - 11$; mudstone, $c \approx 1e - 10$).

^b 800 m is the depth at which CO₂ changes from a gas to a supercritical fluid, assuming a hydrostatic pressure gradient and a geothermal gradient of 25° C/km. 3000 m is the depth below which the density of CO₂ nearly stops increasing, also assuming a hydrostatic pressure gradient and a geothermal gradient of 25° C/km. Since the storage efficiency stops increasing below 3000 m, the higher cost of drilling may preclude sequestration at greater depths [100].

^c Since we only found CO₂ solubility data for $0 \leq s \leq 200$ g/L ($0 \leq s \leq 4$ m), all parameters that are based on s are calculated within this range.

Table S29: Storage capacities for every aquifer we study at different injection times, T . Capacities written in bold are pressure limited; otherwise, they are migration limited.

Reservoir	Region	Storage capacity (Gt CO ₂) at different injection times, T (years)										
		$T = 25$	50	75	100	150	200	250	300	400	500	600
Mt. Simon	a	9.4 ^{+7.9} _{-2.4}	15 ⁺¹² _{-3.7}	19 ⁺¹⁶ _{-4.8}	23 ⁺²⁰ _{-5.9}	31 ⁺²⁶ _{-7.8}	37 ⁺³² _{-9.5}	44 ⁺³⁷ ₋₁₁	50 ⁺⁴² ₋₁₃	61 ⁺⁵² ₋₁₆	73 ⁺⁴³ ₋₁₈	84 ⁺³² ₋₂₃
Mt. Simon	b	4.8 ^{+4.4} _{-1.3}	7.5 ^{+5.8} ₋₂	9.8 ^{+3.6} ₋₃	10 ^{+3.3} _{-3.3}	10 ^{+3.3} _{-3.3}	10 ^{+3.3} _{-3.3}	10 ^{+3.3} _{-3.3}	10 ^{+3.3} _{-3.3}	10 ^{+3.3} _{-3.3}	10 ^{+3.3} _{-3.3}	10 ^{+3.3} _{-3.3}
Mt. Simon	c	2.7 ^{+2.5} _{-0.72}	4.5 ^{+4.1} _{-1.2}	6.1 ^{+5.6} _{-1.6}	7.7 ⁺⁷ ₋₂	11 ^{+9.7} _{-2.8}	13 ^{+8.6} _{-3.6}	16 ^{+5.9} _{-4.3}	17 ^{+5.2} _{-4.3}	17 ^{+5.2} _{-4.3}	17 ^{+5.2} _{-4.3}	17 ^{+5.2} _{-4.3}
Black Warrior River	a	3.8 ^{+3.2} ₋₁	5.6 ^{+4.6} _{-1.5}	7 ^{+5.8} _{-1.9}	8.2 ^{+6.8} _{-2.2}	10 ^{+8.6} _{-2.7}	12 ⁺¹⁰ _{-3.3}	14 ⁺¹² _{-3.8}	16 ⁺¹³ _{-4.3}	20 ⁺¹⁷ _{-5.3}	24 ⁺¹⁹ _{-6.3}	28 ⁺¹⁵ _{-9.2}
Black Warrior River	b	2.3 ^{+1.9} _{-0.58}	3.7 ^{+3.1} _{-0.93}	5.0 ^{+4.1} _{-1.3}	6.2 ^{+5.1} _{-1.6}	8.6 ⁺⁷ _{-2.1}	11 ⁺⁹ _{-2.7}	13 ⁺¹¹ _{-3.3}	16 ⁺¹³ _{-3.9}	20 ⁺¹⁷ ₋₅	25 ⁺¹² _{-6.2}	29 ^{+7.3} _{-7.3}
Black Warrior River	c	2.3 ^{+2.1} _{-0.65}	3.8 ^{+3.5} _{-1.1}	5.2 ^{+4.8} _{-1.5}	6.5 ⁺⁶ _{-1.8}	8.9 ^{+8.1} _{-2.5}	11 ^{+5.7} _{-3.2}	14 ^{+3.4} _{-3.8}	14 ^{+3.4} _{-3.4}	14 ^{+3.4} _{-3.4}	14 ^{+3.4} _{-3.4}	14 ^{+3.4} _{-3.4}
Black Warrior River	d	3.2 ^{+2.7} _{-0.87}	4.3 ^{+3.6} _{-1.2}	5.3 ^{+4.4} _{-1.5}	6.1 ^{+5.1} _{-1.7}	7.7 ^{+6.4} _{-2.1}	9.1 ^{+7.6} _{-2.5}	10 ^{+8.7} _{-2.9}	12 ^{+9.8} _{-3.2}	14 ⁺¹² _{-3.9}	17 ⁺¹⁴ _{-4.6}	19 ⁺¹⁶ _{-5.2}
Frio	a	5.9 ^{+5.2} _{-1.9}	9.2 ^{+8.1} ₋₃	12 ⁺¹¹ ₋₄	15 ⁺¹¹ _{-5.3}	18 ^{+8.2} _{-8.1}	18 ^{+8.2} _{-8.1}	18 ^{+8.2} _{-8.1}	18 ^{+8.2} _{-8.1}	18 ^{+8.2} _{-8.1}	18 ^{+8.2} _{-8.1}	18 ^{+8.2} _{-8.1}
Frio	b	3.7 ^{+3.3} _{-1.1}	5.9 ^{+5.3} _{-2.2}	8 ^{+4.3} _{-4.3}	8.6 ^{+3.7} _{-4.9}	8.6 ^{+3.7} _{-4.9}	8.6 ^{+3.7} _{-4.9}	8.6 ^{+3.7} _{-4.9}	8.6 ^{+3.7} _{-4.9}	8.6 ^{+3.7} _{-4.9}	8.6 ^{+3.7} _{-4.9}	8.6 ^{+3.7} _{-4.9}
Frio	c	3.6 ^{+3.2} ₋₁	5.5 ⁺⁵ _{-1.6}	7.3 ^{+6.6} ₋₂	8.9 ⁺⁸ _{-2.5}	12 ^{+5.7} ₋₅	12 ^{+5.4} _{-5.4}	12 ^{+5.4} _{-5.4}	12 ^{+5.4} _{-5.4}	12 ^{+5.4} _{-5.4}	12 ^{+5.4} _{-5.4}	12 ^{+5.4} _{-5.4}
Madison	a	5.3 ^{+2.2} ₋₂	5.3 ^{+2.2} ₋₂	5.3 ^{+2.2} ₋₂	5.3 ^{+2.2} ₋₂	5.3 ^{+2.2} ₋₂	5.3 ^{+2.2} ₋₂	5.3 ^{+2.2} ₋₂	5.3 ^{+2.2} ₋₂	5.3 ^{+2.2} ₋₂	5.3 ^{+2.2} ₋₂	5.3 ^{+2.2} ₋₂
Madison	b	6.6 ^{+2.6} _{-2.8}	6.6 ^{+2.6} _{-2.8}	6.6 ^{+2.6} _{-2.8}	6.6 ^{+2.6} _{-2.8}	6.6 ^{+2.6} _{-2.8}	6.6 ^{+2.6} _{-2.8}	6.6 ^{+2.6} _{-2.8}	6.6 ^{+2.6} _{-2.8}	6.6 ^{+2.6} _{-2.8}	6.6 ^{+2.6} _{-2.8}	6.6 ^{+2.6} _{-2.8}
Navajo-Nugget	a	5.1 ^{+2.4} _{-2.4}	5.1 ^{+2.4} _{-2.4}	5.1 ^{+2.4} _{-2.4}	5.1 ^{+2.4} _{-2.4}	5.1 ^{+2.4} _{-2.4}	5.1 ^{+2.4} _{-2.4}	5.1 ^{+2.4} _{-2.4}	5.1 ^{+2.4} _{-2.4}	5.1 ^{+2.4} _{-2.4}	5.1 ^{+2.4} _{-2.4}	5.1 ^{+2.4} _{-2.4}
Navajo-Nugget	b	4.0 ^{+1.4} _{-1.4}	4.0 ^{+1.4} _{-1.4}	4.0 ^{+1.4} _{-1.4}	4.0 ^{+1.4} _{-1.4}	4.0 ^{+1.4} _{-1.4}	4.0 ^{+1.4} _{-1.4}	4.0 ^{+1.4} _{-1.4}	4.0 ^{+1.4} _{-1.4}	4.0 ^{+1.4} _{-1.4}	4.0 ^{+1.4} _{-1.4}	4.0 ^{+1.4} _{-1.4}
Morrison		7.0 ^{+6.5} _{-1.9}	12 ⁺¹¹ _{-3.3}	16 ^{+6.8} _{-4.4}	17 ^{+5.3} _{-5.3}	17 ^{+5.3} _{-5.3}	17 ^{+5.3} _{-5.3}	17 ^{+5.3} _{-5.3}	17 ^{+5.3} _{-5.3}	17 ^{+5.3} _{-5.3}	17 ^{+5.3} _{-5.3}	17 ^{+5.3} _{-5.3}
Potomac		3.6 ^{+1.5} _{-1.5}	3.6 ^{+1.5} _{-1.5}	3.6 ^{+1.5} _{-1.5}	3.6 ^{+1.5} _{-1.5}	3.6 ^{+1.5} _{-1.5}	3.6 ^{+1.5} _{-1.5}	3.6 ^{+1.5} _{-1.5}	3.6 ^{+1.5} _{-1.5}	3.6 ^{+1.5} _{-1.5}	3.6 ^{+1.5} _{-1.5}	3.6 ^{+1.5} _{-1.5}
Fox Hills		3.0 ^{+3.1} _{-0.98}	4.7 ^{+3.1} _{-1.5}	5.5 ^{+2.3} _{-2.3}	5.5 ^{+2.3} _{-2.3}	5.5 ^{+2.3} _{-2.3}	5.5 ^{+2.3} _{-2.3}	5.5 ^{+2.3} _{-2.3}	5.5 ^{+2.3} _{-2.3}	5.5 ^{+2.3} _{-2.3}	5.5 ^{+2.3} _{-2.3}	5.5 ^{+2.3} _{-2.3}
Paluxy		1.5 ^{+0.5} _{-0.5}	1.5 ^{+0.5} _{-0.5}	1.5 ^{+0.5} _{-0.5}	1.5 ^{+0.5} _{-0.5}	1.5 ^{+0.5} _{-0.5}	1.5 ^{+0.5} _{-0.5}	1.5 ^{+0.5} _{-0.5}	1.5 ^{+0.5} _{-0.5}	1.5 ^{+0.5} _{-0.5}	1.5 ^{+0.5} _{-0.5}	1.5 ^{+0.5} _{-0.5}
St. Peter		1.4 ^{+0.55} _{-0.41}	1.6 ^{+0.38} _{-0.38}	1.6 ^{+0.38} _{-0.38}	1.6 ^{+0.38} _{-0.38}	1.6 ^{+0.38} _{-0.38}	1.6 ^{+0.38} _{-0.38}	1.6 ^{+0.38} _{-0.38}	1.6 ^{+0.38} _{-0.38}	1.6 ^{+0.38} _{-0.38}	1.6 ^{+0.38} _{-0.38}	1.6 ^{+0.38} _{-0.38}
Cedar Keys		2.1 ⁺² _{-0.58}	3.4 ^{+3.3} _{-0.97}	4.7 ^{+4.5} _{-1.3}	5.8 ^{+5.6} _{-1.6}	8 ^{+7.7} _{-2.3}	9.9 ^{+9.5} _{-2.8}	12 ⁺¹¹ _{-3.3}	14 ⁺¹³ _{-3.9}	17 ⁺¹⁷ _{-4.9}	21 ⁺²³ _{-5.8}	24 ⁺²³ _{-6.8}

References and Notes

- S1. International Energy Agency. Electricity generation by fuel in the United States (1972-2008). <http://www.iea.org/stats>.
- S2. US Energy Information Administration. Annual energy outlook 2010. Technical Report DOE/EIA-0383, 2010.
- S3. S. Bachu, D. Bonijoly, J. Bradshaw, R. Burruss, S. Holloway, N. P. Christensen, and O. M. Mathiassen. CO₂ storage capacity estimation: Methodology and gaps. *Int. J. Greenh. Gas Con.*, 1:430–443, 2007.
- S4. J. Bradshaw, S. Bachu, D. Bonijoly, R. Burruss, S. Holloway, N. P. Christensen, and O. M. Mathiassen. CO₂ storage capacity estimation: issues and development of standards. *Int. J. Greenh. Gas Con.*, 1:62–68, 2007.
- S5. C. W. MacMinn, M. L. Szulczewski, and R. Juanes. CO₂ migration in saline aquifers. Part 1: Capillary trapping under slope and groundwater flow. *J. Fluid Mech.*, 662:329–351, 2010.
- S6. C. W. MacMinn, M. L. Szulczewski, and R. Juanes. CO₂ migration in saline aquifers. Part 2: Combined capillary and solubility trapping. *J. Fluid Mech.*, 688:321–351, 2011.
- S7. J. Bear. *Dynamics of Fluids in Porous Media*. Elsevier, New York, 1972.
- S8. H. E. Huppert and A. W. Woods. Gravity-driven flows in porous layers. *J. Fluid Mech.*, 292:55–69, 1995.
- S9. J. M. Nordbotten, M. A. Celia, and S. Bachu. Similarity solutions for fluid injection into confined aquifers. *J. Fluid Mech.*, 561:307–327, 2006.

- S10. M. A. Hesse, F. M. Orr, Jr., and H. A. Tchelepi. Gravity currents with residual trapping. *J. Fluid Mech.*, 611:35–60, 2008.
- S11. Y. C. Yortsos. A theoretical analysis of vertical flow equilibrium. *Transp. Porous Media*, 18:107–129, 1995.
- S12. R. Juanes, E. J. Spiteri, F. M. Orr, Jr., and M. J. Blunt. Impact of relative permeability hysteresis on geological CO₂ storage. *Water Resour. Res.*, 42:W12418, 2006.
- S13. J. Ennis-King and L. Paterson. Role of convective mixing in the long-term storage of carbon dioxide in deep saline formations. *Soc. Pet. Eng. J.*, 10(3):349–356, 2005.
- S14. R. Juanes, C. W. MacMinn, and M. L. Szulczewski. The footprint of the CO₂ plume during carbon dioxide storage in saline aquifers: storage efficiency for capillary trapping at the basin scale. *Transp. Porous Media*, 82:19–30, 2010.
- S15. G. Pau, J. B. Bell, K. Pruess, A. S. Almgren, M. J. Lijewski, and K. Zhang. High-resolution simulation and characterization of density-driven flow in CO₂ storage in saline aquifers. *Adv. Water Resour.*, 33(4):443–455, 2010.
- S16. R. J. LeVeque. *Numerical Methods for Conservation Laws*. Birkhäuser Verlag, Berlin, second edition, 1992.
- S17. M. L. Szulczewski. Storage capacity and injection rate estimates for CO₂ sequestration in deep saline aquifers in the conterminous United States. Master’s thesis, Massachusetts Institute of Technology, 2009.
- S18. M. D. Zoback. *Reservoir Geomechanics*. Cambridge University Press, 2007.
- S19. R. A. Freeze and J. A. Cherry. *Groundwater*. Prentice Hall, 1979.

- S20. M. L. Szulczewski, C. W. MacMinn, and R. Juanes. How pressure buildup and CO₂ migration can both constrain storage capacity in deep saline aquifers. In *10th Intl. Conf. Greenhouse Gas Control Technol., GHGT-10*, Amsterdam, The Netherlands, September 19–23, 2010.
- S21. M. L. Zoback and M. Zoback. State of stress in the conterminous United States. *J. Geophys. Res.*, 85(B11):6113–6156, 1980.
- S22. Carbon Capture and Sequestration Technologies at MIT. CO₂ thermophysical property calculator. <http://sequestration.mit.edu/tools/index.html>.
- S23. Y. K. Kharaka and J. S. Hanor. Deep fluids in the continents: I. Sedimentary basins. In J. I. Drever, editor, *Treatise on Geochemistry*, volume 5. Elsevier, 2007.
- S24. M. Batzle and Z. Wang. Seismic properties of pore fluids. *Geophysics*, 57:1396–1408, 1992.
- S25. Z. Duan and R. Sun. An improved model calculating CO₂ solubility in pure water and aqueous NaCl solutions from 273 to 533 K and from 0 to 2000 bar. *Chem. Geol.*, 193:257–271, 2003.
- S26. R. M. Enick and S. M. Scott. CO₂ solubility in water and brine under reservoir conditions. *Chem. Eng. Commun.*, 90(1):23–33, 1990.
- S27. S. Bachu. Screening and ranking of sedimentary basins for sequestration of CO₂ in geological media in response to climate change. *Environ. Geol.*, 44:277–289, 2003.
- S28. J. E. Garcia. Density of aqueous solutions of CO₂. Technical Report 49023, Lawrence Berkeley National Laboratory, 2001.

- S29. Q. Zhou, J. T. Birkholzer, C. Tsang, and J. Rutqvist. A method for quick assessment of CO₂ storage capacity in closed and semi-closed saline formations. *Int. J. Greenh. Gas Con.*, 2:626–639, 2008.
- S30. H. F. Wang. *Theory of Linear Poroelasticity*. Princeton University Press, 2000.
- S31. H. D. Cheng. *Multilayered aquifer systems: fundamentals and applications*. Marcel Dekker, 2000.
- S32. L. F. Konikow and C. E. Neuzil. A method to estimate groundwater depletion from confining layers. *Water Resour. Res.*, 43:W07417, 2007.
- S33. J. Croisé, L. Schlickenrieder, P. Marschall, J. Y. Boisson, P. Vogel, and S. Yamamoto. Hydrogeological investigations in a low permeability claystone formation: the Mont Terri Rock Laboratory. *Phys. Chem. Earth*, 29:3–15, 2004.
- S34. S. Escoffier, F. Homand, A. Giraud, N. Hoteit, and K. Su. Under stress permeability determination of the Meuse/Haute-Marne mudstone. *Eng. Geol.*, 81:329–340, 2005.
- S35. S. Mishra, J. F. Pickens, and J. Delay. New approaches for transient testing and long-term pressure monitoring of low-permeability caprocks. In *Proceedings of the International Symposium on Site Characterization for CO₂ Geological Storage*, 2006.
- S36. C. E. Neuzil. How permeable are clays and shales? *Water Resour. Res.*, 30(2):145–150, 1994.
- S37. T. Tokunaga, S. Hosoya, H. Tosaka, and K. Kojima. An estimation of the intrinsic permeability of argillaceous rocks and the effects of long-term fluid migration. In S. J. Düppenbecker and J. E. Iliffe, editors, *Basin Modelling: Practice and Progress*, volume 141, pages 83–94. Geological Society of London, 1998.

- S38. D. N. Dewhurst, Y. Yang, and A. C. Aplin. Permeability and fluid flow in natural mudstones. In A. C. Aplin, A. J. Fleet, and J. H. S. Macquaker, editors, *Muds and Mudstones: Physical and Fluid-flow Properties*, volume 158, pages 23–43. Geological Society of London, 1999.
- S39. S. Neglia. Migration of fluids in sedimentary basins. *A.A.P.G. Bulletin*, 63(4):573–597, 1979.
- S40. D. B. Bennion and S. Bachu. Drainage and imbibition relative permeability relationships for supercritical CO₂/brine and H₂S/brine systems in intergranular sandstone, carbonate, shale, and anhydrite rocks. *Soc. Pet. Eng. J.*, 11(3):487–496, 2008.
- S41. L.H. Wickstrom, E. R. Venteris, J. A. Harper, J. McDonald, E. R. Slucher, K. M. Carter, S. F. Greb, J. G. Wells, W. B. Harrison III B. C. Nuttall, R. A. Riley, J. A. Drahovzal, J. A. Rupp, K. L. Avary, S. Lanham, D. A. Barnes, N. Gupta, M. A. Baranoski, P. Radhakrishnan, M. P. Solis, G. R. Baum, D. Powers, M. E. Hohn, M. P. Parris, K. McCoy, G. M. Grammer, S. Pool, C. Luckhardt, and P Kish. Characterization of geologic sequestration opportunities in the MRCSP Region: final report under DOE cooperative agreement DE-PS26-05NT42255, 2005.
- S42. H. L. Young and D. I. Siegel. Hydrogeology of the Cambrian-Ordovician aquifer system in the northern Midwest, United States, with a section on ground-water quality. Professional Paper 1405-B, U.S.G.S., 1992.
- S43. H. B. Willman, E. Atherton, T. C. Buschbach, C. Collinson, J. C. Frye, M. E. Hopkins, J. A. Lineback, and J. A. Simon. *Handbook of Illinois stratigraphy*. Number Bulletin 95. Illinois State Geological Survey, 1975.

- S44. S. D. Hovorka, M. L. Romero, A. G. Warne, W. A. Ambrose, T. A. Tremblay, R. H. Trevino, and D. Sasson. Sequestration of greenhouse gases in brine formations. <http://www.beg.utexas.edu/environqlty/co2seq/dispslsalnt01.htm>, November 2003.
- S45. Jr. O. B. Lloyd and W. L. Lyke. The ground water atlas of the United States: Illinois, Indiana, Kentucky, Ohio, Tennessee. Hydrologic Atlas 730-K, U.S.G.S., 1995.
- S46. R. J. Mandle and A. L. Kontis. Simulation of regional ground-water flow in the Cambrian-Ordovician aquifer system in the northern Midwest, United States. Professional Paper 1405-C, U.S.G.S., 1992.
- S47. S. D. Hovorka, M. L. Romero, A. G. Warne, W. A. Ambrose, T. A. Tremblay, R. H. Trevino, and D. Sasson. Brine-formation database. <http://www.beg.utexas.edu/environqlty/co2seq/dispslsalnt01.htm>, November 2003.
- S48. D. A. Barnes, D. H. Bacon, and S. R. Kelley. Geological sequestration of carbon dioxide in the Cambrian Mount Simon Sandstone: regional storage capacity, site characterization, and large-scale injection feasibility, Michigan Basin. *Env. Geosci.*, 16(3):163–183, 2009.
- S49. H. E. Leetaru and J. H. McBride. Reservoir uncertainty, Precambrian topography, and carbon sequestration in the Mt. Simon Sandstone, Illinois Basin. *Env. Geosci.*, 16(4):235–243, 2009.
- S50. P. B. King and H. M. Beikman. Geologic map of the United States. US Geological Survey, 1974.
- S51. M. J. Oak, L. E. Baker, and D. C. Thomas. Three-phase relative permeability of Berea sandstone. *J. Pet. Technol.*, 42(8):1054–1061, August 1990.

- S52. T. J. Kneafsey and K. Pruess. Laboratory flow experiments for visualizing carbon dioxide-induced, density-driven brine convection. *Transp. Porous Med.*, 82:123–139, 2010.
- S53. A. Riaz, M. Hesse, H. A. Tchelepi, and F. M. Orr, Jr. Onset of convection in a gravitationally unstable, diffusive boundary layer in porous media. *J. Fluid Mech.*, 548:87–111, 2006.
- S54. A. Kron and G. Heiken. Geothermal gradient map of the United States. Technical report, Los Alamos National Lab, 1980.
- S55. M. Nathenson and M. Guffanti. Geothermal gradients in the conterminous united states. *J. Geophys. Res.*, 93:6437–6450, 1988.
- S56. Mean daily average temperature map of the United States. <http://cdo.ncdc.noaa.gov/cgi-bin/climaps/climaps.pl>, 2010.
- S57. N. Gupta. *Geologic and fluid-density controls on the hydrodynamics of the Mt. Simon Sandstone and overlying geologic units in Ohio and surrounding states*. PhD thesis, The Ohio State University, 1993.
- S58. Salinity of the Mt. Simon Sandstone in the Illinois Basin. Technical report, Midwest Geological Sequestration Consortium, 2005.
- S59. S. Bachu and J. J. Adams. Sequestration of CO₂ in geological media in response to climate change: capacity of deep saline aquifers to sequester CO₂ in solution. *Energ. Convers. Manage.*, 44:3151 – 3175, 2003.
- S60. D. C. Lampe. Hydrogeologic framework of bedrock units and initial salinity distribution

for a simulation of groundwater flow for the Lake Michigan Basin. Scientific Investigations Report 2009-5060, USGS, 2009.

- S61. J. A. Miller. The ground water atlas of the United States: Alabama, Florida, Georgia, South Carolina. Hydrologic Atlas 730-G, U.S.G.S., 1990.
- S62. R. A. Renken. Hydrology of the southeastern Coastal Plain aquifer system in Mississippi, Alabama, Georgia, and South Carolina. Professional Paper 1410-B, U.S.G.S., 1996.
- S63. W. R. Aucott. Hydrology of the southeastern Coastal Plain aquifer system in South Carolina and parts of Georgia and North Carolina. Professional Paper 1410-E, U.S.G.S., 1996.
- S64. E. W. Strom and M. J. Mallory. Hydrogeology and simulation of ground-water flow in the Eutaw-McShan Aquifer and in the Tuscaloosa Aquifer system in northeastern Mississippi. Water-Resources Investigation Report 94-4223, U.S.G.S., 1995.
- S65. P. L. Applin and E. R. Applin. The Gulf Series in northern Florida and southern Georgia. Professional Paper 524-G, U.S.G.S., 1967.
- S66. National Imagery and Mapping Agency. Digital terrain elevation data (DTED Level 0). <http://www.geocomm.com>.
- S67. R. W. Lee. Geochemistry of ground water in the Southeastern Coastal Plain Aquifer System in Mississippi, Alabama, Georgia, and South Carolina. Professional Paper 1410-D, U.S.G.S., 1994.
- S68. R. A. Barker and M. Pernik. Regional hydrology and simulation of deep ground-water

flow in the Southeastern Coastal Plain aquifer system in Mississippi, Alabama, Georgia, and South Carolina. Professional Paper 1410-C, U.S.G.S., 1994.

- S69. L. Y. Sadler, M. B. Rahnama, and G. P. Whittle. Laboratory measurement of the permeability of Selma Chalk using an improved experimental technique. *Hazard. Waste Hazard. Mater.*, 9(4):331–343, 1992.
- S70. R. W. Lee. Water–quality maps for selected Upper Cretaceous water–bearing zones in the southeastern coastal plain. Water-Resources Investigations Report 85-4193, U.S.G.S., 1985.
- S71. S. D. Hovorka. Optimal geological environments for carbon dioxide disposal in saline aquifers in the United States. Contract Report DE-AC26-98FT40417, Bureau of Economic Geology, The University of Texas at Austin, 1999.
- S72. W. E. Galloway, D. K. Hobday, and K. Magara. Frio Formation of Texas Gulf Coastal Plain: depositional systems, structural framework, and hydrocarbon distribution. *A.A.P.G. Bulletin*, 66(6):649–648, 1982.
- S73. S. D. Hovorka, C. Doughty, P. R. Knox, C. T. Green, K. Pruess, and S. M. Benson. Evaluation of brine-bearing sands of the Frio Formation, Upper Texas Gulf Coast for geologic sequestration of CO₂. Technical report, Bureau of Economic Geology, 2001.
- S74. P. D. Ryder and A. F. Ardis. Hydrology of the Texas Gulf Coast aquifer systems. Open-File Report 91-64, U.S.G.S., 1991.
- S75. S. E. Frezon, T. M. Finn, and J. H. Lister. Total thickness of sedimentary rocks in the conterminous United States, 1983.

- S76. R. G. Loucks, M. M. Dodge, and W. E. Galloway. Regional controls on diagenesis and reservoir quality in lower Tertiary sandstones along the lower Texas Gulf Coast. In D. A. McDonald and R. C. Surdam, editors, *Clastic diagenesis*. A. A. P. G., 1984.
- S77. C. W. Kreitler, M. S. Akhter, and A. C. Donnelly. Hydrologic hydrochemical characterization of Texas Frio Formation used for deep-well injection of chemical wastes. *Environ. Geol. Water Sci.*, 16(2):107–120, 1990.
- S78. R. A. Morton and L. S. Land. Regional variations in formation water chemistry, Frio Formation (Oligocene), Texas Gulf Coast. *A.A.P.G. Bulletin*, 71(2):191–206, 1987.
- S79. R. L. Whitehead. The ground water atlas of the United States: Montana, North Dakota, South Dakota, Wyoming. Hydrologic Atlas 730-I, U.S.G.S., 1996.
- S80. J. S. Downey. Geohydrology of the Madison and associated aquifers in parts of Montana, North Dakota, South Dakota, and Wyoming. Professional Paper 1273-G, U.S.G.S., 1984.
- S81. G. W. Freethey and G. E. Cordy. Geohydrology of Mesozoic rocks in the Upper Colorado River Basin in Arizona, Colorado, New Mexico, Utah, and Wyoming, excluding the San Juan Basin. Professional Paper 1411-C, U.S.G.S., 1991.
- S82. G. W. Freethey, B. A. Kimball, D. E. Wilberg, and J. W. Hood. General hydrogeology of the aquifers of Mesozoic age, Upper Colorado River Basin – excluding the San Juan Basin – Colorado, Utah, Wyoming, and Arizona. Hydrologic Atlas 698, U.S.G.S., 1988.
- S83. J. M. Kernodle. Hydrogeology and steady-state simulation of ground-water flow in the San Juan Basin New Mexico, Colorado, Arizona, and Utah. Water-Resources Investigation Report 95-4187, U.S.G.S., 1996.

- S84. L. C. Craig et al. Stratigraphy of the Morrison and related formations, Colorado Plateau Region. Bulletin 1009-E, U.S.G.S., 1955.
- S85. W. L. Dam, J. M. Kernodle, G. W. Levings, and S. D. Craigg. Hydrogeology of the Morrison Formation in the San Juan structural basin, New Mexico, Colorado, Arizona, and Utah. Hydrologic Investigations Atlas HA-720-J, U.S.G.S., 1990.
- S86. Jr. H. Trapp. Hydrogeologic framework of the Northern Atlantic Coastal Plain in parts of North Carolina, Virginia, Maryland, Delaware, New Jersey, and New York. Professional Paper 1404-G, U.S.G.S., 1992.
- S87. H. Trapp, Jr. and M. A. Horn. The ground water atlas of the United States: Delaware, Maryland, New Jersey, North Carolina, Pennsylvania, Virginia, West Virginia. Hydrologic Atlas 730-L, U.S.G.S., 1997.
- S88. E. A. Merewether. Stratigraphy and tectonic implications of Upper Cretaceous rocks in the Powder River Basin, northeastern Wyoming and southeastern Montana. Bulletin 1917-T, U.S.G.S., 1996.
- S89. J. S. Downey and G. A. Dinwiddie. The regional aquifer system underlying the Northern Great Plains in parts of Montana, North Dakota, South Dakota, and Wyoming—summary. Professional Paper 1402-A, U.S.G.S., 1988.
- S90. B. J. O. L. McPherson and B. S. Cole. Multiphase CO₂ flow, transport and sequestration in the Powder River Basin, Wyoming, USA. *Journal of Geochemical Exploration*, 69–70:65–69, 2000.
- S91. R. Q. Foote, L. M. Massingill, and R. H. Wells. Petroleum geology and the distribution of conventional crude oil, natural gas, and natural gas liquids, East Texas Basin. Open-File Report 88-450-K, U.S.G.S., 1988.

- S92. D. R. Kolata. *Interior Cratonic Basins*, chapter 2, pages 59–73. A.A.P.G, 1990.
- S93. J. D. Hoholick, T. Metarko, and P. E. Potter. Regional variations of porosity and cement: St. Peter and Mt. Simon sandstones in Illinois Basin. *A.A.P.G. Bulletin*, 68(6):753–764, 1984.
- S94. W. F. Meents, A. H. Bell, O. W. Rees, and W. G. Tilbury. Illinois oilfield brines: their geologic occurrence and chemical composition. Illinois Petroleum 66, Illinois Geological Survey, 1952.
- S95. P. L. Applin and E. R. Appin. Regional subsurface stratigraphy and structure of Florida and southern Georgia. *A.A.P.G. Bulletin*, 28(12):1673–1753, 1944.
- S96. S. D. Hovorka, M. L. Romero, A. G. Warne, W. A. Ambrose, T. A. Tremblay, R. H. Trevino, and D. Sasson. Brine-formation database. <http://www.beg.utexas.edu/environqlty/co2seq/>, November 2003.
- S97. S. E. Frezon, T. M. Finn, and K. L. Lister. Map of sedimentary basins in the conterminous United States. <http://pubs.er.usgs.gov/usgspubs/om/om223>, 1988.
- S98. K. Bjørlykke. Fluid flow in sedimentary basins. *Sedimentary Geology*, 86:137–158, 1993.
- S99. P. Ortoleva, editor. *Basin Compartments and Seals*. A.A.P.G. Memoir 61. A.A.P.G, 1994.
- S100. S. Bachu. Screening and ranking of sedimentary basins for sequestration of CO₂ in geological media in response to climate change. *Environ. Geol.*, 44:277–289, 2003.